Internal structure and geochemical properties of spheroidal ferromanganese concretions of the Baltic Sea

UNIVERSITY OF HELSINKI

SYKE

Joonas Wasiljeff

MSc. Thesis

COMICS-project

HELSINGIN YLIOPISTO – HELSINGFORS UNIVERSITET – UNIVERSITY OF HELSINKI

Tiedekunta/Osasto – Fakultet/Sektion – Faculty/Section	Laitos – Institution – Department	
Faculty of Science	Geosciences and Geography	
Tekijä – Författare – Author		
Joonas Allan Mikael Wasiljeff		
Työn nimi – Arbetets titel – Title		
Internal structure and geochemical properties of spheroidal ferromanganese concretions of the Baltic Sea		
Oppiaine – Läroämne – Subject		
Geology		
Työn laji – Arbetets art – Level	Aika – Datum – Month and year	Sivumäärä – Sidoantal – Number of pages
MSc. Thesis	9/2015	92

Tiivistelmä – Referat – Abstract

Ferromanganese concretions or nodules are recent biogeochemical sedimentary formations present in abundant amounts at the fringes of deep basins in the area of the Baltic Sea. The concretions have a distinctive concentric structure, consisting of alternating iron and manganese-rich layers. The iron layers typically host phosphorus, and the concretions also work as traps for many other compounds such as heavy metals and REEs. In general, their dissolution occurs in anoxic conditions whereas precipitation in an oxic environment.

Structural and geochemical analyses were performed to understand the growth and evolution of spheroidal ferromanganese concretions from the Gulf of Finland. Porosity, layer structure and the chemical composition of the concretions were assessed using CT-scanning, EDS, XRF, and LOI analyses. Dissolution experiment in anoxic conditions was also implemented by incubating the deoxygenated samples stored in Anaerogen containers.

The analyses showed that Mn layers host a vast pore network. A qualitative identification of the Fe/Mn ratio of layers with different densities was achieved by CT scanning coupled with EDS element mapping. Diffuse structures and the presence of microbial structures in Mn-rich layers could be affiliated with metal oxide susceptibility to redox reactions mediated by microbial processes. On the other hand, Fe-rich layers are more coherent and dense than the Mn-rich layers. Computed tomography analysis also showed that the pore networks extend from the surface of the concretions to the core. The calculated surface area of the pore network is 2 to 5 times greater than the exterior surface area of the concretions. The large surface area is believed to provide a suitable living environment for Fe and Mn reducing and oxidizing microbes. Both of the metals are susceptible to reductive conditions, Fe seemingly being more vulnerable to dissolution with the presence of a carbon source and sulphate. While oxygen is present, Fe (oxyhydr)oxides are effectively formed. In addition, substantial amounts of P was released during the dissolution experiment which may have importance in the Gulf of Finland.

Avainsanat – Nyckelord – Keywords

Iron, Manganese, Concretion, Nodule, Geochemistry, X-Ray Tomography, Structure, Baltic Sea

Säilytyspaikka – Förvaringställe – Where deposited

University of Helsinki, Department of Geosciences and Geography, Kumpula Science Library

Muita tietoja – Övriga uppgifter – Additional information

HELSINGIN YLIOPISTO – HELSINGFORS UNIVERSITET – UNIVERSITY OF HELSINKI

Tiedekunta/Osasto – Fakultet/Sektion – Faculty/Section	Laitos – Institution – Department
Matemaattis-luonnontieteellinen	Geotieteiden ja Maantieteen laitos

Tekijä – Författare – Author
Joonas Allan Mikael Wasiljeff

Työn nimi – Arbetets titel – Title
Internal structure and geochemical properties of spheroidal ferromanganese concretions of the Baltic Sea

Oppiaine – Läroämne – Subject
Geologia

Työn laji – Arbetets art – Level	Aika – Datum – Month and year	Sivumäärä – Sidoantal – Number of pages
Pro Gradu	9/2015	92

Tiivistelmä – Referat – Abstract

Itämeressä syvänteiden reunamilla runsaina esiintyvät rautamangaanikonkreetiot tai nodulit ovat biogeokemiallisten prosessien viimeisen jäätiköitymsen jälkeen synnyttämiä. Konkreetiotioilla on ominainen, vuorottelevista ja konsentrisista mangaani- ja rautarikkaammista kerroksista muodostuva rakenne. Rautapitoisemmissa kerroksissa on yleensä myös runsaasti fosforia. Lisäksi konkreetiot toimivat loukkuina useille muille yhdisteille ja alkuaineille, kuten raskasmetalleille ja REE:lle. Yleisesti ottaen konkreetiot kasvavat hapellisissa ja liukenevat hapettomissa olosuhteissa.

Suomenlahdelta olevien pallomaisten konkreetioiden rakennetta ja geokemiallisia ominaisuuksia tutkittiin niiden kasvun ja kehityksen ominaispiirteiden selvittämiseksi. Myös niiden käyttäytymistä hapettomissa oloissa tutkittiin pelkistyskokeella. Käytettyjä menetelmiä ovat röntgentomografia, EDS elektronimikroanalysaattorilla, XRF ja hehkutus.

Röntgentomografian ja EDS analyysin avulla voitiin osoittaa konreetioiden rakenteiden vallitseva kemiallinen koostumus ja niiden tiheys. Analyysit osoittivat että konkreetiot koostuvat tiheämmistä rautarikkaista kerroksista ja löyhemmistä mangaanirikkaammista kerroksista. Mangaanirikkaissa kerroksissa esiintyy laaja ja epäsäännöllinen huokosverkosto, joka ulottuu konkreetioiden ulkopinnalta niiden ytimeen. Tutkittujen huokosverkostojen pinta-ala on kahdesta viiteen kertaa niin laaja, kuin konkreetioiden ulkopinta-ala. Konreetioilla on siis selvä kasvuvaihe ja epäselvä liukenemisvaihe. Mangaanirikkaissa kerroksissa havaittiin myös mikrobien rakenteita. Pelkistyskokeessa konkreetiot liukenivat, ja näyteastioihin saostui raudan (oksihydr)oksideja sekä raudan (mono)sulfideja. Lisäksi Fe (oksihydr)oksideissa oli sauvamaisia bakteereita. Liuokseen vapautui myös merkittävästi fosforia rautarikkaammista kerroksista.

Tutkimuksen avulla voitiin osoittaa miten tiheämmät ja löyhemmät kerrokset jakaantuvat konkreetioiden sisällä, sekä miten liukenemisrakenteet eli huokoset suhtautuvat niihin. Lisäksi kerrosten vallitseva kemiallinen koostumus määritettiin. Koska bakteerit tarvitsevat läheisen tai suoran kontaktin materiaalin, jota ne prosessoivat, uskotaan suuren huokosverkoston ja mikrobiaalisten rakenteiden esiintymisen mangaanirikkaissa kerroksissa olevan osoitus biogeenisten prosessien läsnäolosta konreetioissa. Saostuminen tapahtuu hapen läsnäollessa. Hapettomattomissa oloissa konkreetioit liukenevat, ja vapauttavat fosforia, jolla on mahdollisia seurauksia Suomenlahdella. Mikrobiologisen sulfaatinpelkistyksen tuottama vetysulfidi reageoi pelkistyneen raudan kanssa muodostaen Fe sulfideita, joka estää fosforin pidättymisen raudan yhdisteisiin.

Avainsanat – Nyckelord – Keywords
Rauta, Mangaani, Konkreetio, Noduli, Geokemia, Röntgentomografia, Rakenne, Itämeri

Säilytyspaikka – Förvaringställe – Where deposited
Helsingin yliopisto, Geotieteiden ja Maantieteen laitos, Kumpulan kampuskirjasto

Muita tietoja – Övriga uppgifter – Additional information

SHORT GLOSSARY

Cavity, pore, pore network	=	features formed by dissolution processes, void space
Concretion, nodule	=	in this study, among other related studies, concretion and nodule are used interchangeably. However, emphasis was given to the term 'concretion', as sedimentary concretions usually display internal structure, in a similar fashion to spheroidal concretions studied here
Core	=	core is used as a descriptive term to the innermost parts of the sample concretions
CT scanning	=	X-ray Computed Tomography imaging, creation of 3D reconstruction of X-ray imaged sample from an image stack of single slices
Dissolution analysis	=	exposing the samples to deoxygenated (=anoxic/anaerobic) environment in order to see possible changes in structure and composition
EDS, element mapping	=	Energy Dispersive Spectrometry by which analyzing of desired elements in an area of interest is possible
EDS, spot analysis	=	determination of predominant chemical composition of a single spot in the sample
EPMA	=	Electron Probe Microanalyzer. The samples studied here with EPMA were analyzed with EDS detector.
LOI	=	Loss On Ignition. Traditional method to determine porosity, organic matter, crystallization water and carbonates in a (sedimentary) sample by igniting it in high temperatures
Slice	=	one image of the CT scan image stack
Spheroidal	=	rounded, sphere-like, spherical
XRF	=	X-ray Fluorescence Spectroscopy. Can be divided into Energy Dispersive (ED) and Wavelength Dispersive (WD). The method is based on interactions of X-rays and a sample and a subsequent release of characteristic X-rays from elements in the sample and their measurement. WDXRF was used in this study

CONTENTS

1. INTRODUCTION

The growth and evolution of ferromanganese concretions (also known as iron-manganese concretions (IMC's) or iron-manganese nodules) found on the Baltic Sea seafloor has been an enigma to researchers for some time now. It is well known, however, that they are composed mostly of iron and manganese oxides, hydroxides and oxyhydroxides, detrital silicate minerals and minor amounts of numerous elements such as heavy metals and REEs. It is suggested that the formation of ferromanganese concretions is a recent biogeochemical process (e.g. Grigoriev et al. 2013, Ojala 2008, Zhang et al. 2002, Hu et al. 2000). The alternating Fe and Mn-rich layers seem to form due to chemical reactions catalyzed by differences in redox properties (e.g. Axelsson et al. 2002, Gasparatos et al. 2005). Moreover, microbial activity could partly drive the redox reactions occurring both inside the concretions and on their surface (Yli-Hemminki et al. 2014). Some bacteria able to reduce Mn^{4+} and Fe^{3+} have been identified. These microbes utilize the Fe and Mn oxides as electron acceptors to drive their metabolic circulation. Also microbes reoxidizing the reduced forms are commonly seen in the nodules. Recent investigations suggest that known Fe and Mn reducers and oxidizers are a minority in the microbe community associated with the concretions (Yli-Hemminki et al. 2014). Nevertheless, it is noteworthy that Mn and Fe also work together in a more direct way, as Mn^{3+}/Mn^{4+} is capable of oxidizing Fe^{2+} and thus affect the formation of Fe^{3+} (oxyhydr)oxides (Krishnamurti and Huang 1988, Postma 1985).

The origin of manganese and iron in the first place, however, is due to the effect of weathering of the lithosphere and sediments, and the transportation of the then dissolved ions and particulate matter by fluvial erosion, and ultimately their accumulation on the seafloor (Poulton and Raiswell 2002). Typically iron and manganese originates from glaciogenic deposits such as tills in the area of the Baltic Sea (Glasby et al. 1997). Even so, availability of manganese is more closely governed by biological productivity and thus related to reductive processes in the sediment, and the reflux of Mn and Fe from the sediment (Anufriev and Boltenkov 2007, Pokhamova 2007). Usually, the supply of the ions is also affected greatly by the oxygen levels of the water column, penetration of oxygen to the sediment and

the depth of carbonate compensation depth (CCD) (Klinkhammer 1980, Halbach and Puteanus 1984 Pokhamova 2007).

Winterhalter and Siivola (1967) were the first to actually describe and study the internal structure of the concretions of the Baltic Sea using electron microprobe. They noted that there was a clear correlation between phosphorus and Fe-rich layers. Later Suess and Djafari (1977) found out that the concretions in the Bay of Kiel of the Baltic Sea contained anomalously high concentrations of Zn, Pb, Cd and Cu. Moreover, they concluded that this was the result of increased anthropogenic impact on the Baltic Sea. However, Ingri and Pontér (1986) in their study deducted that this was not the case and these elements were not from an anthropogenic source in the first place. Instead, they showed that elements like Y and La, which generally are not considered to be from a pollution source, had high concentrations in the surface of the ferromanganese concretions as well. These enrichment processes could be natural, governed by the redox state. Because of this it is difficult to distinguish the anthropogenic impact from the nature's processes (Ingri and Pontér 1986). Nevertheless, more studies were carried out in the Bay of Kiel which suggested that the concretions could indeed function as an indicator of pollution occurring in the area (Glasby et al. 1997). The ability of trapping heavy metals and REEs is attributed to the mineralogy of the concretions. Especially Mn oxides have a high sorption capacity for metal cations (Miyata et al. 2007).

Since the discovery of manganese nodules in 1873, many researchers have contemplated on the thought of bacteriogenic processes to be behind the formation of these concretions. For instance Thiel (1925) already concluded that microorganisms which precipitate manganese can be found nearly everywhere in the world. Also later studies (eg. Werdanskij 1930, Graham and Cooper 1959) claimed that the formation of manganese concretions is mediated by biological processes instead of inorganic processes. Furthermore, Sorokin (1972) reported that microbial life is more intensive in the ferromanganese concretions than in the surrounding sediments. This is supported by later findings: manganese oxides found in sediments are mainly produced by bacterial oxidation (Thamdrup et al. 1994) as Mn^{2+} is not as readily oxidized by inorganic pathways. Biological oxidation of manganese is more efficient than abiotic Mn^{2+} oxidation (Tebo et al. 2004). These studies have identified distinctive microbe types

which accumulate ferromanganese minerals. Microstructures of bacteria have been identified and microbially mediated minerals birnessite and manganosite have been reported also in the Baltic Sea (Zhang et al. 2002).

The primary aim of this study is to produce 1) detailed information about the geochemical and physical properties of the concretions linked to microbial processes occurring in the concretions, 2) the effect of anoxic environment to their structure and stability and 3) the origin of internal structure of dense and less dense layers (e.g. Glasby et al. 1997, Zhamoida 2004). Thus, three focal hypotheses have risen:

1: The interior parts of the spheroidal samples have more reactive surface area than the exterior of the concretions, hence indicating possible dwellings for microorganisms which need a close or even direct contact to the material they are affecting (Thullner et al. 2005).

2: There is a distinctive layered structure formed by iron and manganese-rich layers – Fe layers being more dense.

3: Reductive dissolution is focused on metal oxides of the concretions, especially manganese due to its greater redox sensitivity.

To verify this the porosity is measured and the appearance of the pore network is assessed utilizing micro CT-scanning. X-ray fluorescence analysis (XRF) and microprobe (EPMA) will be used to determine the chemical composition of the concretions and couple the composition of sub-layers with structural variations observed in CT scanning. Furthermore, the concretions are incubated in reductive environment and then rescanned with CT. EPMA will be used to determine the chemistry of possible precipitates and XRF to determine the release of major compounds to the analysis fluid. The use of micro X-ray tomography is a new approach to study the relatively well presumed internal structure of spheroidal ferromanganese concretions of the Baltic Sea. Also a more traditional method, the loss on ignition method (LOI), will be utilized to determine the amount of organic matter and the amount of carbonates in the concretions.

2. GEOLOGICAL AND BIOGEOCHEMICAL SETTING OF THE FERROMANGANESE CONCRETIONS

2.1 Concretions and the biogeochemistry of iron and manganese

Iron and manganese are heavy transition metals commonly seen together in various geological environments (Lahermo et al. 1996, p. 79). Both iron and manganese are delivered to oceans mainly by rivers, icebergs, dust particles, recycling of shelf material and hydrothermal activity (Raiswell and Canfield 2012). In the area of the Baltic Sea, the transport of oxidized colloidal or suspended matter by river runoff is most probably the primary form of delivery (Chester, 1990, Poulton and Raiswell 2002, Raiswell and Canfield 2012, Kendall et al. 2012). Arrival of this colloidal matter to the sea neutralizes the surface charges of the particles which in turn makes coagulation and precipitation possible (Gustafsson et al. 2000, Krachler et al. 2010).

The oxidation states of iron are Fe^{2+} and Fe^{3+} of which the former is called ferrous iron and the latter ferric iron (Kendall et al. 2012). In the case of manganese, Mn has numerous oxidation states of which the most common are Mn^{2+}, Mn^{3+} and Mn^{4+} (Tebo et al. 1997). Both iron and manganese are involved in complex biogeochemical processes which are affected by the pH, Eh, CO_2 availability, temperature and metal complex forming with inorganic and organic ligands, among other factors. In general, the reduced forms are present in low pH and anoxic conditions, whereas the oxygenated forms are thermodynamically more stable in an oxic environment and higher or circumneutral pH (Tebo et al. 2007, Raiswell and Canfield 2012). The metals have an important role in biological systems. This is related to the fact that iron and especially manganese have a rather high redox potential. Hence, manganese works as a focal energy source in certain microbiological systems and environments (e.g. Yli-Hemminki et al. 2014, Miyata et al. 2007, Tebo et al. 2007, Lovley 1991). Similarly, also iron works as an important source of energy for certain organisms such as siderophore excreting prokaryotes and eukaryotic phytoplankton (Raiswell and Canfield 2012). Iron is an important limiting nutrient for the growth of marine plankton and thus affects the CO_2 levels of the atmosphere (Raiswell and Canfield 2012).

In oxidizing conditions, iron and manganese tend to form oxides, hydroxides and

oxyhydroxides (Gasparatos et al. 2005). Still, manganese is not as readily oxidized as iron by inorganic pathways (Tebo et al. 2007). Instead, sedimentary Mn oxides are generally the result of microbial oxidation (Thamdrup et al. 1994, Tebo et al. 2004). It has also been shown that manganese oxide micronodules can grow in a short period of time to heat exchangers using Baltic sea water (Kuosmanen et al. 2005). Manganese oxides absorb cations whereas iron oxyhydroxides tend to incorporate oxyanions and cobolt (Kochinsky and Halbach 1995). As iron readily forms these strong bonds with anionic ligands such as oxygen, phosphorus, sulphur and nitrogen, it has a natural tendency to be incorporated into biological systems (Kendall et al. 2012). Therefore it is a notable component for instance in enzymes such as hydrogenases, iron-sulphur proteins and cytochromes. Hydrogenases are enzymes that catalyze the oxidation of hydrogen by reducing a substrate. Fe-S proteins, on the other hand, are electron carriers which are composed of variable amounts of Fe-S clusters which contain sulphide-linked di-, tri-, and tetrairon centers. These centers typically have two redox states. Fe-S clusters are found in many different metalloproteins, including hydrogenases. Cytochromes are iron containing porphyrin rings, i.e. hemes, that are able to alternate between Fe^{2+} and Fe^{3+}. Some cytochromes have a specific function of promoting the transfer of electrons from the external environment to the metabolic transport chain and thus are related for instance to the oxidation of Fe^{2+} (Kendall et al. 2012). In a similar fashion, also manganese is an essential part of certain enzymes such as manganese superoxide dismutase, manganese catalase, and manganese-dependent ribonucleotide reductase (Tebo et al. 2007). Both Mn superoxide dismutase and catalase are important antioxidants in prokaryote cells whereas Mn ribonucleotide reductase controls the production rate of DNA and thus affects the growth of the organism (Iordan et al. 2000, Schmitz et al. 2006).

In addition, it seems that Mn^{4+} is able to oxidize Fe^{2+} and produce ferric iron compounds (1) (Krishnamurti and Huang 1988, Postma 1985).

$$2Fe^{2+} + MnO_2 + 2H_2O \rightarrow Mn^{2+} + 2FeOOH + 2H^+ \qquad (1)$$

The reaction is spontaneous in pH of 3 and transpires within couple of minutes (Postma 1985). The reaction pathway alters when pH gets higher, however, and hence the

reaction is slowed. Several indications of the reaction in natural environment has also been observed. For instance observations in Lake Matano in Indonesia has showed clear interactions between the metals: a chemocline which segregates manganese rich upper sediment layers from the lower layers which have accumulated iron (Jones et al. 2011). When manganese (oxyhydr)oxides migrate to the level of iron compounds, iron effectively reduces manganese. Similar iron and manganese cycling has been observed in Lake Baikal (Och et al. 2012). It is suggested that sulphate reduction and methanogenesis establishes a Fe/Mn system in which manganese and iron are repeatedly reduced and reoxidized. Anaerobic oxidation of methane (AOM) produces aqueous Mn^{2+} and bicarbonate thus allowing the manganese to roam back to oxidizing layers. This results in increased concentrations of manganese in top parts of the sediment column. Similar processes have been recently assumed in brackish water basins such as the Black Sea and the Baltic Sea (Egger et al. 2015). AOM has a crucial role in the remobilization of iron as well. The implication of this to the availability of Fe^{2+} in the sediment would be ca. 3% and hence have a high impact on ferrous-phosphate mineral precipitation. Usually the formation of Fe compounds in the early diagenesis yields amorphous ferric iron-phosphates (Och et al. 2012).

Under reducing conditions, however, Fe and Mn (oxyhydr)oxides are effectively dissolved and the metals become relatively mobile. Usually, Mn^{4+} is reduced before Fe^{3+} (Marcus et al. 2004). Commonly only a small fraction of the metals are present in their aqueous form as the forming (oxyhydr)oxides are insoluble, in contrast to the fact that biological systems require them to be in solution to be bioavailable (Raiswell and Canfield 2012). These kinds of conditions may be reached in areas of high bottom organic content – the oxidation of organic matter depletes the system of oxygen thus leading to reductive conditions which are capable of mobilizing the metals (Lahermo et al. 1996, p. 79). Hence areas of low C_{org} are formidable for the growth of ferromanganese concretions as well. Enhancement of primary production during spring consumes oxygen from the bottom waters thus increasing the flux of manganese (Marcus et al. 2004). However, summer anoxia mitigates the flux of Mn and increases the flux of Fe. It is probable, that at least ~50 % of the aqueous iron is in reality also complexed with organic ligands such as polysaccharides (Raiswell and Canfield 2012).

In addition to the oxygen depleted environment in contintental margin sediments (high C_{org}) and the microbial reduction of Fe^{3+}, the introduction of sulphides in the system favors the formation of iron sulphides and hence the immobilization of iron (Kendall et al. 2012). In diagenesis, sulphate is microbially reduced to sulphides and then ferric iron is reduced to ferrous iron, the latter reaction also producing bicarbonate (Coleman 1985, Curtis 1983, Lovley et al. 1992). Sulphate reduction is shown in reaction (2):

$$CH_3COO^- + SO_4^{2-} \rightarrow HS^- + 2HCO_3^- \qquad (2)$$

With the presence of H_2S, nanoparticulate Fe monosulphides are formed (3 and 4, Butler et al. 2005) and acidity is increased:

$$Fe^{2+} + H_2S \rightarrow FeS + 2H^+ \qquad (3)$$

$$Fe^{2+} + HS^- \rightarrow FeS + 2H^+ \qquad (4)$$

The formation of mono- and disulphide species leads to the precipitation of pyrite after several intermediate species such as mackinawite and other poorly ordered Fe sulphides (Luther 1991, Schoonen 2004). Pyrite (FeS_2) is then formed in diagenesis by polysulphide pathway or by H_2S pathway (Butler et al. 2005). Sulphate reduction is not the only pathway of H_2S addition to the system, as it has been showed that certain microbes can affect pyrite formation also in a more direct way by conveying S through sulphur-bearing amino acids such as cysteine (Donald and Southam 1999). Moreover, pyrite can be formed rapidly by sulphur-disproportionating bacteria (Canfield et al. 1998). The formation of insoluble pyrite is typical in anoxic ocean sediments (Berner 1985). On many occasions, Fe-sulphides are common in the sediment layers beneath marine concretion fields. Ferric iron is soluble only in really low pH (< 3.0). Really low pH levels can be achieved during sulphide oxidation and the co-release of sulphate (i.e. sulphuric acid).

$$8FeOOH + H_2S + 14H^+ \rightarrow 8Fe^{2+} + SO_4^{2-} + 12H_2O \qquad (5)$$

However, the natural reductive dissolution (5) of Fe oxides by S^{-2} has not been demonstrated thus far (according to Och et al. 2012). In laboratory environment, this process called sulphidation has been investigated with various Fe phases (including ferrihydrite, lepidocrocite, goethite, haematite and magnetite) with their respective half-lives (see Canfield et al. 1992 and Raiswell and Canfield 1996). The reductive dissolution of the same minerals was later studied and they showed longer half-lives with the exception of magnetite (Poulton et al. 2004).

Besides the inorganic pathways and microbial sulphate reduction, many chemoheterotrophic microbes have been found which reduce also Mn^{4+} and Fe^{3+} while decomposing organic material. Within the sediment column, nitrate reduction occurs first, followed by manganese and iron reduction, finally ending in sulphate reduction and methanogenesis. In these situations manganese and iron work as electron acceptors in the anaerobic metabolic circulation of the microbes. If the metals are the sole electron acceptors, these microbes are able to oxidize e.g. fatty acids, hydrogen, alcohols and a spectrum of monoaromatic compounds. Coupled with the metabolism of fermentative microbes, also carbohydrates and amino acids can be completely oxidized. Thus a presumption has risen that the reduction of manganese and iron from their tetravalent and trivalent states to divalent state is mainly controlled by the metabolism of Mn and Fe reducing bacteria (Lovley 1991). This can be expressed with reactions (6) and (7) (Konhauser and Riding 2012):

$$CH_3COO^- + 8Fe(OH)_3 \rightarrow 8Fe^{2+} + 2HCO_3^- + 15OH^- + 5H_2O \qquad (6)$$

$$CH_3COO^- + 4MnO_2 + 3H_2O \rightarrow 4Mn^{2+} + 2HCO_3^- + 7OH^- \qquad (7)$$

In these reactions microbes such as *Geobacter Metallireducens* (a gram-negative metal reducing species of deltaproteobacteria) uses Fe^{3+} and Mn^{4+} as electron acceptors (Lovley et al. 1992). As a rule, the reduction of ferric iron minerals leads to increase of pore water [Fe^{2+}] where the highest concentrations are observed at the Fe^{3+} and sulphate reduction boundary (Konhauser and Riding 2012). When ferrous iron migrates upwards it can be oxidized inorganically by either NO_3^- or MnO_2. In contrast, when ferrous iron diffuses into underlying zones of sulphate reducers and high hydrogen sulphide

concentrations, iron is effectively precipitated as iron sulphides.

It is energetically feasible for microbes to be involved also in mineral formation (Edwards et al. 2005). Fe^{2+} and Mn^{2+} can be a significant energy source for certain chemolithoautotrophic microorganisms as they yield 65 kJ mol^{-1} and 25 kJ mol^{-1}, respectively (McCollom 2000). These chemolithoautotrophs utilize CO_2 as a source of carbon and gain energy by oxidizing inorganic substrates coupled with a terminal electron acceptor which is usually oxygen (Konhauser and Riding 2012). Ferromanganese biomineralization can be expressed with reactions (8) and (9) (Konhauser and Riding 2012):

$$2Fe^{2+} + 0.5O_2 + 2H^+ \rightarrow 2Fe^{3+} + H_2O \qquad (8)$$

$$Mn^{2+} + 0.5O_2 + H_2O \rightarrow MnO_2 + 2H^+ \qquad (9)$$

The simplest way of Fe (oxyhydr)oxide formation is believed to transpire inorganically in circumneutral pH with fitting nucleation sites. In many cases, microbes can work as nucleation sites with their mere presence, as their surfaces are negatively charged in most natural environments, thus giving rise to ferromanganese mineral accumulation (Konhauser and Riding 2012).

Because natural iron (oxyhydr)oxide biomineralization is so ubiquitous, it is believed that any microorganism capable of producing anionic ligands adsorbs cationic iron species and fine grained iron (oxyhydr)oxides from their environment (Ghiorse 1984, Glasauer et al. 2001). The adsorption of iron (oxyhydr)oxides occurs mainly trough attachment to negatively charged functional groups in the surfaces of the microbes (Figure 1, Wightman and Fein 2005). Microbial cell walls are highly reactive surfaces which are usually compositionally variable, but are commonly formed of peptidoglycan (a polymer composed of sugars and amino acids) overlain by additional polymeric substances (EPS), sheats and S-layers (part of the cell envelope) (Konhauser and Riding 2012).

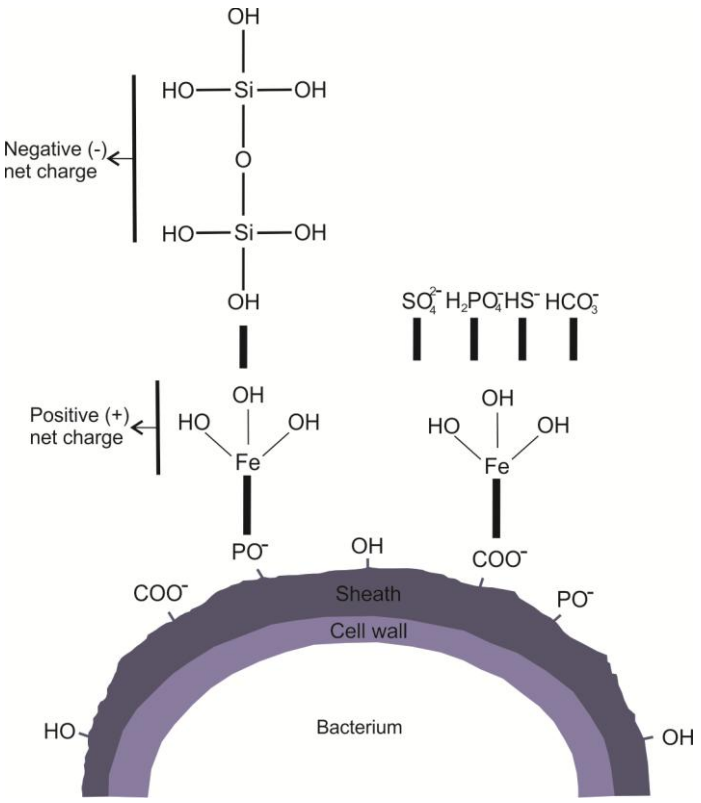

Figure 1. Schematic illustration of deprotonation of bacterial surface functional groups and subsequent attachment of metals. These metals then react inorganically with anions such as phosphate, sulfate, sulfide, bicarbonate or silica from the surrounding fluid and may thus affect mineral formation. (Modified: Konhauser and Riding 2012)

Cell surface functional groups include e.g. carboxyl, hydroxyl, phosphoryl, sulphur and amine groups which deprotonate when pH increases hence inducing a negative surface charge (Konhauser 2007). When these ionized surfaces develop, they may work as nucleation sites for minerals by lowering the interfacial energy for heterogeneous nucleation. This happens when different cations are bound to the cell wall, solid phases begin to form and at the same time the surface area of the nucleus interfering with bulk solution decreases. This in turn decreases G_0 of the mineral precipitation process and therefore boosts mineral formation. Trivalent and divalent cations are strongly bound to the cell walls of numerous bacteria whereas monovalent cations are more easily exchangeable (Konhauser and Riding 2012). All in all, potential biomineralization processes only catalyze mineral formation through kinetics, instead of extending precipitation or enhancing precipitation in undersaturated environment (Fowle and Fein 2001). Mineral size then again is determined by numerous variables such as the availability of components and reaction time.

Furthermore, biomineralization processes, were they active or passive, are present in numerous pH values and also partly ignore the presence of oxygen (Konhauser and Riding 2012). Every microbe has metabolism specifically optimized for its environmental conditions. In general, microbes gain energy from sunlight (phototrophy) or trough electron transport chains (chemotrophy), and fix carbon by the intake and reduction of CO_2 (autotrophy) or by consuming existing organic compounds (heterotrophy). Whatever was the pathway, microbes effectively affect the redox and saturation states of surrounding fluids. Ferric iron compounds can be produced by anoxygenic photosynthesis, whereas both oxidized Mn and Fe compounds can be produced by chemolithoautotrophs. For instance, some chemolithoautotrophs using nitrate as electron acceptor while oxidizing Fe in anoxic conditions have been observed (Hauck et al. 2001). However, although the oxidation of Fe^{2+} minerals coupled with NO_3^- reduction yields enough energy for ATP synthesis and microbial growth to be lucrative, empirical evidence of pure culture autotrophic nitrate-dependent ferrous iron oxidation is scarce (Weber and Coates 2007). Instead, it seems some additional electron donors are required for metal oxidation.

Already in 1982 microbes were observed with SEM in the Baltic Sea ferromanganese concretions (Ghiorse and Hirsch 1982). In the study a myriad of different iron and manganese depositing microbes were found on the surfaces of western Baltic Sea ferromanganese concretions. Moreover, for instance Baturin and Dubinchuck (1983) observed numerous ultra-microstructures in the concretions; including coccomorphic, tubular and boom-shaped forms. According to the study of Hu et al. (2000), there is clear evidence of microbial origin in the formation of the IMC's. They found two distinctive microbe types from the ferromanganese nodules of the deep Pacific Ocean which accumulate ferromanganese minerals. The study states that metallic minerals are only found from areas where the microbes propagate. However, the literature on shallow-water formed ferromanganese concretions like those occurring in the Baltic Sea is much lesser than the literature on the deep-water formed ferromanganese concretions (Zhang et al. 2002). Some studies (e.g. Duan et al. 1996) also suggest that sedimentary concretions operate as nature's biofactories for certain microbes. Duan et al. noticed that the microorganisms were much more numerous in the concretions than in the

surrounding sediments. Still, a lot of variations occurred between different concretions.

It is suggested that biofilms could work as intermediaries for mineral precipitation in extreme microcosms such as ferromanganese concretions (Edwards et al. 2005 and references therein). When these studies are applied to the formation of ferromanganese nodules, according to Wang and associates (2009a), two focal scenarios can be envisaged: a) the formation of biofilm on the surface of the concretions and b) centrifugal accretion within the existing mineral deposition (i.e. inside the concretion). Both Fe and Mn depositing and reducing microbes have been since identified on the surfaces of spheroidal concretions and within them (Yli-Hemminki et al. 2014).

2.2 Concretions and the Baltic Sea

The modern Baltic Sea is a relatively shallow sea, and the second largest brackish water body in the world, formed around 8500–8000 cal years BP (Berglund et al. 2005). The sea is vulnerable to alterations in oxygen conditions as the basin is very isolated and is surrounded by areas of high agricultural discharge (Conley et al. 2009). This is because the exchange of water is limited by the Danish Straits which allow the sea to maintain a rather low salinity of ~7‰ (Leppäranta and Myrberg 2009). Fundamental characteristics of the sea also include an average depth of 54 m and a permanent salinity stratification. This stratification hampers vertical convection generating weakly oxygenated or anoxic bottoms. Anthropogenic impact has further increased oxygen consumption through eutrophication (Leppäranta and Myrberg 2009). The basin sits on an old depression in the bedrock and was covered by the Eem Sea before the latest glaciation. Like the other major brackish water basins in the World Ocean, the Baltic Sea developed into a brackish water body during the Holocene (Leppäranta and Myrberg 2009).

Since the end of the last glaciation event, Late Weichselian, the basin has been subjected to both isostatic and eustatic changes and experienced a succession of different marine and littoral stages (Andrén et al. 1999). The first stage after the onset of the latest deglaciation was the freshwater Baltic Ice Lake 12 500 – 10 000 cal years BP (Jensen 1995). It was followed by the Yoldia Sea stage around 10 000 – 9500 cal years BP and

involved two freshwater and one brackish water phase in between (Svensson 1989). Next became the Ancylus Lake which was then succeeded by a precursor of the modern Baltic Sea, the Littorina Sea, after a transitional phase called the Mastogloia Sea from around 8000 to 7500 cal years BP. The Littorina Sea which was the most saline stage of the Baltic Sea took place from ca. 7 500 to 4000 cal years BP and was followed by the recent Baltic Sea (Andrén et al. 1999). The modern salinity levels were reached around 2000 years ago (Leppäranta and Myrberg 2009).

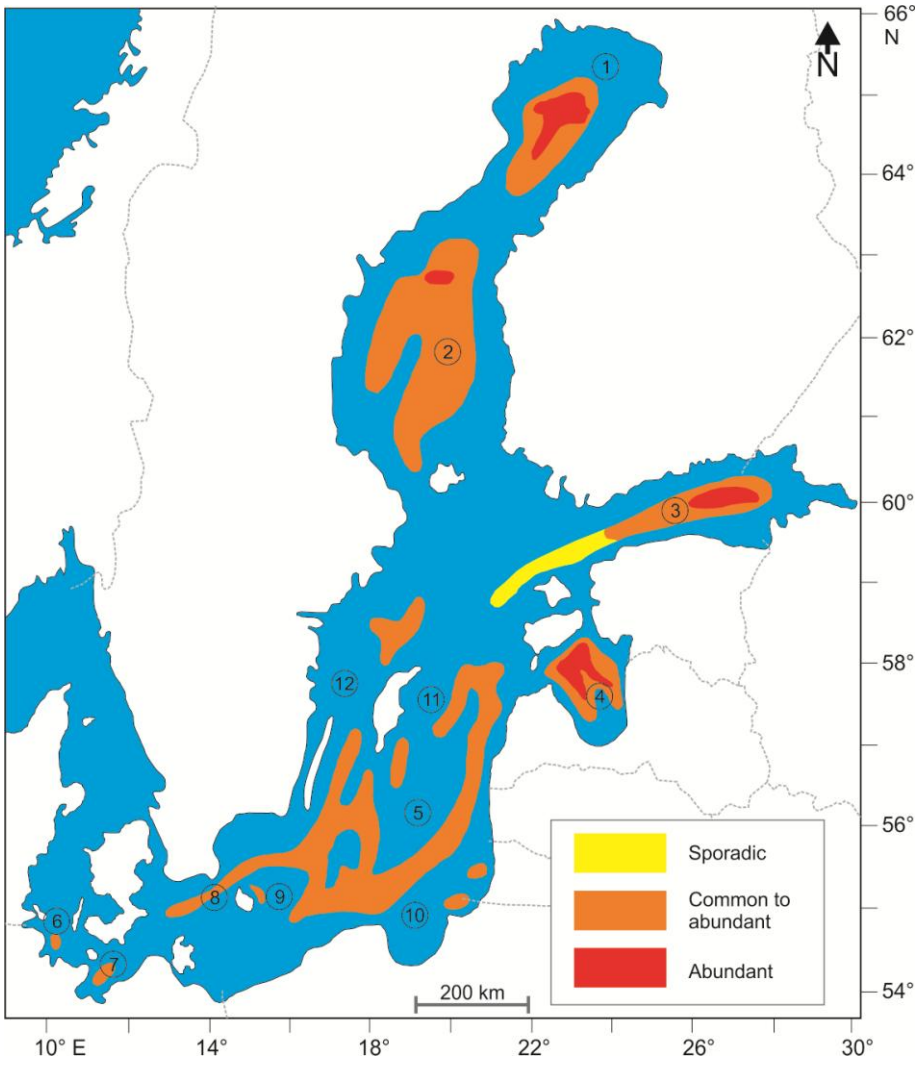

Figure 2. Illustration of major areas of interest in the Baltic Sea and the distribution of ferromanganese concretions. Concretions are found at the fringes of deep basins. Mn-rich spheroidal concretions predominate in the most abundant concretion fields in areas of Gulfs of Bothnia, Finland and Riga. 1: Bothnian Bay; 2: Bothnian Sea; 3: Gulf of Finland; 4: Gulf of Riga; 5: Baltic Proper; 6: Bay of Kiel; 7: Mecklenburg Bay; 8: Arkona Basin; 9: Bornholm Basin; 10: Gdansk Deep; 11: Gotland Deep; 12: Landsort Deep. (Modified: Glasby et al. 1997)

Lithotectonically the area around the Baltic Sea can in a simplified way be divided into

a few major blocks (Reimann et al. 2000). Fennoscandian Shield predominates in Finland, large areas of Sweden and the north western parts of Russia. Baltic States, Russia, Denmark, most of Poland and some areas in Germany are part of the Eastern European Platform. In contrast, major parts of Norway and some areas of Sweden are underlain by the Caledonian mountain chain. Eastern European Platform is the most complex in terms of different lithogenic units, beholding Ceno-, Meso-, and Paleozoic and Proterozoic units. On the other hand, the Fennoscandian Shield comprises mainly of Proterozoic and Archean rocks whereas areas in Norway and some parts of Sweden are Proterozoic and Paleozoic. The sediments in shallow seas are mainly terrigenous in origin in addition to some chemical and biogenic sediments (Bridge and Demicco 2008, p. 473). The sediments within the Baltic Sea basin have also greatly been influenced by both the surrounding terrestrial lithologies and glaciogenic, fluvial and to some extent eolian erosion of the surrounding areas during recent geological timeframe.

The modern Baltic Sea is comprised of numerous basins (Leppäranta and Myrberg 2009), including the Baltic Proper and Gulf of Finland for instance (Figure 2). Most of the sediments in the area of the Baltic Sea are clastic sediments such as silty-clays and sands with common occurrences of muds. Although soft bottoms such as clays, silts and muds predominate, some large areas of sandy bottoms or hard bottoms such as tills or bedrock are common (Winterhalter et al. 1981). In addition, biochemical sediments, such as the ferromanganese concretions are abundant in the Baltic Sea.

The samples for this study were collected from the north eastern parts of the Gulf of Finland. The Gulf of Finland has unique biogeochemical and physical properties although it is almost a linear continuation from the Baltic Proper (see Figures 2 and 5; Pitkänen et al. 2008). This area of the Baltic Sea is especially vulnerable to alterations in oxygen conditions, mainly caused by relatively large external input of phosphorus and nitrogen in addition to the rather shallow depth of the Gulf. Moreover, the Gulf has a distinct but unstable stratification of salinity. Occasionally these forcings may give rise to hypoxia or anoxia of the bottom waters and to cyanobacterial blooms caused by the subsequent release of phosphorus (Pitkänen et al. 2008). Although the loading of nitrogen has recently decreased, the last decade or so has been marked by increased inorganic P concentrations of the deep waters especially during winters, caused by low oxygen conditions.

Generally speaking the concretions are found (Figure 2) at depths of around 40–100 m at the fringes of deep basins (Glasby et al. 1997). The concretions are also found at depths of around 3–100 meters especially on the eastern parts of the Gulf of Finland (Zhamoida et al. 2007). Spheroidal concretion fields commonly occur at the fringes of deep basins and at boundaries of anoxic and oxic systems. These brackish water variants of ferromanganese nodules seem to be more independent in relation to the water depth when compared to limonites (Ojala 2008) or deep ocean nodule deposits for instance (Wang et al. 2011). Winterhalter (1966) has approximated that around 10 % of the Baltic Sea in areas of Saaristomeri, Pohjanlahti and Suomenlahti is covered in ferromanganese concretions. These estimations are of course open for change as more data accumulates. The morphology of the nodules seems to be governed by the sediment characteristics and relief of the seafloor (Zhamoida et al. 2007).

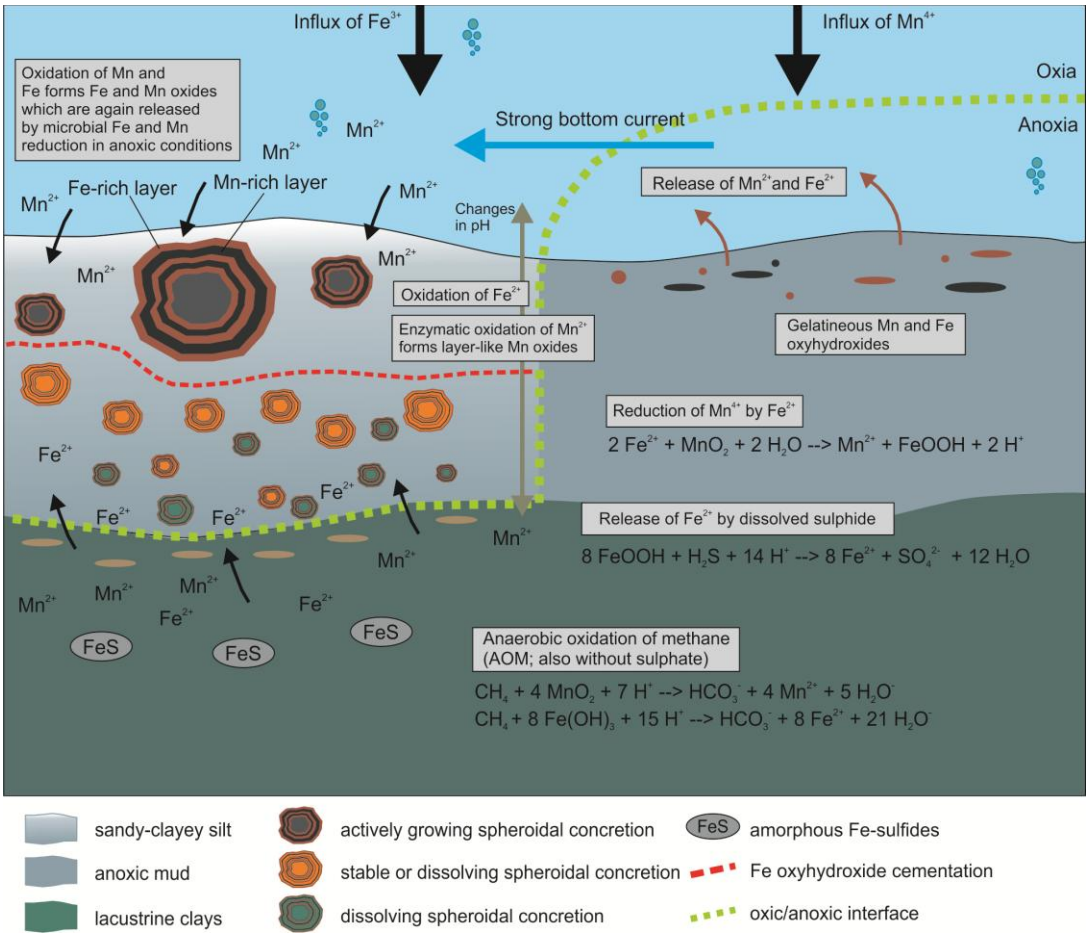

Figure 3. Schematic idealization of focal growth and evolution mechanisms of spheroidal ferromanganese concretions. Illustration is based on Glasby et al. 1997, Miyata et al. 2007, Zhamoida et al. 2007, Ojala 2008, Wang et al. 2009a, Och et al. 2012, Egger et al. 2015.

Usually they are present in areas where sedimentation rates are low or non-existent (Winterhalter 2004). The seasonal redox cycling, low depositional rates and the erosional conditions favor the formation of ferromanganese concretions (Glasby et al. 1997). This occurs especially in areas where the sedimentation rate of organic material is low (Ingri 1985) and commonly where the bottom sediments are recent silty-clayey mud (Zhamoida et al. 2007). Occasionally they are seen in Holocene marine silty-clayey muds as well. The underlying sediments are mainly older lacustrine clays or limno-glacial clays. Chiefly, the concretions occur at a depth of < 0.5 m within the sediment.

In the case of spheroidal concretions, the sediment column can be divided into zones of 1) active accumulation and growth, 2) stable layer where dissolution and growth rates are nearly equal and 3) layer of concretion dissolution (see Figure 3, Zhamoida et al. 2007). All the mentioned zones are usually observed in the top ~20 cm of the sediment column. Moreover, especially the spheroidal ferromanganese concretions seem to form in areas with strong bottom currents (Glasby et al 1997). The bottom currents bring both oxygen rich water from more oxygenated areas and also work as a supply for the reduced Mn and Fe and other metals from anoxic waters – gelatineous Fe and Mn oxides formed in adjacent mud-rich and oxygen-poor areas are thermodynamically unstable and may be flushed to more suitable areas by currents (Emelyanov 1986). The lateral migration of the metals from these mud zones is believed to be the main source of metals for spheroidal concretions (Zhamoida et al. 2007, Winterhalter 2004, Glasby et al. 1997). However, vertical migration of the reduced forms of the metals within the sediment column may be an equally important source in a similar process as suggested earlier (Och et al. 2012, Egger et al. 2015). This is because in low-sulphate environments Fe and Mn (oxyhydr)oxides are candidates for AOM which then releases Fe^{2+} and Mn^{2+}.

Many studies have also tried to determine the growth rate of the nodules. These include calculations of concentric growth rings which were then regarded as annual, and later other methods including helium isotope studies (Anufriev et al. 2005, Anufriev and Boltenkov 2007), accumulation rates of metals (Marcus et al. 2004) and ^{210}Pb dating (Zhamoida et al. 2007, Grigoriev et al. 2013). All the recent dating studies carried out suggest that the growth rate of the nodules is generally speaking < 10 mm kyr^{-1} (Marcus et al. 2004, Anufriev et al. 2005, Anufriev and Boltenkov 2007, Zhamoida et al. 2007,

Grigoriev et al. 2013). The growth rate, however, is greatly affected by the local micro-environmental changes. Some mussels with ferromanganese nodule aggregates on top of their shells (Ghiorse and Hirsch 1982, Glasby et al. 1997) have been found, alongside with a beer bottle cap embedded in a coating of ferromanganese precipitates (Zhamoida et al. 2007). Thus the growth rate is geologically speaking a fast one in comparison to other oceanic nodules (Wang et al. 2011), hence traditional dating methods including ^{231}Pa, ^{234}U, and ^{10}Be are hampered (Anufriev and Boltenkov 2007). The growth speed is also suggestive for biogenic origin of the concretions.

Zhamoida et al. (2007) note that the concretions might act as a redox buffer system. Most of manganese found in the concretions is on its tetravalent state and iron in its trivalent state (Arif and Blinov 2004). Abundant concretion fields are found on the boundary layers of oxic and anoxic systems. In these situations manganese can act as a buffer for oxygen level fluctuations because of the relatively easy transformation from Mn^{2+} to Mn^{4+} (Zhamoida et al. 2007). Furthermore, manganese and iron ratio correlates with the morphology of the concretions. Usually spheroidal concretions have comparatively high Mn/Fe ratios (Glasby et al. 1997). E. g. in the study of Anufriev et al. (2005, Anufriev and Boltenkov 2007) the chemical composition of the IMC's of the Baltic Sea was determined, which suggested that the Mn/Fe ratio of the concretions was ~3.5. This can alter as well depending on the circumstances – especially the supply of manganese from adjacent areas or the dissolution of metal oxides in anoxic conditions greatly affects the availability of manganese and in less extent iron (e.g. Glasby et al. 1997, Winterhalter 2004, Zhamoida et al. 2007). In some cases, the Fe/Mn ratio can give insights of the spatial arrangement of the concretions (Glasby et al. 1997). It has been shown that a decrease in Fe/Mn ratio is related to distance from river mouths.

On the other hand, determining the mineralogy of the ferromanganese nodules is challenging as most of the solid matter present in the concretions is amorphous or poorly crystalline (Bogdanova et al. 2008). Main constituents of the IMC's are Mn- and Fe-oxyhydroxide, -hydroxide and -oxide precipitates (generally in the form of [MO_xOH_y; as $Mn^{4+}O_xOH_y$ or $Fe^{3+}O_xOH_y$] (Wang et al. 2011)) including minerals goethite, todorokite, ferrihydrite and birnessite, feroxhyte, akaganeite, lepidocrocite, and hematite among some amounts of other minerals (Winterhalter 1966, Glasby et al. 1997, Bogdanova et

al. 2008). In many studies poorly crystalline iron compounds are regarded as amorphous because of the ultrafine epitactic intergrowths of different manganese and iron minerals. This makes the actual mineralogical determination difficult. Occasionally dehydration of the sample may lead to phase changes, for instance a possible transformation of todorokite to birnessite (e.g. Zhang et al. 2002, Glasby et al. 1997). Many of the Fe phases characterized in the nodules have also been observed as an end product of biomineralization (Weber and Coates 2007). These include two line ferrihydrite, goethite, lepidocrocite, and hematite. Microbes are able to form all of these minerals in circumneutral pH also in anoxic conditions. Similarly, todorokite and birnessite are generally believed to be the result of biomineralization (Zhang et al. 2002, Miyata et al. 2007). Mineralogically speaking, first and foremost birnessite- and todorokite-like mineralisations can absorb and substitute for numerous different metal cations. Birnessite is basically composed of MnO_6 sheet of octahedra with 7-Å interlayer configuration (Post 1999). These interlayer spacings are occupied by cations such as H^+, Na^+, K^+, Mn^{2+} and Ca^{2+} alongside water molecules. Some recent studies show biogenic Mn^{4+} oxides with birnessite like structures (Miyata et al. 2007). Fe (oxyhydr)oxides, on the other hand, are able to absorb numerous anionic ligands as mentioned previously. When discussing the Baltic Sea, one of the most important elements adsorbing efficiently to iron oxides is phosphorus (van der Zee et al. 2003).

The capability of endorsing different metals and elements has both risen an interest in exploiting the concretions economically and a concern for the environment: on one hand, the concretions contain such a high amounts of manganese and REEs to account them as ores (Zhamoida et al. 2004) whereas on the other hand, the dissolution of the concretions has given emphasis to the possible effects of e.g. the release of phosphorus to the surroundings and the subsequent influence to eutrophication (Lehtoranta 2003, Zhamoida et al. 2007, Pitkänen et al. 2008).

3. MATERIAL AND METHODS

Ferromanganese concretions supplied by the Finnish Environment Institute were used to study the concretions' physicochemical properties. For the study nine samples were selected in total. All of these samples were spheroidal. Six samples were chosen for

study with the X-ray tomography method (CT), of which four were chosen for visualization (Figure 4). Furthermore, JWTomo3 and JWTomo5 were chosen to dissolution experiment. They were incubated in Anaerogen containers for a duration of 2 months after which they were reimaged with CT.

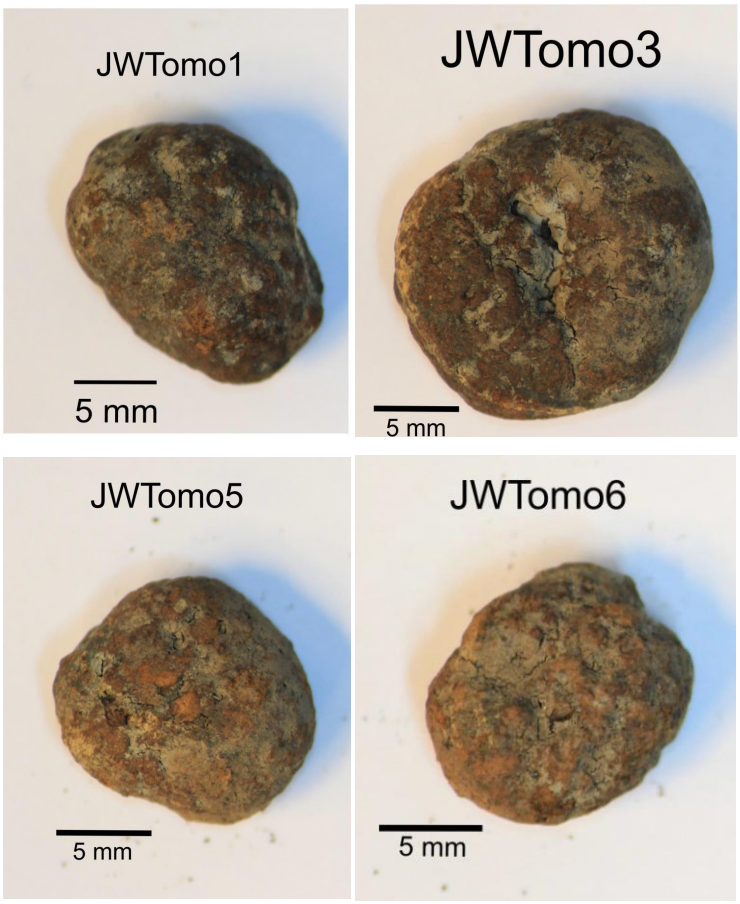

Figure 4. Spheroidal concretion samples studied with X-ray tomography. Samples JWTomo1, JWTomo5 and JWTomo6 show granular surface texture, whereas JWTomo3 has some dissolution features and smoother surface.

From the remaining three spheroidal samples two were chosen to be studied with X-ray fluorescence analysis (XRF) and one of them to be studied with the Electron Probe Micro-Analyzer (EPMA). Furthermore, liquids from the dissolution experiments were also analyzed with XRF whereas metallic precipitates which accumulated to the sample bottles were analyzed with EPMA. Finally, the two solid samples studied with XRF were also ignited to determine loss on ignition (LOI).

All of the samples show granular or slightly granular to smooth surface texture with

some dissolution features. The diameter of the samples ranges from ~1.0 cm to ~2.0 cm. The samples were collected from a silty-clayey bottom from the eastern Gulf of Finland near Haapasaari with Box Corer and van Veen (Figure 5).

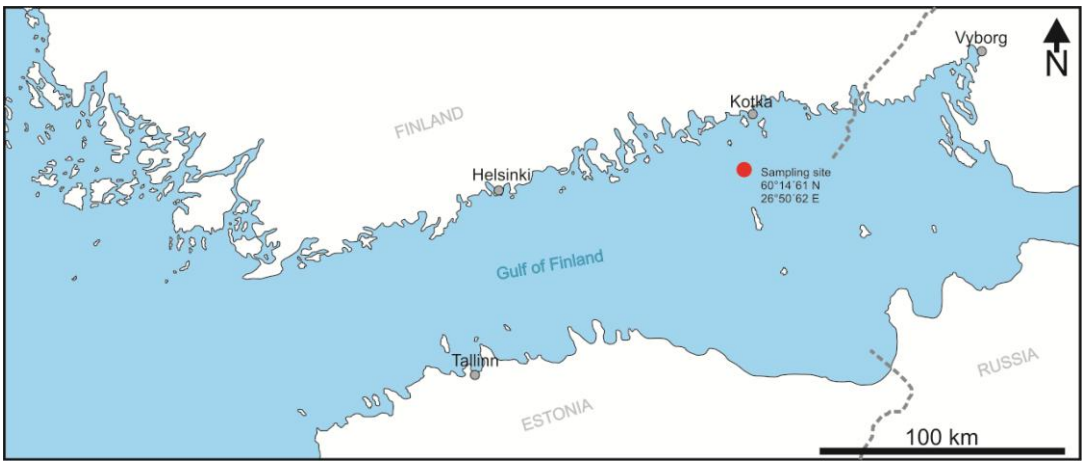

Figure 5. Map of the sampling site and the surroundings of the sample spheroidal ferromanganese concretions. The sampling site is depicted as a red dot in the map.

The concretions for the X-ray microtomography were measured using a digital caliper and then photographed. Using a 3D printer (Makerbot), specific test tubes were rendered for each of the samples.

3.1 X-ray tomography

The X-ray tube used in the imaging is Phoenix X-ray 180 nanofocus and the detector is Hamatsu Flat Panel C7942SK-05. Theoretical maximum spot resolution is ~250 nm px^{-1} but in practice the resolution is determined by the sample size giving the actual resolution 9.5 μm px^{-1} for the spheroidal concretion samples. The X-ray beam was also filtered with 0.5 mm of copper. For more detailed information see Appendix B.

3.1.1 Sample preparation

Six spheroidal samples were named from JWTomo1 to JWTomo6 for the X-ray

tomography imaging. Each sample was then put into a plastic petri dish and moved to a fume hood overnight for drying in 105°C.

Next the samples were put into a plastic test tube and supported with cotton wool to keep the samples from moving. Also, the samples were aligned parallel to the rotation axis of the test tube. This however brought some problems in the first runs as the test tube and the cotton wool didn't support the samples properly, also the tube's cap was rounded so it affected the positioning of the tube. Because of this, a 3D printer was used to render a test tube specific for the dimensions of each concretion. For this, the exact parameters (diameter) of the IMC's were measured using a digital caliper. Six specific test tube pieces were created for the JWTomo1 to JWTomo6 samples with MakerBot. Some of the samples were supported with cotton wool. Four samples (JWTomo1, JWTomo3, JWTomo5 and JWTomo6, respectively) were chosen for visualization and analysis (Appendix A).

3.1.2 The elements of X-ray tomography

A spectrum of different analytical applications for X-rays exists, yet the X-ray computed tomography (X-ray CT) has only recently become emphasized in mineralogical and geological research as a nondestructive tool. X-ray computed tomography is an imaging method in which incident X-ray beams are directed to a sample in a purpose of creating cross-sectional images of the sample by illuminating it from different angles. These images can be reconstructed to form a three dimensional rendering. In general, a sample can be reconstructed from transmission or diffracted data depending on the method by which the samples are illuminated. The illumination can be generated by ultrasound, electromagnetic radiation (in this case the X-rays) or magnetic resonance imaging. (Cnudde et al. 2006)

The principle of the technique is that a sample is positioned between an X-ray source and a detector. Because the sample is needed to be imaged from multiple angles, a rotational platform is typically used. To construct the images, a computer algorithm based on an algorithm called FDK by Feldkamp et al. (1984) is usually used to calculate the cross-sections or slices through the sample. In this case, only a 180° rotation is required. Furthermore, because the X-ray beam geometry is conical the magnification can be altered by moving the sample between the source and the

detector. Thus, the closer the sample the higher is the spatial resolution. However, for instance the pixel size of the detector, focal spot size of the X-ray tube and the size of the sample affects the spatial resolution also. (Cnudde et al. 2006). In our imaging the samples were rotated 360° in 0.4 degree intervals.

It is known that X-rays are absorbed to different elements and compounds on different intensities based on their mass density (or the atomic number to be precise). In essence, heavier elements absorb X-rays much more efficiently than lighter ones as the heavier elements are usually a lot denser (Cnudde et al. 2006). As X-rays collide to a material they are attenuated directly proportional to the material's density and the intensity of the X-rays (Whiston 1987, p. 14). Hence, different phases can be distinguished from the samples and a 3D structural analysis can be made. It should be remembered, however, that the electron density map reconstructed from the analysis data only shows the differences between the densities of the materials and thus does not *de facto* give insights of the (chemical) composition of the sample material. Some studies have been made with dual gamma-ray CT scanner in order to differentiate the mineral composition of deep sea ferromanganese concretions (Rizescu et al. 2001). According to the results, two different phases were differentiated, i.e. abyssal clays and ferromanganese minerals. Working with the X-ray CT instead, caution is advised while interpreting 'real densities' quantitatively. This would require extensive work with scanning of specific calibration materials and their comparison to the samples. However, in this study, a combination of EPMA and CT was used to canvass if the chemical composition and the spatial arrangement (density) can be somehow related.

3.1.3 Analysis and visualization

All the slices created from the samples were converted to 16-bit grayscale images with 2^{16} = 65536 separate grayscale values. The known voxel volume is ~860 μm^3 thus giving the actual voxel size 9.5 x 9.5 x 9.5 μm isotropic. The distance ratio is 0.105 pix μm^{-1}.

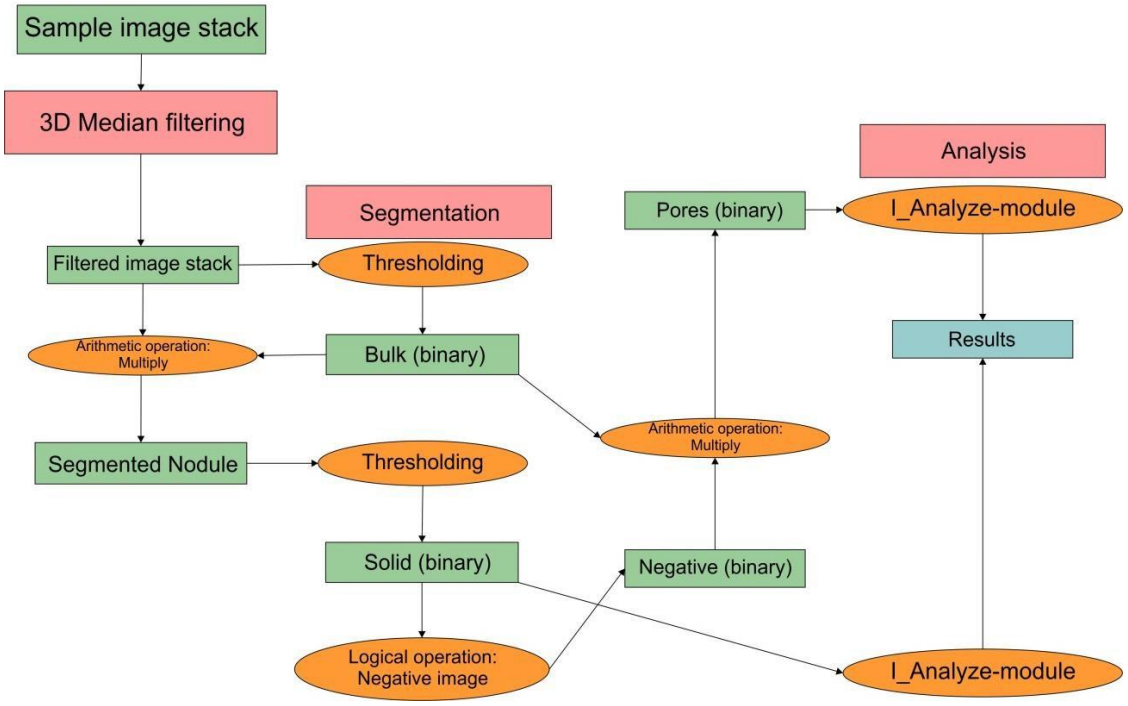

Figure 6. Flow diagram describing the work phases of pore space and bulk material segmentation and analysis from tomography images of the ferromanganese concretions using Avizo Fire.

Processing of the tomography images was completed using Avizo Fire, a commercial program for tomography and 3D image analysis suited especially for earth sciences. The processing (Figure 6) started with setting scale to the images and filtering of the image stack using a median 3x3x3 kernel filter. The filtering removed noise and small details, but also made the boundaries of solid matter and pores smoother which in turn makes the segmentation and the analysis easier to compute.

After that, the next step was the segmentation of the pores. This was achieved by thresholding the slices in three different phases. Two distinct grayscale value peaks were interpreted from the histogram of the image stack. As the surrounding air was also characterized as pores due to their similar grayscale values, the first step was to distinguish the interior and the exterior of the sample. This was done by selecting all the grayscale values which comprise the solid material of the nodules. Then the selection was filled so as to produce a binary image (referred as Bulk from now on) in which the bulk material (i.e. the nodule) and the exterior air were separated. This was followed by the segmentation of the pores from the interior material. The

Bulk was used as a mask to differentiate the exterior air from the solid matter from the filtered grayscale image stack (referred as Segmented Nodule in Figure 6). Next the thresholding process was repeated and a binary image of the pore space and interior solid material was created (referred as Solid from now on). Because the pore space would now logically have the same binary values as the exterior air has in the Bulk, a negative image stack of the Solid was created. The negative image mask was then multiplied with the Bulk to produce a segmented image stack in which only the pore space is distinguishable. Finally, using the I_Analyze module of Avizo Fire, the pore network's volume and surface area and the nodules solid material volume was calculated. The results are presented in Table 1. Vizualisation of the samples was done using VG Studio and Avizo Fire.

3.2 Loss on ignition

Two spheroidal samples (JWXRF1 and JWXRF2) were chosen to be studied with the loss on ignition method (LOI). The objective was to determine the porosity of the ferromanganese concretions by measuring the weight changes of the spheroidal samples when 1) wet, 2) after being kept in room temperature until no significant change in mass occurred, 3) hot air oven in 105 °C and finally 4) in a muffle furnace in 550 °C and 5) 1000 °C. Storing the samples in room temperature was to differentiate the amount of primary vaporization from the largest pores. Heating the samples in the hot air oven removed rest of the porous water. By igniting the samples in furnace the amounts of organic matter, crystallization water and carbonates could be estimated also. In the test setup the size of the samples, exposure time, position of the samples in the furnace and the laboratory measurements affect the results (Heiri et al. 2001). Therefore, these parameters were taken in to consideration while testing.

First, the wet samples were weighed with the Precisa XR 205SM-DR scale in glassy petri dishes. Then the samples were moved to a hot air oven. The samples were then weighed after being in the hot air oven in 25 °C for 2 hours. After that the samples were put in to a cupboard under a protective sheet in room temperature for 16 hours. Then a new weighing was made. After that the procedure was repeated and the new weighing

was made after keeping the samples 40 hours in room temperature. Finally, after 64 hours no change in mass occurred. Thus, the samples were put into a 105 °C hot air oven for 5 hours. This was made again the next day to ensure no more mass changes occurred.

In the next phase four crucibles were pre-ignited on a Nabertherm muffle furnace in 550 °C for 1 hour. Then the crucibles were moved into a desiccator overnight. Afterwards, the crucibles were weighed with the Precisa scale. Then JWXRF1 was grinded and ignited in the muffle furnace. JWXRF2 was chosen to be analyzed with XRF without igniting it beforehand. However, the Claisse gas fluxer used measures the LOI amount. In addition, igniting to remaining JWXRF2 powder was made afterwards. The igniting was done in 550 °C and in 1000 °C for three hours in both temperatures.

3.3 XRF and EPMA

The X-ray fluorescence (XRF) device used in this study is the Department of Geosciences and Geography's and Department of Material Physics' WD-XRF type PANalytical Axios mAX spectrometer. The setup used was 3 kW; acceleration voltage was set to 60 kV and the probe current to 50 mA. For the XRF beads a vacuum medium was used whereas for the liquid samples He-atmosphere was utilized. The beads were analyzed with standardized quantitative settings and the liquid samples with semi-quantitative standardless Omnian settings. The electron probe micro-analyzer (EPMA) used in this study is the Department of Geosciences and Geography’s Jeol Superprobe JXA 8600. The acceleration voltage used was 15 kV and the probe current was at 1 nA.

3.3.1 Sample preparation and analysis

Two spheroidal samples named JWXRF1 and JWXRF2, and two liquid samples were prepared to be studied with the X-ray fluorescence analysis with PANalytical Axios mAX spectrometer. One spheroidal sample named JWEPMA was also chosen to be studied with Electron Probe Micro-Analyzer Jeol Superprobe JXA 8600. On top of that, microprobe preparates were done of the precipitates accumulated to the sample bottles in the dissolution experiment. Both the thin sections and liquid samples were named

after the dissolution experiment samples, JWTomo3 and JWTomo5, respectively.

First, the samples JWXRF1 and JWXRF2 were ground in a Fritsch pulverisette 6 grinder in a tungsten carbide container with four tungsten carbide spheres. The runtime was set to 5 minutes with a speed of 300 rpm. No ethanol was added. One of the pre-ignited crucibles was weighed with a Precisa XR 205SM-DR scale. Then around 0.7 grams of the ferromanganese powder of sample JWXRF1 was measured to the crucible. After that, the crucible was put in to the muffle furnace and ignited in 1000 °C for 3 hours. The sample was then moved into a desiccator for 24 hours. The igniting hardened and aggregated the powdered material so that it had to be crushed with a plastic spoon before it could be weighed again. Afterwards, slightly under the recommended amount of 0.6 g of substance (0.5889 g) was weighed and 6.0 g of $LiBO_2$-$Li_2B_4O_7$-LiBr flux was added. Then the mixture was processed to an XRF bead with Claisse M4 gas fluxer. Thus, it must be noted that there might be minor inconveniences with the results. However, these will likely be marginal as the PANalytical Axios mAX has detected 0.06 gram sample size with satisfactory accuracy (according to test runs with the machine). The second sample, JWXRF2, was decided not to ignite before making it a bead. It was processed directly after grinding and 0.6001 grams was measured to the platinum crucible for the gas fluxer. JWXRF2 was ignited afterwards instead.

For the liquid samples, the contents of the sample bottles (Figure 7) were vacuum filtrated. Then the filtrated liquid was stored in sample vessels for XRF (~20 mL). Moreover, precipitates accumulated on the filters were scraped to a thin section glass, dried, and prepared for microprobe analysis. They were also carbon coated.

JWEPMA was placed into epoxy and cut in half to produce two hemispherical sample buttons which were then polished. The more presentable of the buttons was chosen to be studied with EDS analysis. The sample was neither carbon nor gold coated as it consists mainly of iron and manganese compounds so the button ought to be conductive. Instead, conductive tape was used to avoid overcharging of the sample. In addition, due to the porous nature of the nodules, the topography of the sample surface introduced some inconsistencies for the analysis and thus extra care had to be taken while analyzing.

Fe, Mn, Al, P, Ca, As and Si were analyzed in the EDS element mapping of JWEPMA. Each element was analyzed for ~20 minutes per area of interest. EDS linescan, on the other hand, was done manually by choosing the best possible location for spot analysis

with an interval of ~70 μm between spots giving 6.195 mm the overall line length. The analyses were done mainly with qualitative EDS analysis because of the porous nature of the sample, but nevertheless the results can be considered scientifically accurate due to the precision of the instrument. Also the most representative line was chosen for EDS linescan based on interpretations from CT scanning and EPMA. For the precipitate samples JWTomo3 and JWTomo5, a qualitative spot analysis was done with EDS. Data for spot analyses and line scan route are in Appendix F.

3.3.2 Introduction to XRF and EPMA

The principles of X-ray methods are usually linked to the characteristic behavior of different elements when affected by electromagnetic radiation or electron beams. When incident X-ray beam hits to a material, part of it is diffracted and passed through, and part of it is absorbed by the material (Whiston 1987). When the elements of the material are bombed by the high intensity X-rays, the atoms get excited and may lose some inner shell electrons and form vacancies. The same occurs when the atoms are bombed with high intensity electron beam, like in the case of microprobe or SEM. Then, so called electron transitions take place when the outer shell electrons fill the vacancies. These transitions produce characteristic X-rays which are unique to different elements and thus they are a tool of determining the chemical composition of a sample material. The X-rays emitted by a specific element or compound have a distinctive wavelength which can be calculated to be inversely proportionate to its energy (Brouwer 2003). There is a simple equation (10) that shows how energy E (keV) is related to the wavelength (λ):

$$E = \frac{hc}{\lambda} \qquad (10)$$

In the equation, h is Planck's constant (keV) and c is the velocity of light (nm). The wavelength dispersive X-ray fluorescence analyzer differs from the energy dispersive XRF (or EDXRF) analyzer by the detection system. In the WDXRF an X-ray tube shoots a high intensity X-ray beam to the sample and measures the emitted wavelengths which are then dispersed by an analyzing crystal. The crystal acts as a color separator and shoots the so produced colors (wavelengths) to different directions. The detectors are able to measure the intensities of different wavelengths.

Thus, the results are based on the intensity differences of each detected wavelength. (Brouwer 2003)

EPMA consists of various components of which the most important are: the electron gun, rotary vane vacuum pump, vacuum line system, oil diffusion pump, filament, and analysis detectors. The EDS detection system analyzes the sample by using a 'Si (Li) drifted' detector, which detects characteristic photons given off from the sample. The detector is also doped with lithium and boron, which act as diode that accepts and donates electrons. The high voltages used with the spectroscopy results in the necessity of cooling by liquid nitrogen in order for the lithium in the detector to remain stable. As the X-ray's diffracted energy hits the detector, a pulse current is created and this is what is measured to ascertain the sample's properties (Lawes and James 1987).

3.4 Dissolution experiment

Dissolution of JWTomo3 and JWTomo5 were studied in anoxic conditions. After initial CT scanning the sample concretions were rejuvenated in aquarium with other nodules from the sample location (Figure 5) a period of one week.

Figure 7. Sample bottles for dissolution experiment. JW3 = JWTomo3 and JW2 = JWTomo5

Afterwards, they were put into sample bottles with 100 mL of Helsinki-water (Figure 7 and Appendix E) which were then deoxygenated with N_2 for ten minutes. The sample bottles were incubated in anaerobic conditions for two months in a dark room in 20°C. 100 μL mL^{-1} of vitamins were added. Sodium acetate was used as a carbon source. After a period of two months, the samples were dried and reimaged with CT scanning. Then after a year of removal of the concretions from the sample bottles, the composition of the liquid was analyzed with WDXRF and pH was measured with a pH paper. Around 20 mL of solution was used for the analysis. Then the solutions were vacuum filtrated. The remains of the filtration were collected to thin section glass and carbon coated for EPMA analysis.

3.5 Sources of error and further notices

Mineral phases present in the samples are most probably really poorly crystallized and intermixed based on earlier studies (e.g. Bogdanova et al. 2008) and interpretations of EPMA technician Radoslaw Michallik and the author of this thesis. Thus quantitative mineralogical analysis is difficult to make without XRD or other further mineralogical analysis and so the results EPMA analysis yielded are qualitative. Also the unpolished surface of the epoxy button renders quantitative EDS analysis mostly worthless as the beam cone which hits the analyte surface might penetrate into surroundings because of the uneven surface. However, according to test runs with the instrument also qualitative results can be held scientifically relevant and accurate.

Also all the other laboratory analyses include possible sources of error. For instance common sources of error for XRF and EPMA are random errors such as counting statistics, X-ray tube or electron gun and generator stability and equipment errors; systematic errors including sample errors and equipment errors; standard deviation of measurements and sampling errors. These can be counteracted with e.g. good sample preparation, proper settings and up-to-date calibration of the instrument. However, biggest sources of error come from the analysis and visualization of the CT scanning images, as most of the post-processing is done subjectively. This can be best counteracted with careful and thoughtful processing of the images by the investigator.

Furthermore, some of the analyses done here could have been prepared in a more

thorough way – all the blame is pointed to the author of this thesis. For instance using a pH meter instead of pH paper in the dissolution experiment would have created more reliable results. Also the use of plastic bottles in the experiment instead of glassy ones would have made analysis with ICP-MS possible also enabling the determination of possible trace elements released to the solution. Furthermore, measuring the mass of the precipitates would have given insights of the absolute mass loss or gain during the dissolution experiment.

4. RESULTS

4.1 Inner structure of the concretions

4.1.1 Tomography

Both quantitative and qualitative analyses were made to the samples studied with tomography. The pore 3D surface area, volume and relative pore volume were calculated as well as the nodule surface area, nodule volume and relative nodule area (Table 1). Also a qualitative analysis of the pore networks alignment and structural characteristics of the nodules was made based on the rendered 3D images of the samples.

Table 1. The geometric attributes of the ferromanganese nodule samples and their pore networks. a denotes before and b after the dissolution experiment.

		JWTomo1	JWTomo3a	JWTomo5a	JWTomo6
Nodule area	mm^2	883,28	1883,21	585,82	494,51
Nodule volume	mm^3	1426,98	1607,49	819,53	696,45
Pore area	mm^2	4139,22	3650,24	3263,51	1328,85
Pore volume	mm^3	111,63	322,82	81,6	42,55
Nodule area proportion	%	21,3	51,6	18,0	37,2
Pore volume proportion	%	7,8	20,1	10,0	6,1
Morphology		Spheroidal	Spheroidal	Spheroidal	Spheroidal

		JWTomo3b	JWTomo5b
Nodule area	mm^2	944,01	390,81
Nodule volume	mm^3	1593,00	899,39
Pore area	mm^2	4597,52	1378,7
Pore volume	mm^3	373,68	35,932
Nodule area proportion	%	20,5	28,3
Pore volume proportion	%	23,5	4,0
Morphology		Spheroidal	Spheroidal

All the spheroidal samples have clearly a larger pore network surface area than the nodule's surface area. In essence, the pore networks extend around two to five times greater than the nodules' exterior surface areas. In contrast, the pore networks' volume is only around 20 % to as small as ~6 % compared to the nodules' solid

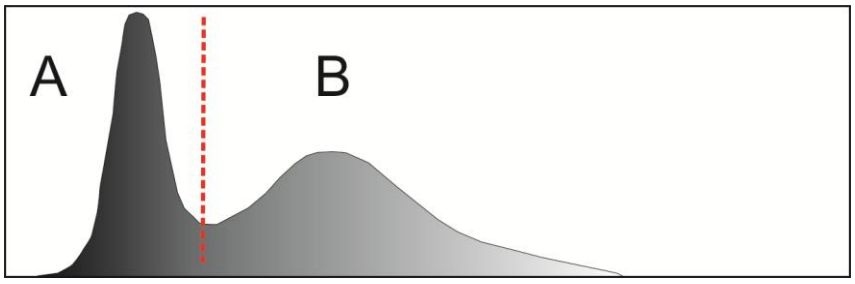

Figure 8. Schematic illustration of a sample grayscale image stack histogram. Generally speaking, all the sample histograms showed two to three distinct peaks. A represents the first peak which comprises the grayscale values of the pore space and the background. B represents the second and third peaks which comprise the bulk material of the concretions.

material's volume. Furthermore, samples JWTomo3 and JWTomo5 showed remarkable change in both volume and area after treatment in anoxic conditions. The pore area of JWTomo3 has increased as much as ~26 % while pore volume has increased ~16 %. Similarly, the nodule area is almost half of its original value but the nodule volume has decreased only slightly (~1 %). In contrast, the pore area of JWTomo5 has decreased ~58 % and pore volume ~56 %. On top of that, nodule area has decreased, being only ~67 % of the initial situation, but nodule volume has slightly increased (~10 %).

Grayscale value differences in the tomography images indicate differences in the density of the media: the layer is more diffuse the darker coloured the image is and *vice versa*. The grayscale image stacks showed bimodal histograms, from which the peaks are interpreted as the background and pore space, and the mineralized bulk material (Figure 8).

In all the spheroidal samples, the most porous areas are concentrated to the core of the concretions. Furthermore, the samples tend to have a larger void in the center of the nodule the bigger the samples are. Also the cavities seem to form circular concentric areas (Figures 9, 10, and sample specific figures later in the text) around the core

following layer boundaries of differing densities. Also all the spheroidal samples have similar internal structure of concentric rings of dense and less dense layers. Similarly, all the IMC's appear to have one especially thick and dense layer radially in between the core and the surface. This dense layer is shown white in Figure 9.

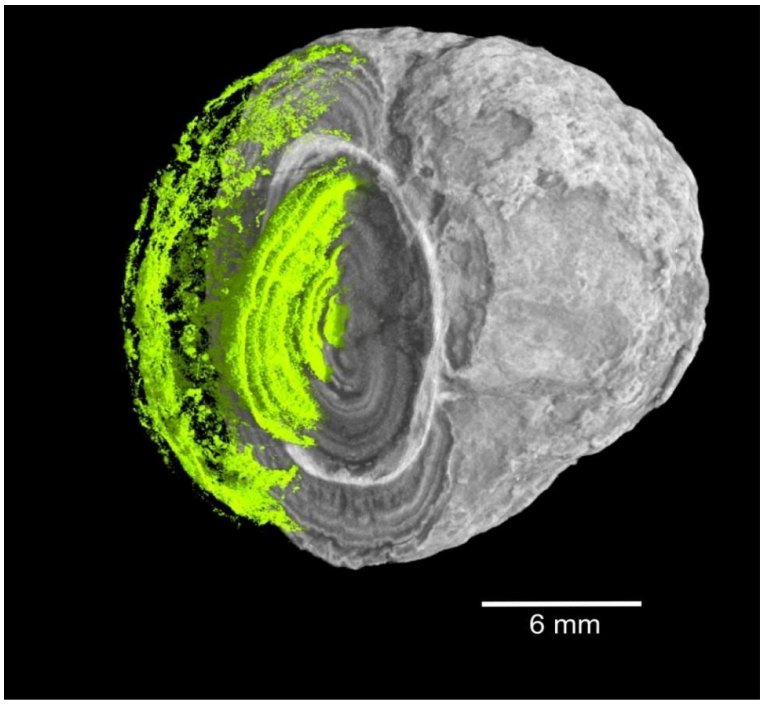

Figure 9. Visualization of sample JWTomo5.The picture shows visible rings of differing composition in the nodule. Lighter colours are more dense and darker colours are more diffuse. The pores are colored green and the pore network is at its densest near the core of the concretion. The pores also seem to be concentrated on the more diffuse layers (darker greyscale values).

Figure 10. A single thresholded black and white slice of sample JWTomo5 image stack. The image reflects that the greatest part of the porosity is concentrated to the center of the concretion and is formed as circular concentric cavities.

JWTomo1 represents a more spherule-like concretion with a slightly elongated form. It shows semi-granular surface texture observable with the naked eye (Figure 4). Eminent features include a complex pore network mainly distinguishable near the core and two thicker and denser zones of which the first is near the core and the other near the rims of the concretion (Figure 11). Layers of differing densities can be observed. The cavities are concentrated to the more diffuse layers and in some cases are nearly concentric particularly in the innermost parts of the nodule. In contrast, the outermost parts show mainly irregularly shaped cavities. Furthermore, the layers do not generally speaking show sharp contacts, hence the transition from a sparse layer to a dense layer is mainly gradual. In the outermost parts of the concretion, the layers seem to be banded and rounded. All of the concretions show a clear growth phase (the layers) and a nebulous dissolution phase (the cavities). Dissolution does not seem to follow a clear pattern from the outermost parts to the interior parts.

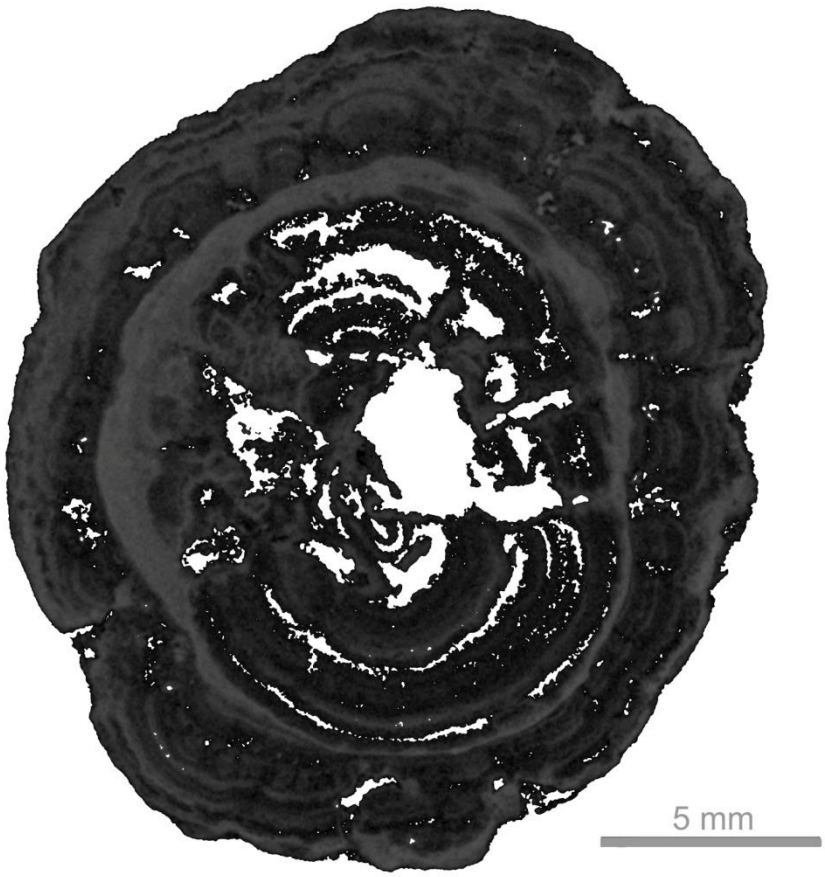

Figure 11. Grayscale slice of the bulk material of JWTomo1. Lighter grayscale values indicate denser material and *vice versa*. White areas represent pore space.

JWTomo3 has a more elongated and flat shape compared to the more spherule-like samples JWTomo1, JWTomo5 and JWTomo6, respectively (see Figure 4). The sample also shows smooth surface texture and is pitted from its other side. The most conspicuous features occurring on the tomography images of JWTomo3 are a large void in the core of the concretion and a rim of dense material surrounding the core (Figure 12).

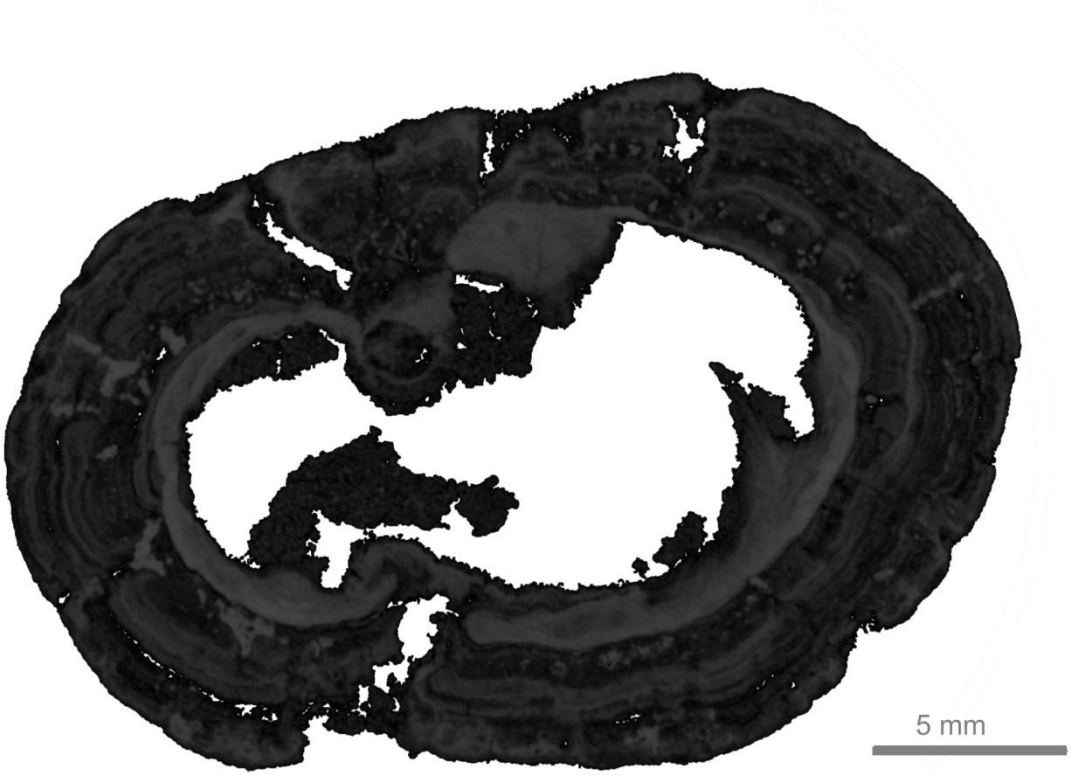

Figure 12. Grayscale slice of the bulk material of JWTomo3. Lighter grayscale values indicate denser material and *vice versa*. White areas represent pore space.

This relatively thick and dense layer seems to predominate throughout the whole sample. Moving towards the rim of the nodule, smaller scale layer-like structures can be observed. Moreover, cavities and pore space seem to be concentrated to the more diffuse layers and often follow a transition from a more dense layer to a more diffuse one. In contrast to the other samples, however, the pore network itself seems to be smaller excluding the large cavity in the core. In other words, the pore network volume is larger in relation to the pore network area compared to the other nodules. Texturally speaking, the sample can be divided into two sub-units. Material seems to be more homogeneous below the thick, dense layer. From the thick layer outwards, however, alternating dense

and sparse sub-layers seem to prevail. In this unit, the banded layers form almost like ripples, or heaving structures. Moreover, denser aggregates can be observed in certain layers. The dense layers also seem to surround cavities in the outermost part of the concretion.

JWTomo5 is a spherule-like concretion with semi-granular surface texture (see Figure 4). Grayscale slices of the sample show texturally two or three different zones (Figure 13). In the innermost part, the material is more homogeneous and a complex network of cavities reigns. These features are separated from the outermost parts by a relatively dense and thick layer which does by no means show a uniform structure. Instead it is thicker from the other side and is disturbed by cavities and areas of lower density.

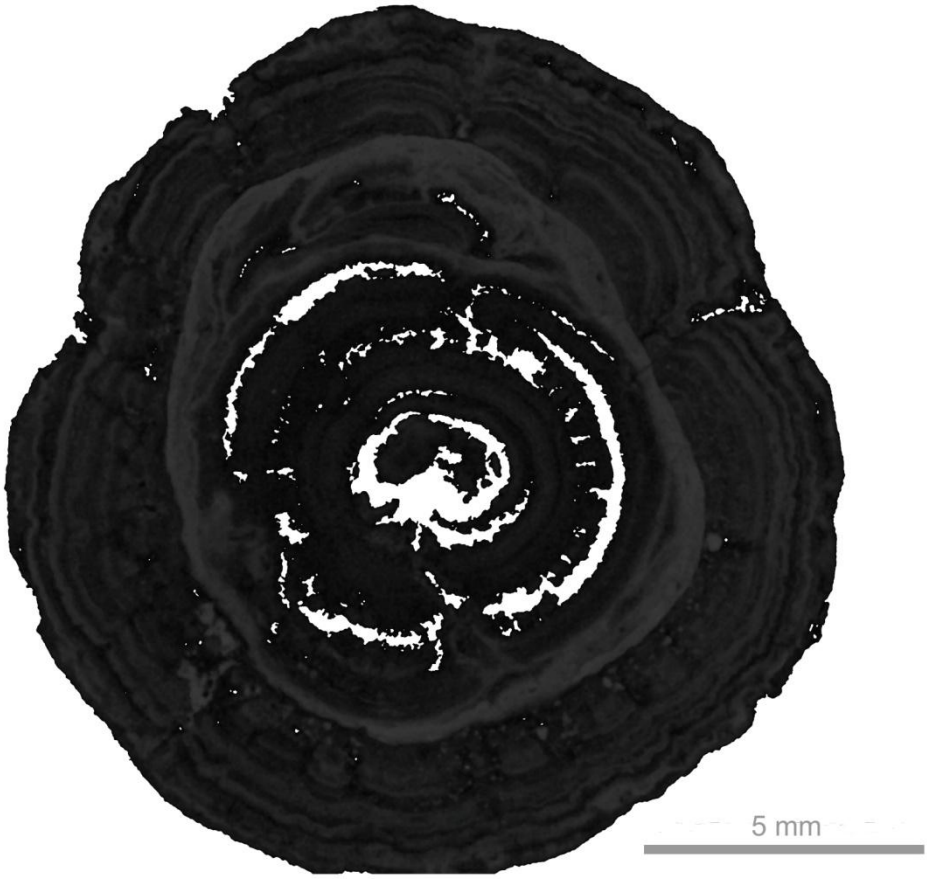

Figure 13. Grayscale slice of the bulk material of JWTomo3. Lighter grayscale values indicate denser material and *vice versa*. White areas represent pore space.

Generally speaking, the cavities are aligned concentrically within the boundaries of the

thick and dense layer. In the outermost parts, however, the cavities show irregular shape and can be aligned perpendicular towards the layers. In the outermost parts the layers are banded and rounded. In the upper-right-hand side of Figure 13 the layers seem to bend around the cavities. Again, relatively clear alternation of sparse and dense sub-layers occurs especially in the outermost parts of the nodule. In addition, smaller and denser aggregates can be observed.

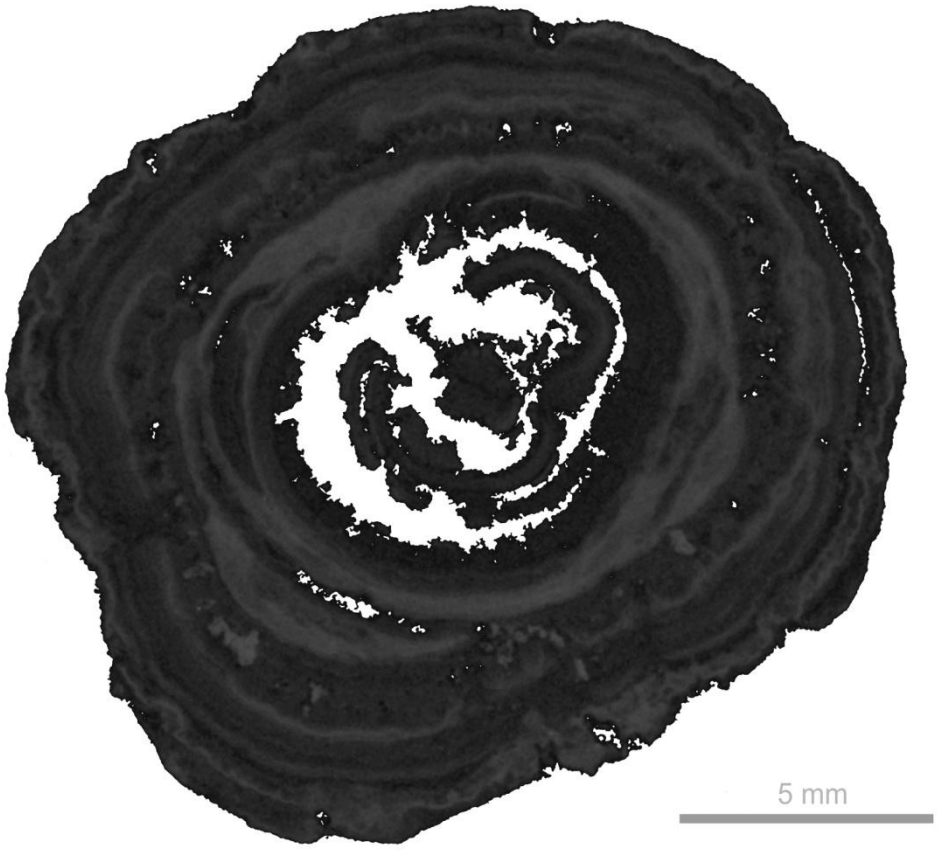

Figure 14. Grayscale slice of the bulk material of JWTomo3. Lighter grayscale values indicate denser material and *vice versa*. White areas represent pore space.

JWTomo6 is the smallest and the most spherule-like of all the sample spheroidal concretions (see Figure 4). The nodule's surface texture is granular or semi-granular. Much like the previous nodules, interior of JWTomo6 can be divided into two to three different sections. Interior is dominated by a pore network which is then surrounded by a thick and a rather uniform dense layer (Figure 14). Material towards the core from the dense layer is mainly homogeneous contrary to the material outside the thick layer. Hence, outermost layers of the concretion show distinguishable alternation between dense and sparse sub layers. Furthermore, in all of the samples the pore network seems to

stretch from the core to the surface.

4.2 Composition of the concretions

4.2.1 LOI

Weight changes at 105 °C and at LOI temperatures showed considerable shifting in mass compared to original measurements made at room temperature. Drying in the hot air oven already showed the porous nature of the concretions as the weight change was already ~40 % compared to wet weight. In the first step of LOI between temperatures 500 and 550 °C organic matter is combusted to ash and CO_2. The change was ~14 percent's calculated from dry weight using the equation (11):

$$LOI_{550} = ((DW_{105} - DW_{550})/DW_{105})*100 \qquad (11)$$

where LOI_{550} represents the amount of loss on ignition at 550 °C (as a percentage), DW_{105} the dry weight after being kept in hot air oven and DW_{550} the dry weight after igniting the sample. In the next step at 1000 °C carbon dioxide is generated from carbonates. The LOI is calculated as (12):

$$LOI_{1000} = ((DW_{550} - DW_{1000})/DW_{105})*100 \qquad (12)$$

where LOI_{1000} is the amount of LOI at 1000 °C (as a percentage), DW_{550} is the dry weight after igniting in 550 °C and DW_{1000} represents the dry weight after heating the sample to 1000 °C and finally DW_{105} is the sample's weight after dried in hot air oven. The results of mass changes in samples JWXRF1 and JWXRF2 are showed in Table 2.

Table 2. The weights of samples JWXRF1 and JWXRF2 while being: 1) wet, 2) at room temperature (RT), 3) at 105 °C, 4) amount used in LOI (m_{LOI}), 5) dry weight after igniting at 550 °C and 6) at 1000 °C. Finally the % of LOI has been calculated using equations (11) and (12).

		JWXRF1	JWXRF2
m_{wet}	g	2.833	2.391
m_{RT}	g	1.797	1.597
m_{105}	g	1.589	1.414
m_{LOI}	g	0.728	0.573
m_{550}	g	0.623	0.488
m_{1000}	g	0.589	0.467
LOI_{550}	%	14.4	14.8
LOI_{1000}	%	4.7	2.1

4.2.2 XRF

The X-Ray Fluorescence analysis revealed that the samples are composed mainly of iron and manganese, with quite large amounts of SiO_2, P_2O_5 and Al_2O_3.

Table 3. The chemical composition of the samples JWXRF1 and JWXRF2 measured with WD-XRF quantitative analysis compared to USGS Mn-nodule standard.

		JWXRF1		JWXRF2		USGS NOD-P-1
SiO2	%	21.26		24.08		13.9
TiO2	%	0.23		0.28		0.5
Al2O3	%	4.81		5.66		4.8
Fe2O3	%	27.41		37.34		15.8
MnO	%	16.82		19.23		37.6
MgO	%	1.63		2.021		3.3
CaO	%	1.97		2.38		3.1
Na2O	%	1.17		1.38		2,2
K2O	%	1.58		1.82		1,2
P2O5	%	4.01		5.78		0,46
Ba	ppm	3043		2413		3350
Ce	ppm	144		109		290
Co	ppm	410		271		2240
Cr	ppm	13	<MDL-10	10	<MDL-10	-
Cu	ppm	136		85		11500
Ga	ppm	9	<MDL-2	11	<MDL-2	-
La	ppm	65		64		104
Nb	ppm	8	<MDL-10	7	<MDL-10	120
Ni	ppm	233		124		13400
Rb	ppm	63	<MDL-10	64	<MDL-10	-
Sr	ppm	939		821		680
U	ppm	12	<MDL-10	10	<MDL-2	-
V	ppm	136		109		570
Y	ppm	50		42		-
Zn	ppm	516		244		1600
Zr	ppm	179		129		-
Total	%	80.9		100		82,83
Original	%	97.17		83,61		

JWXRF1 is normalized to 80.9 percent as LOI has been made, whereas JWXRF2 results are normalized to one hundred percent as LOI assay has not been made

<MDL-2 = Content is smaller than the method detection limit calculated with two standard deviations thus the result is below the detection limit

<MDL-10 = Content is smaller than the method detection limit calculated with ten standard deviations thus the result is below the detection limit

The samples also hold high concentrations of trace elements including strontium, barium, cobalt, cerium, nickel, yttrium, lanthanum and zinc (Table 3).

4.2.3 EPMA

The sample comprises largely of compounds of iron, manganese and phosphorus with minor amounts of potassium and sodium. These iron and manganese precipitates have inclusions of primary minerals like quartz, feldspars and hydrous micas (Figures 15 and 19 and Appendix D).

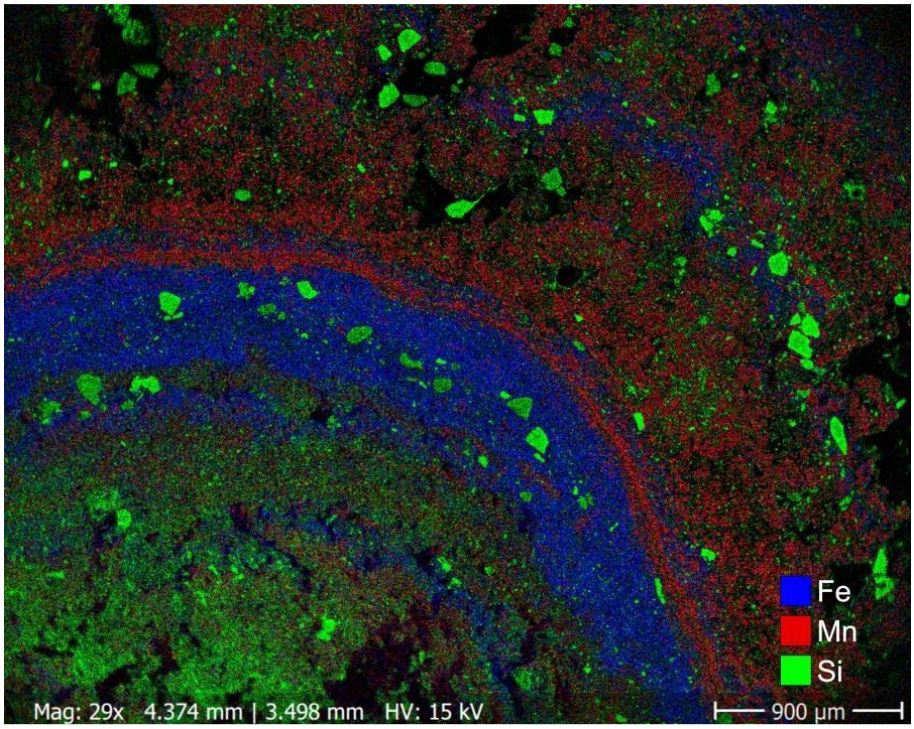

Figure 15. Caption of element mapping made with EDS. Core can be seen in the lower-left-hand side of the image with iron- (blue) and manganese-rich (red) layers surrounding the core as distinct concentric rings. Silicon is presented with green.

Element map of the sample was rendered and it shows mostly clear alternating manganese-rich and iron-rich layers (Figure 16). The Mn-rich layers seem to be more diffuse and Fe-rich layers more coherent albeit being thinner than the Mn layers. As stated previously, phosphorus is found on Fe-rich layers (Figure 17). More images are presented in Appendix C.

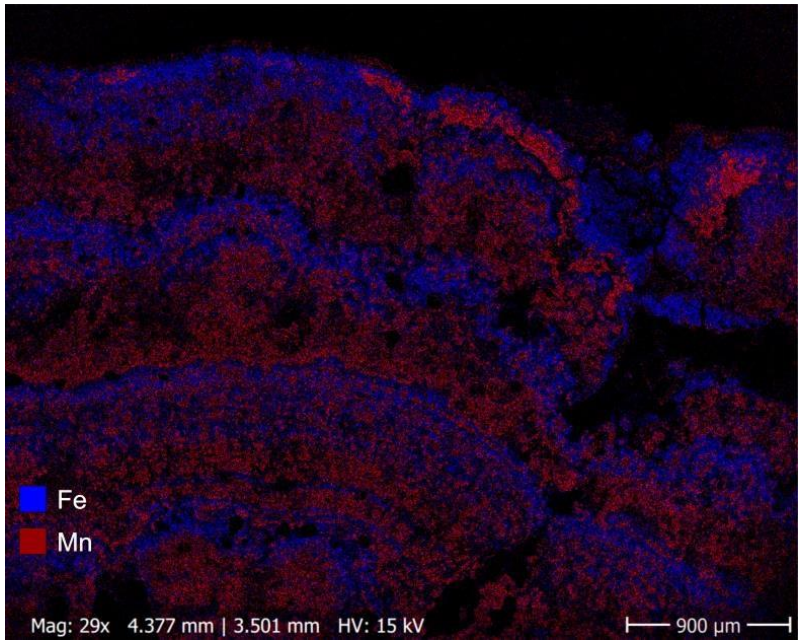

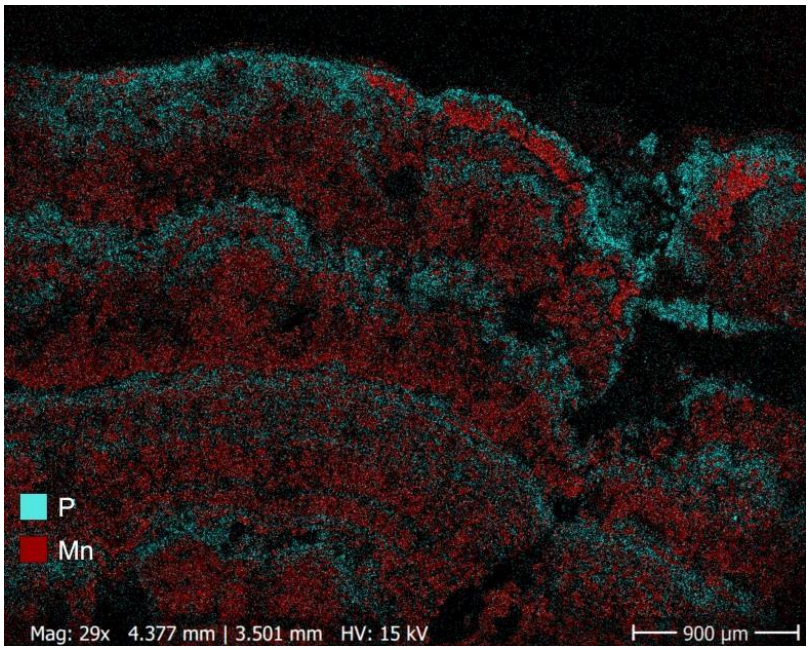

Figures 16 (upper) and **17** show repeating iron- and manganese-rich layers and phosphorus in the same layers as iron.

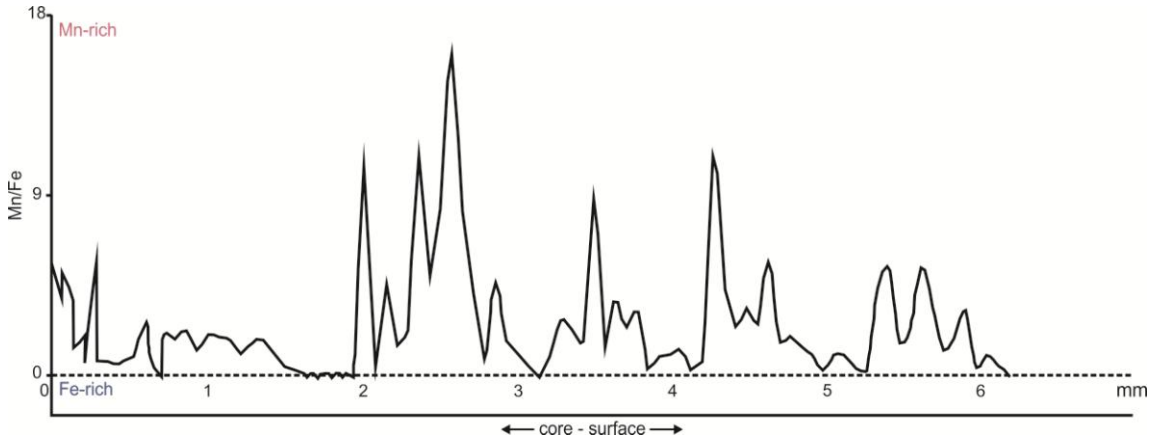

Figure 18. Diagram of JWEPMA Mn/Fe ratio from the core to the surface. The diagram shows alternating Mn- and Fe-rich layers. The thick Fe-rich layer can be seen at ~1.6 to 2 mm from the core. Iron is more enriched in the surface whereas manganese seems to be more enriched in between the core and the surface.

EDS line scan showed the same alternating Fe- and Mn-rich layer pattern. The profile (Figure 18) shows the thick Fe-rich layer and indicates that the most Mn-rich layers are gathered in between the thick Fe-layer and surface which is also Fe-rich. Data for EDS line scan can be found from Appendix F.

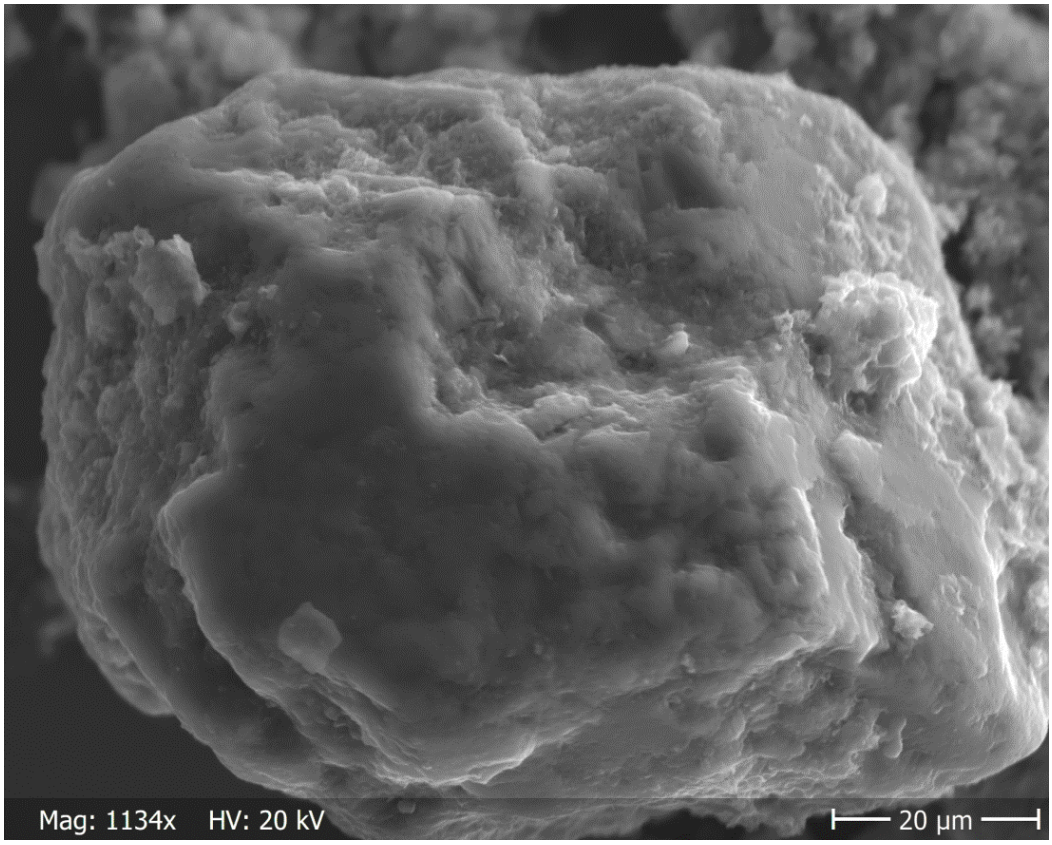

Figure 19. Secondary electron image of potassium feldspar (likely albite).

The EDS analysis showed that only the silicon rich minerals have distinct chemical compositions and sharp-edged crystal morphology that can be correlated for instance to biotite (Appendix D), potassium feldspar (Figure 19) and quartz. All the iron and manganese rich layers had mixed compositions of iron oxides with phosphorus, aluminum, silicon, magnesium, sodium, calcium and potassium and manganese oxides with aluminum, silicon, magnesium, sodium, calcium, potassium and chlorine. The core was the most enriched in silicates whereas the rim of the concretion showed mostly iron, manganese and phosphorus compounds. Also some of the interstitial spaces between iron and manganese oxides had almost pure carbonaceous composition.

4.3 Dissolution experiment

The dissolution experiment showed that the concretions are susceptible to anoxic environment. Both of the samples JWTomo3 and JWTomo5 had lost material which had reprecipitated on the bottom and walls of the sample bottles (Figure 7). As rescanning with CT showed, the volume and area of both the concretions and their pore networks changed during the experiment (Table 1). However, visual observations of the samples in Avizo Fire and VG Studio did not show any remarkable changes in layer or pore network structure (Figures 20 and 21).

Table 4. Composition of JWTomo3 and JWTomo5 dissolution experiment fluids

		JWTomo3	JWTomo5
Mn	%	0.007	0.025
Fe	%	0.025	0.283
P	%	0.205	0.268
Na	%	0.089	0.079
Mg	%	0.027	0.031
Si	%	0.008	0.016
S	%	0.012	0.251
Cl	%	1.028	1.149
K	%	0.048	0.050
Ca	%	0.254	0.269
Ni	%	0.021	0.024
Cu	%	0.011	0.010

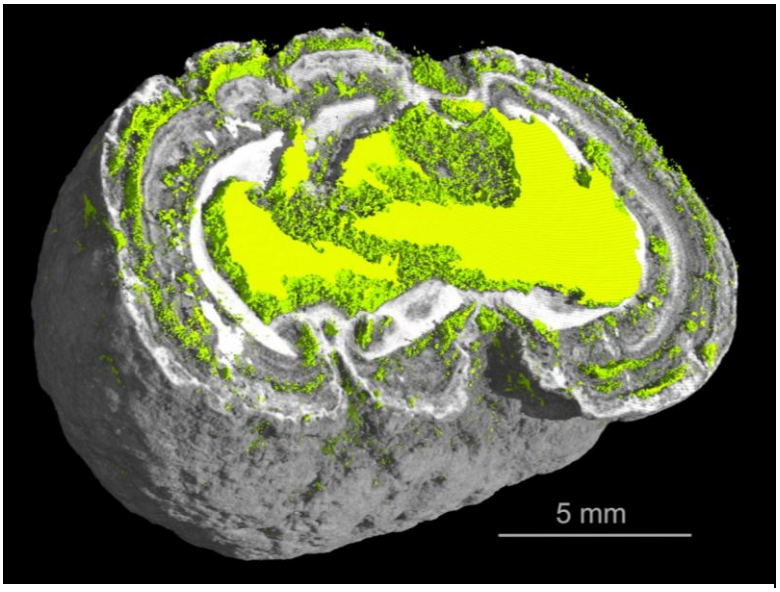

Figure 20. Representation of JWTomo3 before the treatment in anoxic environment. Yellowish green presents pore space.

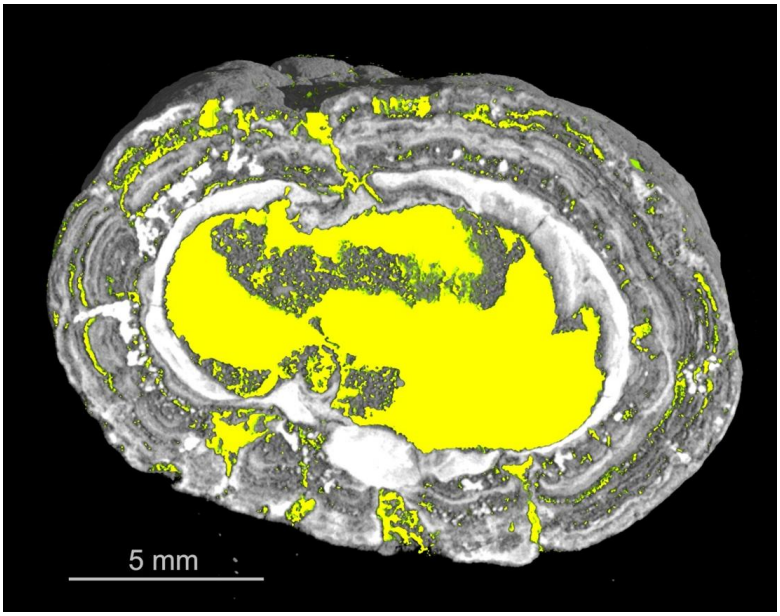

Figure 21. Reconstruction of JWTomo3 after treatment in anoxic environment. Yellowish green presents pore space.

XRF analysis also showed that there are some minor amounts of elements released to the water (Table 4). Main difference between sample bottles was the colour of the precipitates accumulated in the bottles. JWTomo3 showed a layered structure, where the top parts were dominated by yellowish brown precipitates and lower parts by dark gray

precipitates. On the other hand, JWTomo5 was composed completely of the latter dark precipitates. EDS spot analysis showed that the yellowish precipitates are Fe oxides whereas the dark precipitates are Fe sulphides. Some rod-like microbes were also observed in the Fe oxides (Figure 30). The pH was within or near circumneutral, as the pH paper indicated it to be ~6 to 6.5 in JWTomo3 water and ~8 in JWTomo5 water. Also a distinct rotten egg-like smell was observed during opening of both the sample bottles, indicating the presence of H_2S.

5. DISCUSSION

5.1 Growth and evolution of spheroidal ferromanganese concretions

5.1.1 Composition and the role of phosphorus

The sample concretions were collected near Haapasaari, north eastern parts of the Gulf of Finland. They show compositional similarities to other Baltic Sea concretions (e.g. Anufriev and Boltenkov 2007, Hlawatch et al. 2002) and deep sea nodules (Wang et al. 2009a) analyzed previously. As Table 5 indicates, however, the amount of Mn is smaller than average within the Gulf of Finland although the amounts of Fe are similar. Instead the Fe/Mn ratio is more alike with the concretions from the Bay of Kiel. Also phosphorus shows similar concentrations as in the samples from the Bay of Kiel. In addition, silica concentrations are higher than in earlier analyses. River Neva discharging from the east of the Gulf affects greatly the hydrodynamics of the area as well as with the amounts of components available for the growth of the concretions. On the other hand, the Baltic Proper dominates in the west (Pitkänen et al. 2008). Some investigators consider the Gulf of Finland as an estuary of River Neva, which creates a transition zone from marine to freshwater environment (Pitkänen et al. 2008, Telesh et al. 2008). Albeit being only two samples compared to an average of many, it is possible that the lower Mn/Fe ratio could be related to distance to rivermouths such as River Neva, as suggested earlier by Glasby and associates (1997). However, it is more probable that the chemical composition of the samples is more closely governed by geochemical processes and characteristics of the sampling location.

Table 5. Bulk chemical constituents of ferromanganese concretions.

	JWXRF1[+] wt-%	JWXRF2[+] wt-%	USGS NOD-P-1[+] wt-%	GoF* wt-%	WBS** wt-%	BoK[†] wt-%	EPO[F] wt-%
Mn	13.03	14.89	29.12	32.0	23.8∓12.8	18.10	16.40
Fe	9.59	13.06	5.53	9.15	14.7∓12.8	14.50	4.25
Si	9.94	11.26	6.50	5.14	n.a.	n.a.	2.14
Al	1.27	1.50	1.27	2.70	0.7∓0.3	1.02	n.a.
Na	0.44	0.51	0.82	0.56	n.a.	n.a.	n.a.
Mg	0.99	1.22	1.99	1.28	1.41∓0.4	1.25	n.a.
Ti	0.14	0.17	0.30	0.11	n.a.	n.a.	0.23
K	0.65	0.76	0.50	0.81	n.a.	0.87	n.a.
P	0.88	1.26	0.10	n.a.	n.a.	1.48	n.a.

+ Quantitative analysis made with WD-XRF
*Chemistry of spheroidal concretions from the Gulf of Finland analyzed with ICP-MS (Anufriev and Boltenkov 2007)
** Median chemistry of spheroidal concretions from the area of western Baltic Sea analyzed with ICP-MS (Hlawatsch et al. 2002)
† Chemistry of spheroidal concretions from the Bay of Kiel analyzed with ICP-MS (Hlawatsch et al. 2002)
F Chemistry of ferromanganese nodules from Clarion-Clipperton zone of Eastern Pacific Ocean (Wang et al. 2009a)

Lehtoranta (2003) calculated that the topmost sediment column has a phosphorus concentration of 3.2 mg g^{-1}. Earlier calculations of the amount of P in spheroidal ferromanganese concretions of the Gulf is 34.0 mg g^{-1} (Zhamoida et al. 2004) and between 0.7–26.0 mg g^{-1} (Ojala 2008). Based on the data calculated here, the concentrations of P in JWXRF1 and JWXRF2 are 8.80 mg g^{-1} and 12.60 mg g^{-1}, respectively. This agrees with previous data and suggests that the concretions work as a much more effective trap for phosphorus as the surrounding sediment. Therefore their dissolution might lead to increased phosphate concentrations in the sediment pore water where concretions are dissolving. This is discussed further in section 5.1.5.

5.1.2 Structure and related composition

Spheroidal ferromanganese concretions show granular texture and are found in different sizes and shapes. Commonly they are around 2-30 mm in diameter (Zhamoida 2004). They also display irregular internal features. Indeed, the 3D reconstructions of the samples show ornamental patterns and distinctive lamellar structures. This alternation of layers of differing densities is manifested as concentric rings, banded layers or laminae

(Figure 5.1). Previous studies have also identified these less dense and dense sub-layers within the concretions (e.g. Glasby et al. 1997 and references therein, Zhamoida 2004, Marcus et al. 2004). Such ripple mark-like structures have been attributed to disequilibria between Mn^{2+}/Mn^{4+} and Fe^{2+}/Fe^{3+} (Halbach et al. 1988), although they do not explain the ornamental apprearance of the layers (Wang et al. 2011). As previously mentioned, manganese is well capable of oxidizing reduced iron albeit a slowing reaction with rising pH (Postma 1985). In addition to Fe (oxyhydr)oxides, the inorganic oxidation reactions of Mn minerals can be catalyzed by other Mn phases or microbial surfaces (e.g. Chukhrov et al. 1976, Ehrlich 2002). Previous chemical analyses with EDS revealed that the concentric layers are mostly heterogeneous even within an individual micro-layer: only the ratio between iron and manganese alternates. In addition, there is no regular alternation between iron-rich and manganese-rich layers. Investigations done here, and the study of Ojala (2008) also supports these findings as can be noticed from Figure 18. However, as these figures show, some division based on both structure and composition can be made. The most distinct features are 1) the core 2) thick Fe-rich layer and 3) the surrounding concentric-like layers.

Unlike other oceanic nodules (Somayajulu 2000), the effect of bioturbation and the mechanical movement on the structural characteristics of the concretions is liable to be tangential (e.g. Marcus et al. 2004, Zhamoida et al. 2007). This is because especially in the Gulf of Finland benthic macrofauna has suffered from the halocline and its effect to the generation of hypoxia or anoxia (Pitkänen et al. 2008). Also the eutrophication of surface waters has increased biomass production thus leading to oxygen consumption in deep waters.

5.1.1 Biomineralization

Recent studies suggest a possible involvement of biomineralization on the formation of oceanic ferromanganese nodules (Wang et al. 2011). Microbial communities are able to form laminae of mineralized material as a byproduct of their metabolism (Vasconcelos and McKenzie 2009). Although major part of the mineralized material seems to be amorphous or poorly crystallized, some phases like birnessite and manganosite have been identified using X-Ray diffraction. In the study of Zhang et al. (2002) these black coarse

precipitates have coated the surface of capsular material which consists of entombed nannobacteria. Thermodynamically unstable manganosite (MnO) occurring only as isolated grains in the filamental structures within the concretions has also been observed (Zhang et al. 2002). This is in concert with the presence of biofilms (Edwards et al. 2005) and Mn and Fe reducing and oxidizing microbes (Yli-Hemminki et al. 2014) observed in ferromanganese nodules. Lamellar structures observed in the Baltic Sea nodules thus might have genetic similarities to layers seen in other sedimentary environments or oceanic nodules.

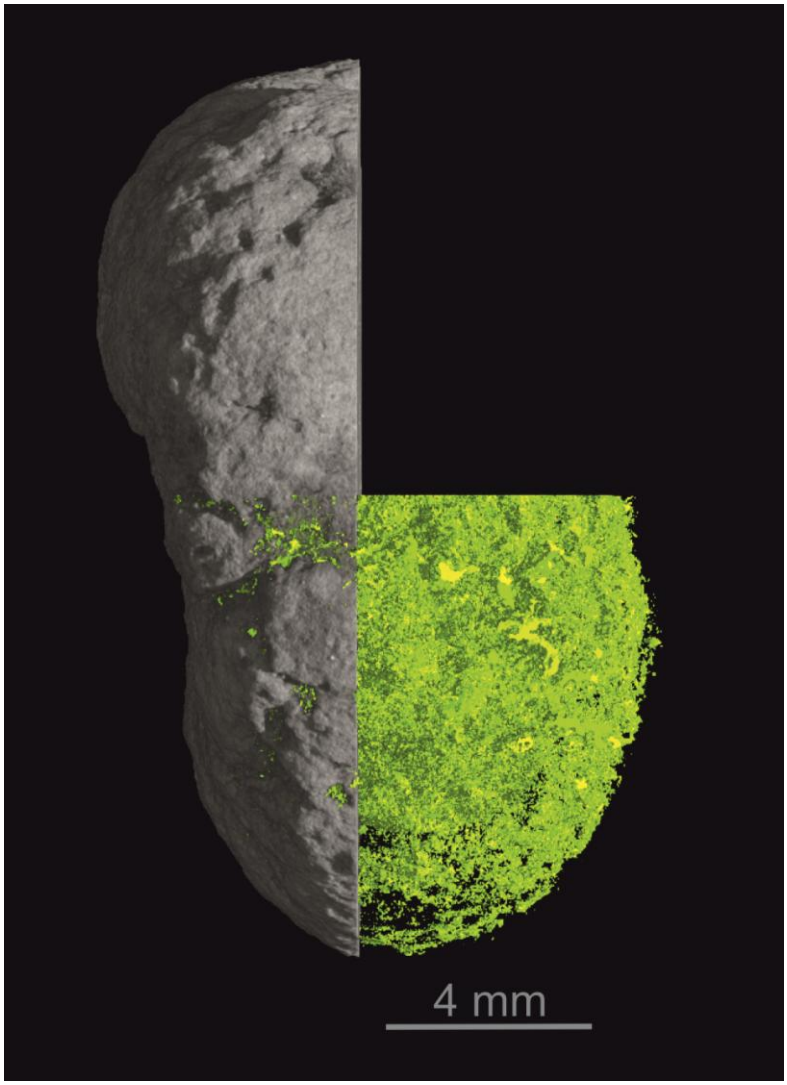

Figure 22. 3D representation of JWTomo3 and a part of its pore network (green). The image shows that the pore network is extensive.

Tomography images also show an extensive network of cavities ranging from the interiors of the concretions to the surface (Figures 9 and 22). It has been suggested that

these cavities might work as attachment surfaces for microbes. Microbes need a close or even direct contact to the concretions' surface with their cell wall (Thullner et al. 2005) in order to form a suitable environment to reduce or oxidize for instance manganese (Bargar et al. 2005). Continuing this way of thinking, also the pore network and cavities are mainly concentrated to the Mn-rich layers and are far more extensive than the surface area of the nodules.

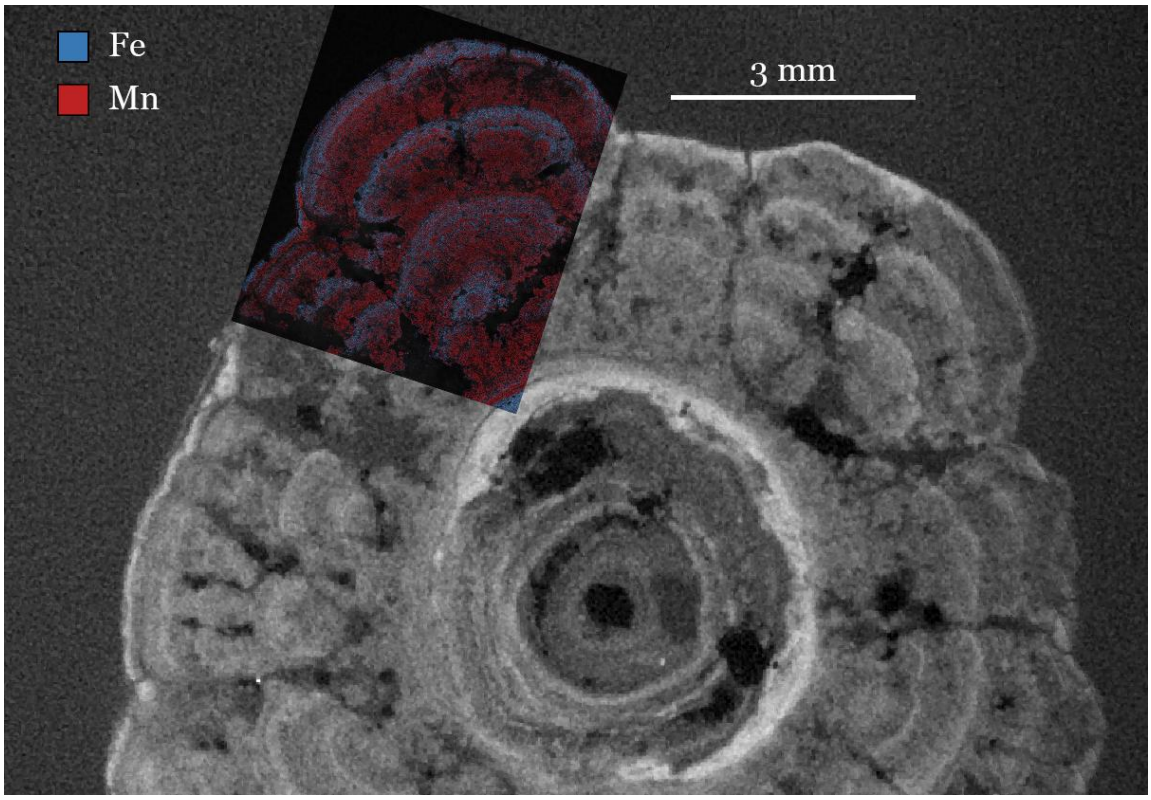

Figure 23. Composite image of JWEPMA with EDS element mapping image showing the main constituents (Fe and Mn) of the dense (white) and less dense (gray) layers present in the CT grayscale slice of the sample.

In addition, the interstitial spaces in the manganese rich areas are occasionally dominated by almost purely carbonaceous composition (see Appendix D). It has been previously suggested that high C/Mn ratio is related to biogenic processes (Wang et al. 2011). However, manganese is more readily reduced than iron, hence the less dense layers could also possibly imply susceptibility to reductive environments, microbes only reducing the manganese. In addition, due to the extremely porous nature of the nodules, it is possible that at least part of the carbon containing areas could be explained by the intrusion of epoxy to interior cavities of the nodules during sample preparation thus the results should

be interpreted with caution. Nevertheless, up to 14.8 % of the dry weight comes from organic compounds as indicated by loss on ignition at 550 °C (see Table 2). The concretions studied, however, had only relatively small amounts of carbonate carbon (~2 to 5 %). As it is unlikely that C_{org} has been able to withstand decomposition over a period of $>10^3$ years of concretion growth, it could be possible that the C_{org} is novel, formed by either microbes or by adsorbed organic matter to Fe (Gu et al. 1994) and to some extent Mn (oxyhydr)oxides.

Biogenic origin of the concretions is also supported by the findings of Wang and associates (2009a), who showed that Mn-rich layers of deep ocean nodules host microbes whereas Fe-rich layers are almost devoid of them. However, in laboratory investigations Mn oxidizers including *Bacillus* and *Pseudomonas* thrived also in Fe rich environments (Yli-Hemminki et al. 2014). Accompanied with EDS element mapping, it can be showed that Fe-rich layers form the more dense areas whereas Mn-rich layers form the less dense areas observable in the tomography images (Figure 23). Chemolithoautotrophic microbes are able to use Mn^{2+} as a substrate for energy generation while producing oxidized manganese (Edwards et al. 2005). This could attest to Mn susceptibility to microbial oxidation. As mentioned earlier, Fe biomineralization is also ubiquitous in several natural environments (e.g. Ghiorse 1984, Glasauer et al. 2001).

However, as Mn is more readily formed by microbial oxidation, Fe (oxyhydr)oxide formation could be only indirectly affected by biofilms or the accumulation of iron to the cell walls of bacteria or could entirely be controlled by abiogenic processes. Instead, inorganic precipitation of iron via oxidation by manganese would predominate. However, as stated previously, reduction of $Mn^{3+/4+}$ by Fe^{2+} gets hampered with increasing pH (Postma 1985) thus invoking a question whether biomineralization would be the driving force for ferromanganese concretion growth after all. When iron enters a system with circumneutral pH and oxygen, ferric iron compounds are spontaneously formed on available nucleation sites (Konhauser and Riding 2012). Once again, bacteria provide such nucleation sites. Therefore, some prerequisites for possible role of microbes in the growth and evolution of the concretions may be filled: 1) presence and the extensive nature of pore network and concretion surface which are able to accommodate the microbes; 2) presence of biofilms and microbes in the concretions (e.g. Yli-Hemminki et al. 2014, Wang et al. 2011 and with caution this study); 3) Localization of C to Mn-rich

layers and more diffuse structure of the Mn-rich layers and 4) the presence of rod-like microbes within Fe (oxyhydr)oxide precipitates collected from the dissolution experiment.

5.1.3 Core formation and nucleation

Recent studies have identified micronodules of ferromanganese (oxyhydr)oxides accumulating on the deep oceanic nodules (Wang et al. 2009b). Similar micronodule-like manganese structures have also been observed in laboratory experiments (Hosseinkhani and Emtiazi 2011) and as a biofouling agent in heat exchanger surfaces (Kuosmanen et al. 2005). Although not as well distinguishable as with HR-SEM or HR-EDS, grain aggregates alike that are roughly 10 to 200 μm in diameter can be seen in the CT images

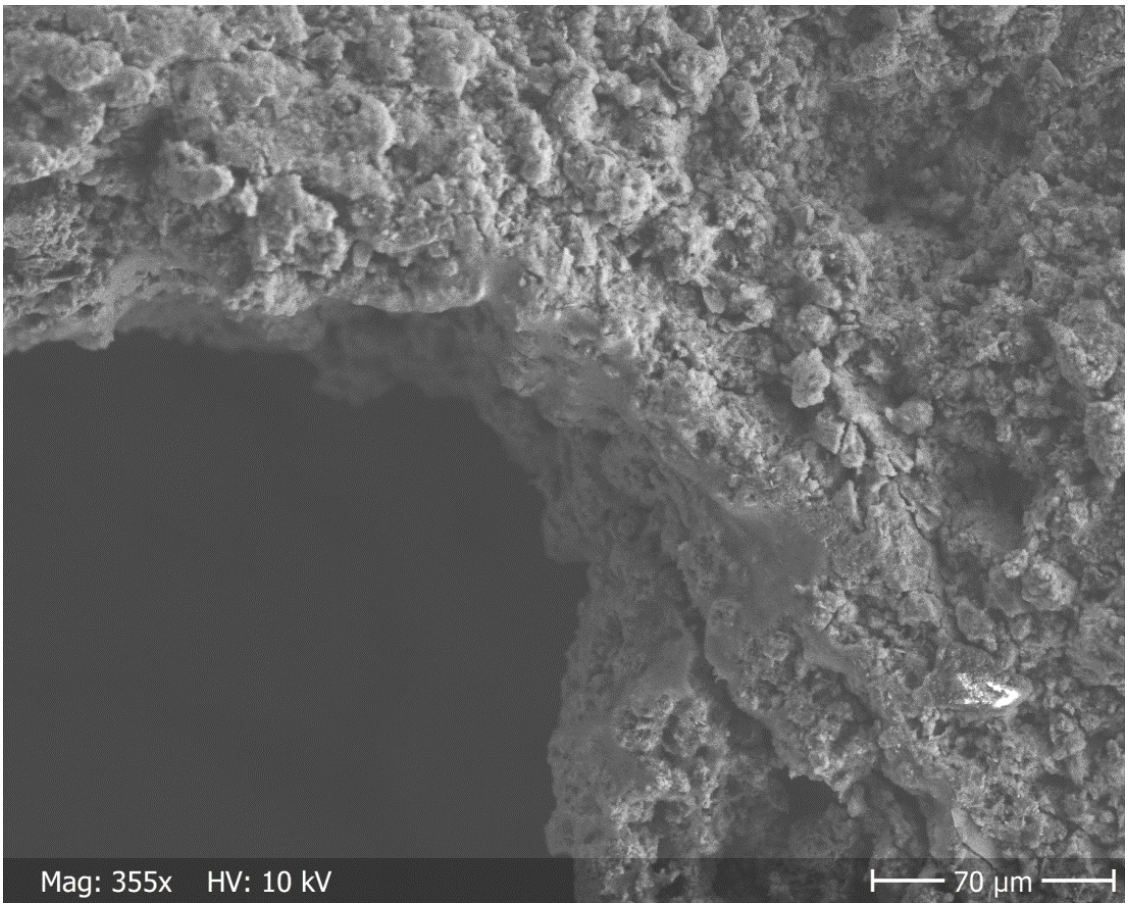

Figure 24. Secondary electron image from the core area of JWEPMA. The sample is composed of aggregates with an average diameter of ~20 μm.

of the sample concretions as well (Figures 24, 25, and 26). These grain aggregates are mainly clotted on the more structurally homogeneous interior of the concretions and to

interstitial spaces between denser layers, i.e. to the Mn-rich layers. In addition, interpreted from the EDS element mapping images, the core of the sample seems to be chemically the most heterogeneous part of the sample. This is in concert with the results gained from CT scanning which shows structural homogeneity. In essence, iron, phosphorus, manganese and major amounts of silicate minerals are distributed into the core. This could suggest that hydrous micas, feldspars and quartz have acted as nucleation sites for the precipitation of both iron and manganese oxides. This has also been suggested previously (Zhamoida et al. 2007).

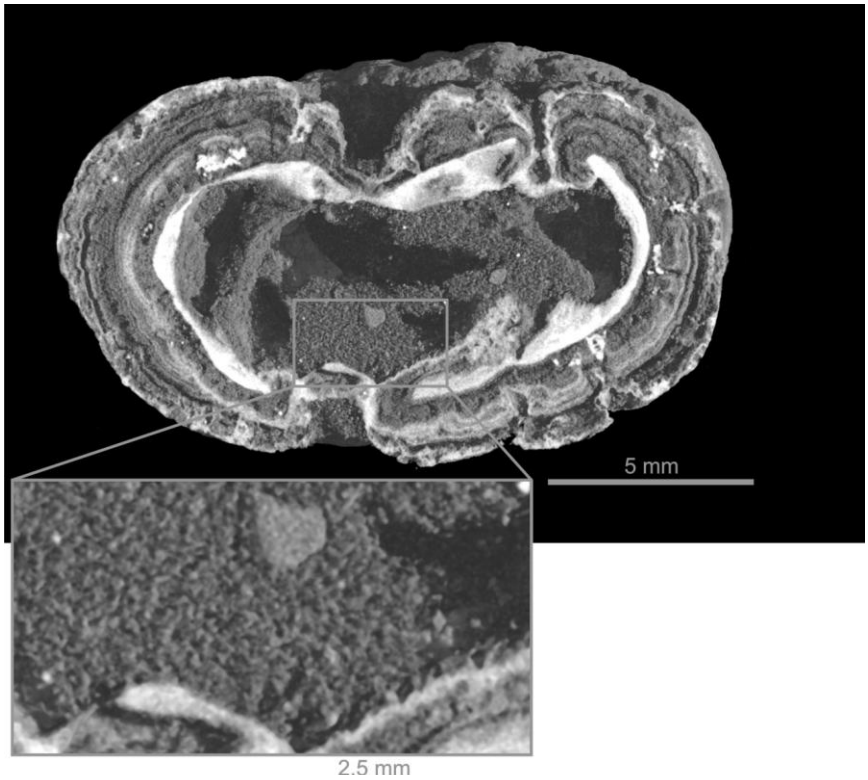

Figure 25. 3D Reconstruction of JWTomo3. Layers of differing density can be observed: in the sample less dense layers seem to predominate. The interiors of the concretion show aggregate- or micronodule-like texture in which grains of detrital origin are embedded. Individual aggregates are roughly 10 to 200 μm in diameter.

Both iron and manganese minerals are mainly formed in oxidative environment favoring circumneutral pH, and occur as colloidal, amorphous and/or poorly crystalline oxyhydroxide precipitates (e.g. Wang et al. 2011, Kendall et al. 2012). Also the bottom sediments hosting ferromanganese concretions in the Gulf are oxidized and the pH of the water column is on average ~8.0 to 8.4 (Perttilä et al. 1980). These colloidal compounds have reversed surface charges, Mn having negative and Fe having positive charge.

Opposite charges influence the formation of mingled colloids (Bau et al. 1996) and later coarser agglomerates in a process which is then able to incorporate trace metals as well (Koschinsky and Halbach 1995). Other metals are mainly incorporated by ionic bonds and scavenging. This could explicate both the distribution of chemical components in the core and the more homogeneous composition of the core area of the nodules seen in the tomography images. In general, however, the net charges of colloidal Fe and Mn oxyhydroxide particles get neutralized upon the delivery to the ocean basin because of high ionic strength of the seawater (Gustafsson et al. 2000, Krachler et al. 2010). Usually Mn (oxyhydr)oxides are also stabilized in seawater through binding into other transition elements (Glasby 1974). Moreover, no concentric growth layers around detrital minerals is observed thus suggesting rather an abduction of the grains during concretion growth. Also reaggregation on the nucleation sites, whether they were detrital minerals or microbial biofilms and cell surfaces, would also require charging of the particle surfaces to enable formation of intermingled colloids as the "root" for further concretion growth. This would follow the train of thought of Wang and associates (2011) of marine nodule growth and evolution. First bacterial biofilms form around detrital minerals acting as seeds for metal attachment to their surfaces (Konhauser and Riding 2012). The existing mineral precipitates then work as templates for further mineral precipitation. When the precipitates reach large enough size, they clot together forming a self sustaining microcosm which then continues to grow if enough components are available and e.g. pH and Eh are suitable for mineral precipitation. This colloidal intermixing could also create the wavy- or ornamental-like appearance of the alternating Mn- and Fe-rich layers.

5.1.4 The outer layers

The outer layers of the concretions are composed of structurally sparse and less-dense Mn-rich layers occasionally interfered by denser and more coherent Fe-rich layers as can be seen in Figures 25 and 26. After the initial accretion of the nucleus, Fe and Mn accumulate on existing seed crystals in deep oceanic nodules (Wang et al. 2011). It is possible, that the colloid forming process continues outwards of the core area in the Baltic Sea ferromanganese concretions as well. Some microbe-like structures were also observed during EPMA analyses from the Mn-rich layers (Figure 27). This could suggest a direct biogenic origin for Mn layers and abiogenic (indirect microbial) origin for Fe layers.

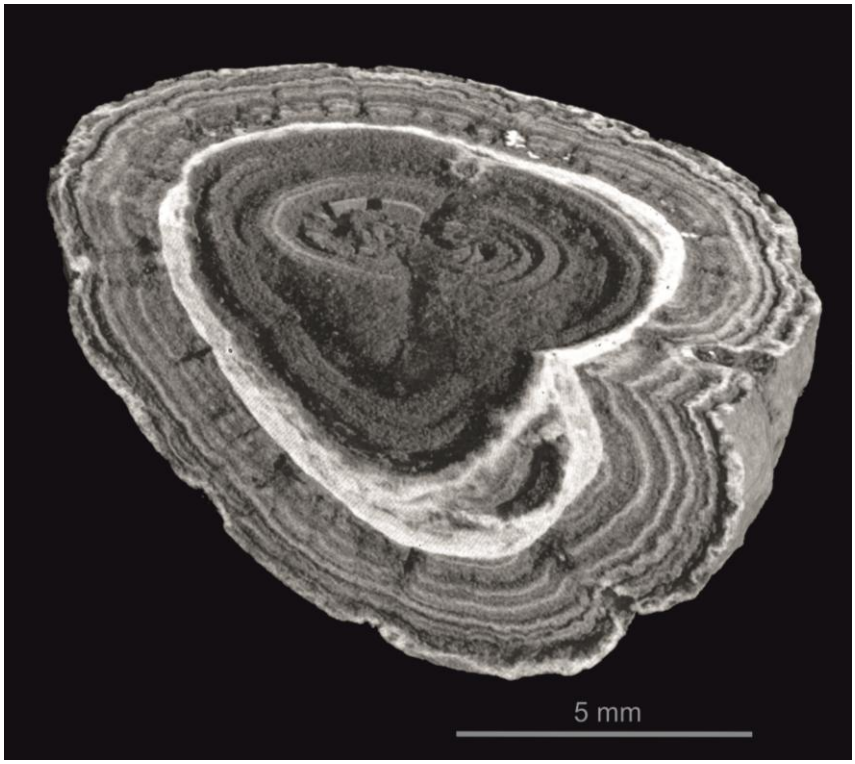

Figure 26. 3D representation of JWTomo5.Mn-rich and less dense clotted aggregate structure predominates (gray) which is occasionally punctuated by denser Fe-rich layers (white). Black areas within the concretion are pore space.

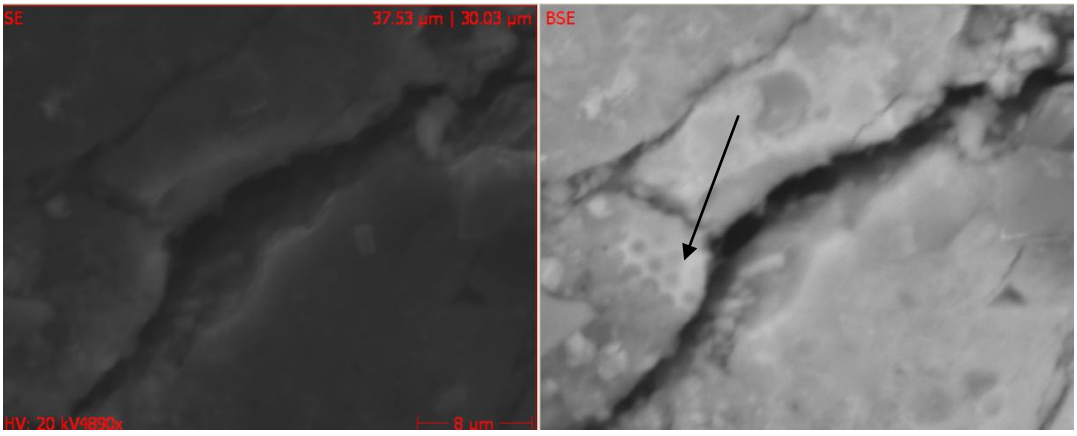

Figure 27. SE and BSE images from Mn-rich layer of JWEPMA. The arrow points to a hexagon shaped form which may be a possible chain of *cocci* or remnants of a biofilm with a total length of 8 to 10 µm.

5.1.5 Concretion dissolution

Dissolution experiment showed that material is effectively removed from the concretions and part of it is retained in the solution while major part of it has reprecipitated in the walls and the bottom of the sample bottles as yellowish brown (Figures 7 and 28) and dark gray precipitates (Figures 7 and 29). Furthermore, CT scanning suggests that the

volume of JWTomo3 has slightly decreased whereas the volume of JWTomo5 has slightly increased (see Table 1). Also the pore network area and volume has increased within JWTomo3 but in JWTomo5 it has decreased. These data suggest dissolution and precipitation of material to JWTomo5 concretion and dissolution of JWTomo3 concretion during the experiment.

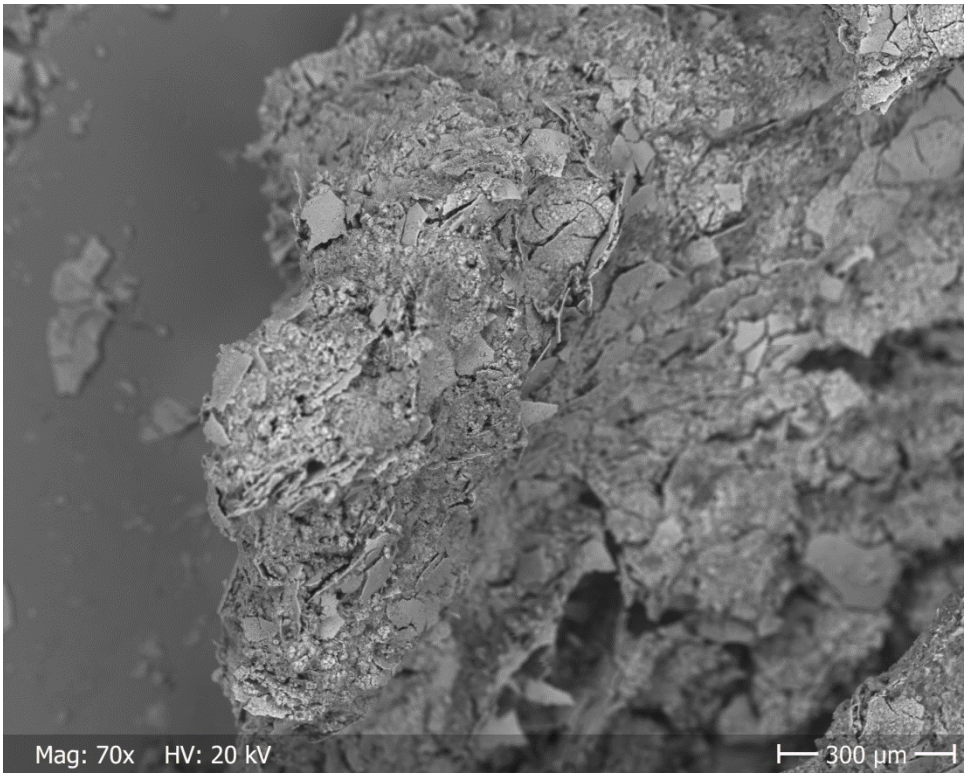

Figure 28. BSE image of flaky Fe (oxyhydr)oxides collected from JWTomo3 bottle.

Dissolution of the ferromanganese concretions has risen a question whether they would act as a repollutant by releasing numerous compounds during dissolution (e.g. Zhamoida 2004). As mentioned earlier, in the area of the Gulf of Finland oxygen conditions are on their lowest during summer as a lot of organic matter has accumulated on the seafloor and in conjunction with the hydrodynamic conditions they change the surface sediment processes to anaerobic (Pitkänen et al. 2008). In the bottom sediments brown layers indicate oxidative environment and the formation of Fe^{3+} (oxyhydr)oxides and thus the retention of phosphorus (Lehtoranta 2003). However, areas of dark gray precipitates are indicative of the formation of iron sulphides unable to adsorb P.

The chemical analyses of the sample solutions imply, that dissolution has mainly targeted the Fe-rich layers of the concretions as can be seen from Table 4. Also some manganese has been removed from the concretions: Mn concentration of JWTomo5 water is approximately 3.6 times greater than the concentration of JWTomo3 water based on XRF analyses of the fluids (Table 4). Similarly, concentration of Fe in JWTomo5 water is as much as 11.3 times greater than in JWTomo3 water indicating a more effective precipitation process within the JWTomo3 bottle. Also the concentration of S is higher in JWTomo5.

Table 6. Comparison of Fe/Mn and Fe/P ratios of solid concretion samples and the liquids of dissolution experiment.

	JWXRF1	JWXRF2	JWTomo3	JWTomo5
Fe/Mn	0.74	0.88	3.57	11.32
Fe/P	10.90	10.37	0.12	1.06

Ratios of the metals are distinctly higher measured from the dissolution experiment fluid (Table 6). Then again, Fe/P ratios of the solid samples are higher than those of the fluid. JWTomo3 shows a remarkably low Fe/P ratio whereas JWTomo5 shows a ratio >1. This could indicate retention of phosphorus to the formed Fe (oxyhydr)oxides in JWTomo3 bottle which is also supported by EDS spot analysis (see Appendix D). In JWTomo5 bottle, however, the formation of sulphides hampers the ability of Fe to capture P.

In addition, the amount of precipitates collected from JWTomo3 bottle was greater than the amount collected from JWTomo5. This also generates some inconsistency to the data. It is possible however, that the increased volume of JWTomo5 concretion is the result of microbial and/or abiotic oxidation of both iron and manganese. Because this material is amorphous and really diffuse, it leads to apparent growth of the nodule. However, as both of the sample bottles had clearly released a lot of material to the environment and also both Fe and Mn concentrations are larger in JWTomo5 water, it is more likely that some analytical error has occurred during JWTomo5 imaging with CT or during postprocessing of the images. Nevertheless, the CT results of JWTomo3 can be held reliable. Although SO_4^{2-} operates as a limiting reagent for microbial sulphate reduction and the subsequent formation of sulphides, the higher amounts of S would imply such never transpired in

JWTomo5 bottle even though S species cannot be separated with XRF analysis. The rotten egg-like smell observed would, however, imply the presence of H_2S in both bottles which indicates microbial sulphate reduction has occurred.

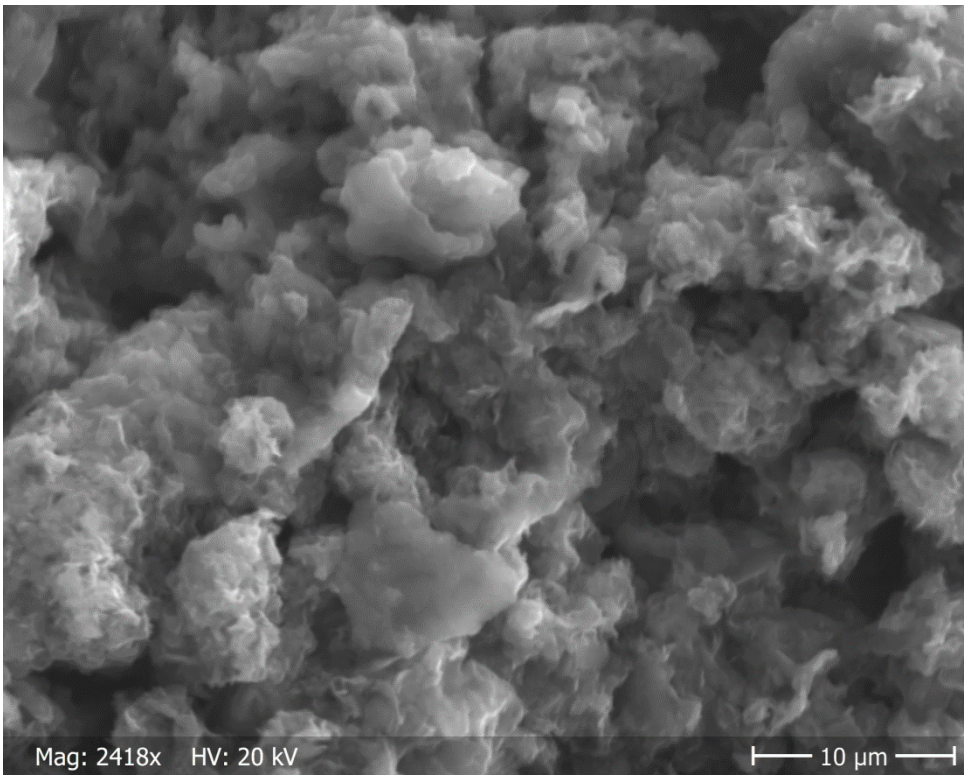

Figure 29. SE image of flaky iron sulphides collected from JWTomo5 dissolution experiment bottle.

Results here show that P release has occurred being 0.205 to 0.268 % of the solution (Table 4). As volume of the XRF samples was 20 mL, the concentrations JWTomo3 and JWTomo5 yielded are 2.05 mg P L^{-1} and 2.68 mg P L^{-1}, respectively. These amounts are small compared to the P in the concretions (Table 3). However, these values are substantial compared to the macronutrient concentrations of Helsinki-water (Appendix E, P concentration was 0 in the beginning). In addition, the metals measured from the solution were 0.25 mg Fe L^{-1} and 0.07 mg Mn L^{-1} from JWTomo3 and 2.83 mg Fe L^{-1} and 0.25 mg Mn L^{-1} from JWTomo5. These are higher than the composition of Helsinki-water. Although the pH values of the solutions were not measured accurately (i.e. with a pH meter) and show values near the low end of circumneutral pH in the case of JWTomo3, the results have similarities with recent studies (e.g. Lehtoranta et al. 2015).

Lehtoranta and associates suggest that the dissolution and release of metals and P is mainly controlled by available labile C that microbes can utilize. Because both of the samples here were nourished with C source (Na-acetate), such presumptions cannot be made nor even separate abiotic and biotic reduction as will be discussed below. It should be remembered, however, that ultimately the reduction processes are driven by microbial sulphate reduction and the main question of metal reduction revolves around biological reduction being direct or indirect.

Fe^{3+} (oxyhydr)oxides are major terminal electron acceptors in marine (Canfield et al. 1993) and estuarine environments (e.g. Hyacinthe et al. 2006). Ferric iron oxide reduction is mainly controlled by microbial (enzymatic) catalysis in non-sulphogenic sediments (Lovley 1991) but can also be abiotic (Ionescu et al. 2015). *Shewanella*, a heterotrophic Fe-reducer was enriched in cultures from Baltic Sea ferromanganese concretions (Yli-Hemminki et al. 2014). Previous studies have showed that amorphous ferric iron oxides are reduced more easily than crystalline ferric iron oxides (Munch and Ottow 1983). In addition, the role of microbial reduction of these oxides decreases: lepidocrocite > hematite > goethite. However, according to Bonneville and associates (2009) there exists numerous solubility products of Fe^{3+} (oxyhydr)oxides even for a single mineral. This is because of differences in mineral properties such as crystallinity, grain size and impurities, but also because the difficulty of experimental determination of the solubility products. Usually the abiotic reduction rate exceeds microbial reduction with the presence of Fe sulphides (Mortimer et al. 2011), sulphides (Yao and Millero 1996) and nitrite (Burdige 1993). This study cannot separate abiotic and biotic reduction from each other, but recent studies have shown that abiotic reduction has a major role in the overall reduction of iron (Ionescu et al. 2015). Also Mortimer and associates (2011) noted while comparing abiotic and biotic Fe reduction while Fe sulphides are present, that abiotic reduction has a considerable role. Thus we could infer that the reduction of iron (and manganese) is controlled by both abiotic and biotic processes ultimately driven by microbial sulphate reduction with the presence of existing Fe sulphides boosting the reduction rates. Electron flux enabling direct and indirect microbial reduction originates from the added carbon source Na-acetate.

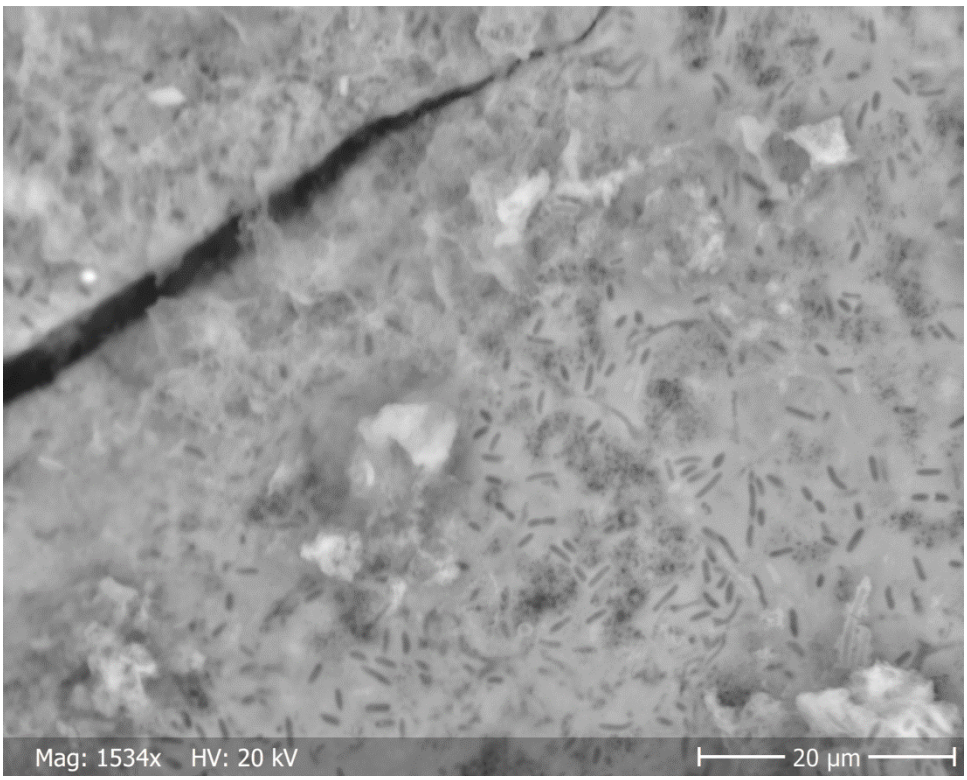

Figure 30. BSE image of JWTomo3 bottle Fe (oxyhydr)oxide flake with ~ 2 to 5 µm sized rod-like bacteria

Furthermore, EDS analysis showed that the yellowish brown precipitates are formed mainly of Fe and O thus implying they are Fe (oxyhydr)oxides (see Appendix D). The dark gray precipitates, on the other hand, showed spikes in S and Fe suggesting them to be Fe sulphides. The iron oxide precipitates also included some rod-like bacteria (Figure 30) which were not observed in the sulphides. It is suggested that four types of processes produce Fe (oxyhydr)oxides in circumneutral pH (Ionescu et al. 2015). These include chemical oxidation, Fe sorption to organic matter, microbial oxidation in aeorbic or microaerobic environment and microbial oxidation in anaerobic environment. Although the pH in JWTomo3 water was slightly under circumneutral it may have been similar to JWTomo5 water. It is possible that during concretion removal from the sample bottle, some amounts of oxygen entered the system leading to sulphide oxidation and subsequent precipitation of $Fe(OH)_3$. This can be presented by reaction (13) between FeS_2 and oxygen (Schieber 2011):

$$FeS_2 + 3.5O_2 + H_2O \rightarrow Fe^{2+} + 2SO_4^{2-} + 2H^+ \qquad (13)$$

This reaction thus produces acidity and reactive ferrous iron which may have decreased

the pH of JWTomo3 water. A further reaction with Fe^{2+} with oxygen then increases acidity and produces Fe hydroxides (14):

$$Fe^{2+} + 0.25O_2 + 2.5H_2O \rightarrow Fe(OH)_3 + 2H^+ \qquad (14)$$

Newborn Fe hydroxides tend to settle to the topmost parts of the sediment (Schieber 2011). Similar trend can be observed in the JWTomo3 bottle (Figure 7). However, the presence of rod-like microbes observed in the Fe (oxyhydr)oxide precipitates would attest to microbial intervention in their deposition. Some chemoheterotrophs such as *Leptothrix ochracea* facilitate ferro(manganese) mineral precipitation with their surface ligands as was discussed in section 2.1 (Konhauser and Riding 2012). Under aerobic conditions, microbes such as *Pseudomonas* or *Bacillus* able to oxidize Fe^{2+} have been cultured from the Baltic Sea ferromanganese concretions (Yli-Hemminki et al. 2014). These proteobacteria are rod shaped so they might have possible connection to the microbes observed in Figure 30. However, according to the study of Yli-Hemminki and associates, known Fe and Mn oxidizing microbes were not dominant in the concretions. Moreover, chemolithoautotrophic Fe (oxyhydr)oxide formation in non-acidic and low oxygen conditions is driven by microbes such as *Galionella* whereas in anaerobic conditions usually by microbes utilizing nitrate and a carbon source such as acetate (Konhauser and Riding 2012). Therefore the most probable explanation is a concurrent abiotic and biotic reaction which has driven the precipitation of Fe (oxyhydr)oxides. As Ionescu and associates (2015) mention, it is hard to differentiate individual components of natural Fe precipitation. Iron sulphides on the other hand are usually formed from Fe (oxyhydr)oxides by reduction with H_2S which is a product of microbial sulphate reduction (Schoonen 2004, Butler et al. 2005, Schieber 2011). Sulphate reduction then is controlled by the availability of organic matter (Canfield and Raiswell 1991). The formation of sulphides yields metastable precursor minerals such as earlier mentioned mackinawite (FeS_{1-x}) or greigite (Fe_3S_4) in reducing sediments before transforming to pyrite (FeS_2) over time (Schieber 2011). As shown in section 2.1 equations (3) and (4), formation of these precursor Fe monosulphides increases acidity. However, sulphate reduction increases pH according to equation (2). It is thus possible that sulphate reduction and the formation of H_2S lead to increase of pH in JWTomo5 solution which was then again lowered towards circumneutral by the precipitation of FeS.

6. CONCLUSION

Combination of EDS element mapping and X-Ray Computed Tomography yields unique insights of the internal structure of spheroidal ferromanganese concretions of the Baltic Sea. With CT scanning and EDS it is possible to distinguish less dense and dense layers and determine their predominant chemical composition. The results show a clear alternating Fe and Mn-rich growth pattern and irregular dissolution features (i.e. pore networks). Fe-rich layers are more dense and Mn-rich layers form the less dense parts of the concretions occurring as 10 to 200 μm aggregates. The pore networks are mainly concentrated to the less dense Mn-rich layers and are far more extensive than the surface area of the nodules hence enabling a large area for microbial redox processes to occur. Moreover, the morphology of the pore network can be perceived with such a high resolution for the first time, indicating larger cavities in the core than near the surface of the concretions. However, the pore network extends from the surface to the core. These cavities also usually follow the contacts between Mn- and Fe-rich layers. In addition, microbe-like structures were observed from the Mn-rich layers and rod-shaped microbes from the Fe (oxyhydr)oxide flakes precipitated during the dissolution experiment, suggesting involvement of microbial processes.

The dissolution on the other hand, occurs in anoxic conditions mainly driven by sulphides formed in microbial sulphate reduction rather than direct Fe or Mn reduction. Precipitation of the dissolved metals at least in a semi-closed system is largely controlled by the presence of oxygen and sulphides and a carbon source enabling microbial sulphate and metal oxide reduction – in anaerobic conditions ferromanganese compounds are dissolved and then iron and sulphides are precipitated whereas in an aerobic environment iron (oxyhydr)oxides are precipitated. The effect of dissolution to the release of P or other compounds from Fe and Mn layers is possibly real, as this study shows that the concretions release P which may have importance in the Gulf of Finland. In contrast to the original hypothesis, it seems that the dissolution targets mainly the Fe-rich layers, but also an increase of Mn concentration within the experiment fluid was observed.

7. ACKNOWLEDGMENTS

This study was funded by K. H. Renlund's Foundation and is part of a joint project (COMICS) between the Finnish Environment Institute (SYKE), Geological Survey of Finland (GTK) and University of Helsinki. I wish to thank all who made this study possible. First of all I would like to show appreciation for my mentors prof. Juha Karhu from University of Helsinki, Deparment of Geosciences and Geography and Adj. prof. Jouni Lehtoranta from the Finnish Environment Institute for giving support, providing the samples and giving me the possibility to complete this study. I am also grateful to Aki Kallonen for invaluable advice and making the tomography imaging possible, Radoslaw Michallick for EDS imaging and counsel, Pasi Heikkilä and Matthew Hicks for guidance and treasured advice with XRF, Aarno and Mia Kotilainen for feedback, and Aleksis Karme for advice with image processing and giving his time for rendering the test tubes with 3D printer. Lastly, I wish to thank my family, friends and girlfriend Anna for supporting me during the whole process.

REFERENCES

Anufriev, G. S., Blinov, L. N., Boltenkov, B. S. and Arif, M. 2005. Chemical and Isotope Composition of Baltic Iron-Manganese Concretions. Technical Physics 50, 663–665.

Anufriev, G. S. and Boltenkov, B. S. 2007. Ferromanganese Nodules of the Baltic Sea: Composition, Helium Isotopes, and Growth Rate. Lithology and Mineral Resources 42, 240–245.

Arif, M. and Blinov, L. N. 2004. Investigation of Concretions from the Baltic Sea. Glass Physics and Chemistry 30, 359–361.

Axelsson, M. D., Rodushkin, I., Baxter, D. C., Ingri, J. and Öhlander, B. 2002. High spatial resolution analysis of ferromanganese concretions by LA-ICP-MS. Geochemical transactions 3, 40–47.

Bargar, J. R., Tebo, B. M., Bergmann, U., Webb, S. M., Glatzel, P., Chiu, V. Q. and Villalobos, M. 2005. Biotic and abiotic products of Mn(II) oxidation by spores of the marine *Bacillus sp.* strain SG-1. American Mineralogist 90, 143–154.

Bau, M., Koschinsky, A., Dulski, P. and Hein J. R. 1996. Comparison of the partitioning behaviours of yttrium, rare earth elements, and titanium between hydrogenatic marine ferromanganese crusts and seawater. Geochimica et Cosmochimica Acta 60, 1709–1725.

Berglund, B. E., Sandgren, P., Barnekow, L., Hannon, G., Jiang, H., Skog, G., and Yu, S. Y. 2005. Early Holocene history of the Baltic Sea, as reflected in coastal sediments in Blekinge, southeastern Sweden. Quaternary International 130, 111–139.

Berner, R. A. 1985. Sulphate reduction, organic matter decomposition and pyrite formation. Philosophical Transactions of the Royal Society A 315, 25–38.

Bogdanova, O. Y., Gorshkov, A. I., Novikov, G. V. and Bogdanov, Y. A. 2008. Mineralogy of Morphogenetic Types of Ferromanganese Deposits in the World Ocean. Geology of Ore Deposits 50, 462–469.

Bonneville, S., Behrends, T. and Van Cappellen, P. 2009. Solubility and dissmilatory reduction

kinetics of iron(III) oxyhydroxides: A linear free energy relationship. Geochimica et Cosmochimica Acta 73, 5273–5282.
Bridge, J. S. and Demicco, R. V. 2008. Earth surface processes, landforms and sediment deposits. Cambridge University Press, 815 pp. ISBN: 978-0-521-85780-2
Brouwer, P. 2003. Theory of XRF: getting acquainted with the principles. Almelo: PANalytical.
Burdige, D. J. 1993. The biogeochemistry of manganese and iron reduction in marine sediments. Earth-Science Reviews 35, 249–284.
Butler, I. B., Archer, C., Vance, D., Oldroyd, A. and Rickard, D. 2005. Fe isotope fractionation on FeS formation in ambient aqueous solution. Earth and Planetary Science Letters 236, 430–442.
Canfield, D. E. and Raiswell, R. 1991. Pyrite formation and fossil preservation. In: Allison, P. A. and Briggs, D. E. (edit.) Taphonomy: Releasing the Data Locked in the Fossil Record. New York, Plenum, pp. 337–387.
Canfield, D. E., Raiswell, R. and Bottrell, S. 1992. The reactivity of sedimentary iron minerals toward sulphide. American Journal of Science 292, 659–683.
Canfield, D. E., Thamdrup, B. and Hansen, J. W. 1993. The anaerobic degradation of organic matter in Danish coastal sediments: iron reduction, manganese reduction, and sulphate reduction. Geochimica et Cosmochimica Acta 57, 3867–3883.
Canfield, D. E., Thamdrup, B. and Fleischer, S. 1998. Isotope fractionation and sulfur metabolism by pure and enrichment cultures of elemental sulfur-dispoportionating bacteria. Limnology and Oceanography 43, 253–264.
Chester, R. 1990. Marine geochemistry 1. Oceans, chemical composition & chemical properties. London, Unwin Hyman Ltd., 698 p.
Chukhrov, F. V., Zvyagin, B. B., Yermilova, L. P. and Gorshkov, A. I. 1976. Mineralogical criteria in the origin of marine iron-manganese nodules. Mineralium Deposita 11, 24–32.
Cnudde, V., Masschaele, B., Dierick, M., Vlassenbroeck, J., Van Hoorebeke, L. and Jacobs, P. 2006. Recent progress in X-ray CT as a geosciences tool. Applied Geochemistry 21, 826–832.
Coleman, M. L. 1985. Geochemistry of diagenetic non-silicate minerals: Kinetic considerations. Philosophical Transactions of the Royal Society A 315, 39–56.
Conley, D. J., Björck, S., Bonsdorff, E., Carstensen, J., Destouni, G., Gustafsson, B. G., Hietanen, S., Kortekaas, M., Kuosa, H., Meier, H. E. M., Müller-Karulis, B., Nordberg, K., Norkko, A., Nürnberg, G., Pitkänen, H., Rabalais, N. N., Rosenberg, R., Savchuck, O. P., Slomp, C. P., Voss, M., Wulff, F. and Zillén, L. 2009. Hypoxia-Related Processes in the Baltic Sea. Environmental Science and Technology 43, 3412−3420. DOI: 10.1021/es802762a
Curtis, C. D. 1983. Microorganisms and diagenesis of sediments. In: Krumbein,W. E. (edit.) Microbial geochemistry. Blackwell, p. 263–286.
Donald, R. and Southam, G. 1999. Low temperature anaerobic bacterial diagenesis of ferrous monosulfide to pyrite. Geochimica et Cosmochimica Acta 63, 2019–2023. DOI: 10.1016/S0016-7037(99)00140-4.
Duan, W. M., Hedrick, D. B., Pye, K., Coleman, M. L. and White, D. C. 1996. A preliminary study of the geochemical and microbiological characteristics of modern sedimentary concretions. Limnology and Oceanography 41, 1404–1414.
Edwards, K. J., Bach, W. and McCollom, T. M. 2005. Geomicrobiology in oceanography: microbe-mineral interactions at and below the seafloor. Trends in Microbiology 13, 456–494.
Egger, M., Rasigraf, O., Sapart, C. J., Jilbert, T., Jetten, M. S. M., Röckmann, T., van der Veen, C., Bândă, N., Kartal, B., Ettwig, K. F. and Slomp, C. P. 2015. Iron-Mediated Anaerobic Oxidation of Methane in Brackish Coastal Sediments. Environmental Science and Technology 49, 277–283. DOI: dx.doi.org/10.1021/es503663z.
Emelyanov, E. M. 1986. Basins of the Baltic Sea. Finnish Marine Research 253, 79–96.
Feldkamp, L. A., Davis, L. C. and Kress, J. W. 1984. Practical cone-beam algorithm. Journal of the Optical Society of America A 1, 612–619.
Fowle, D. A. and Fein, J. B. 2001. Quantifying the effects of *Bacillus subtilis* cell walls on the precipitation of copper hydroxide from aqueous solution. Geomicrobiology Journal 18, 77–

91.
Gasparatos, D., Tarenidis, D., Haidouti, C. and Oikonomou, G. 2005. Microscopic structure of soil Fe-Mn nodules: environmental implication. Environmetal Chemistry Letters 2, 175–178. DOI: 10.1007/s10311-004-0092-5.
Ghiorse, W. C. and Hirsch, P. 1982. Isolation and Properties of Ferromanganese-Depositing Budding Bacteria from Baltic Sea Ferromanganese Concretions. Applied and Environmental Microbiology 43, 1464–1472.
Ghiorse, W. C. 1984. Biology or iron- and manganese-depositing bacteria. Annual Reviews in Microbiology 38, 515–550.
Glasauer, S., Langley, S. and Beveridge, T. J. 2001. Sorption of Fe hydr(oxides) to the surface of *Shewanella putrefaciens:* cell-bound fine-grained minerals are not always formed de novo. Applied and Environmental Microbiology 67, 5544–5550.
Glasby, G. P. 1974. Mechanism of incorporation of manganese and associated trace elements in marine manganese nodules. Oceanography and Marine Biology – An Annual Review 12, 11–40.
Glasby, G. P., Emelyanov, E. M., Zhamoida, V. A., Baturin, G. N., Leipe, T., Bahlo, R. and Bonacker, P. 1997. Environment of formation of ferromanganese concretions in the Baltic Sea: A critical review. In Nicholson, K., Hein, J. R., Bühn, B. and Dasgupta, S. (edit.): Manganese Mineralization: Geochemistry and Mineralogy of Terrestrial and Marine Deposits. Geological Society Special Publication 119, 213–237.
Graham, J. W. and Cooper, S. C. 1959. Biological origin of manganese-rich deposits on the sea floor. Nature 183, 1050–1051.
Grigoriev, A. G., Zhamoida, V. A., Gruzdov, K. A. and Krymsky, R. Sh. 2013. Age and Growth Rates of Ferromanganese Concretions from the Gulf of Finland Derived from ^{210}Pb Measurements. Oceanology 33, 345–351.
Gu, B., Schmitt, J., Chen, Z., Liang, L. and McCarthy, J. F. 1994. Adsorption and Desorption of Natural Organic Matter on Iron Oxide: Mechanisms and Models. Environmental Science & Technology 28, 38–46.
Gustafsson, O., Widerlund, A., Andersson, P. S., Ingri, J., Roos, P. and Ledin, A. 2000. Colloid dynamics transport of major elements through boreal river-brackish bay mixing zone. Marine Chemistry 71, 1–21.
Halbach, P. and Puteanus, D. 1984. The influence of carbonate dissolution rate on the growth and composition of Co-rich ferromanganese crusts from Central Pacific seamount areas. Earth and Planetary Science Letters 68, 73–87.
Heiri, O., Lotter, A. F. and Lemcke, G. 2001. Loss on ignition as a method for estimating organic and carbonate content in sediments: reproducibility and comparability of results. Journal of Paleolimnology 25, 101–110.
Hlawatsch, S., Garbe-Schönberg, C. D., Lechtenberg, F., Manceau, A., Tamura, N., Kulik, D. A. and Kersten, M. 2002. Trace metal fluxes to ferromanganese nodules from the western Baltic Sea as a record for long-term environmental changes. Chemical Geology 182, 697–709.
Hosseinkhani, B. and Emtiazi, G. 2011. Synthesis and Characterization of a Novel Extracellular Biogenic Manganese Oxide (Bixbyite-like Mn_2O_3) Nanoparticle by Isolated *Acinetobacter* sp. Current Microbiology 63, 300–305. DOI: 10.1007/s00284-011-9971-8.
Hu, W., Zhou, H., Gu, L., Zhang, W., Lu, X., Fu, Q., Pan, J. and Zhang, H. 2000. New evidence of microbe origin for ferromanganese nodules from the East Pacific deep sea floor. Science in China 43, 187–192.
Hyacinthe, C., Bonneville, S. and Van Cappellen, P. 2006. Reactive iron(III) in sediments: chemical versus microbial extractions. Geochimica et Cosmochimica Acta 70, 4166–4180.
Ingri, J. and Pontér, C. 1986. Scavenging properties of ferromanganese nodules in the Gulf of Bothnia. Rapports et Proces-verbaux des Réunions. Conseil International pour l'Éxploration de la Mer 186, 234–243.
Ionescu, D., Heim, C., Polerecky, L., Thiel, V. and De Beer, D. 2015. Biotic and abiotic oxidation and reduction of iron at circumneutral pH are inseparable processes under natural conditions. Geomicrobiology Journal 32, 221–230. DOI: 10.1080/01490451.2014.887393
Iordan, E. P., Bryukhanov, A. L., Dunaevskii, Ya. E., Pryanishnikova, N. I. and Danilova, I. V.

2000. Manganese-Dependent Ribonucleotide Reductase of *Propionibacterium freudenreichii* subsp. *shermanii*: Partial Purification, Characterization, and Role in DNA Biosynthesis. Microbiology 69, 387–392.

Jensen, J. B. 1995. A Baltic ice lake transgression in the southwestern Baltic: evidence from Fakse Bugt, Denmark. Quaternary International 27, 59–68.

Jones, J. G., Crowe, S. A., Sturm, A., Leslie, K. L., MacLean, L. C. W., Katsev, S., Henny, C., Fowle, D. A. and Canfield, D. E. 2011. Biogeochemistry of manganese in ferruginous Lake Matano, Indonesia. Biogeosciences 8, 2977–2991.

Kendall, B., Anbar, A. D., Kappler, A. and Konhauser, K. O. 2012. The Global Iron Cycle. In: Knoll, A. H., Canfield, D. E. and Konhauser, K. O. (edit.) Fundamentals of Geobiology, Wiley-Blackwell, 456 pp.

Klinkhammer, G. P. 1980. The distribution of manganese in the Pacific Ocean. Earth and Planetary Science Letters 46, 361–384.

Kochinsky, A. and Halbach, P. 1995. Sequential leaching of marine ferromanganese precipitates: Genetic implications. Geochimica et Cosmochimica Acta 59, 5113–5132.

Konhauser, K. O. 2007. Introduction to Geomicrobiology. Blackwell, Oxford, 425 pp.

Konhauser, K. O. and Riding, R. 2012. Bacterial Biomineralization. In: Knoll, A. H., Canfield, D. E. and Konhauser, K. O. (edit.) Fundamentals of Geobiology, Wiley-Blackwell, 456 pp.

Krachler, R., Krachler, R. F., von der Krammer, F., Süphandag, A., Jirsa, F., Ayromlou, S., Hofmann, T. and Keppler, B. K. 2010. Relevance of peat-draining rivers for the riverine input of dissolved iron into the ocean. Science of The Total Envrironment 408, 2402–2408.

Krishnamurti, G. S. R. and Huang, P. M. 1988. Influence of manganese oxide minerals on the formation of iron oxides. Clays and Clay Minerals 36, 467–475.

Lahermo, P., Väänänen, P., Tarvainen, T. ja Salminen, R. 1996. Geochemical Atlas of Finland Part 3: Environmental geochemistry – stream waters and sediments. Geological Survey of Finland, 151 p.

Lawes, G. 1987. Scanning electron microscopy and X-ray microanalysis: analytical chemistry by open learning. Wiley, London, 122 p.

Lehtoranta, J. 2003. Dynamics of sediment phosphorus in the brackish Gulf of Finland. Monographs of the Boreal Environment Research 24, 58 p.

InteLehtoranta, J., Ekholm, P., Wahlström, S., Tallberg, P. and Uusitalo, R. 2015. Labile organic carbon regulates phosphorus release from eroded soil transported into anaerobic coastal systems. Ambio 44, 263–273. DOI: 10.1007/s13280-014-0620-x

Leppäranta, M. and Myrberg, K. 2009. Physical Oceanography of the Baltic Sea. Springer, 378 pp. DOI: 10.1007/978-3-540-79703-6

Lovley, D. R. 1991. Dissimilatory Fe(III) and Mn(IV) reduction. Microbiological Reviews 55, 259–287.

Lovley, D. R., Giovannoni, S. J., White, D. C., Champine, J. E., Philips, E. J. P., Gorby, Y. A. and Goodwin, S. 1992. *Geobacter Metallireducens* gen. nov. sp. nov., a microorganism capable of coupling the complete oxidation of organic compounds to the reduction of iron and other metals. Archives of Microbiology 159, 336–344.

Luther, G. W. III 1991. Pyrite synthesis via polysulphide compounds. Geochimica et Cosmochimica Acta 55, 2839–2849.

Marcus, M. A., Manceau, A. and Kersten, M. 2004. Mn, Fe, Zn and As speciation in a fast-growing ferromanganese marine nodule. Geochimica et Cosmochimica Acta 68, 3125–3136.

McCollom, T. M. 2000. Geochemical constraints on primary productivity in submarine hydrothermal vent plumes. Deep-sea Research 47, 85–101.

Miyata, N., Tani, Y., Sakata, M. and Iwahori, K. 2007. Microbial Manganese Oxide Formation and Interaction with Toxic Metal Ions. Journal of Bioscience and Bioengineering 104, 1–8.

Mortimer, R. J. G., Galsworthy, A. M. J., Bottrell, S. H., Wilmot, L. E. and Newton, R. J. 2011. Experimental evidence for rapid biotic and abiotic reduction of Fe(III) at low temperatures in salt marsh sediments: a possible mechanism for formation of modern sedimentary siderite concretions. Sedimentology 58, 1514–1529.

Munch, J. C. and Ottow, J. C. G. 1983. Reductive transformation mechanism of ferric oxides in hydromorphic soils. Environmental Biogeochemistry Ecological Bulletins 35, 383–394.

Och, L. M., Müller, B., Voegelin, A., Ulrich, A., Göttlicher, J., Steiniger, R., Mangold, S., Vologina, E. G. and Srum, M. 2012. New insights into the formation and burial of Fe/Mn accumulations in Lake Baikal sediments. Chemical Geology 330–331, 244–259.

Ojala, E.-J. 2008. Itämeren rauta-mangaanisaostumien geokemiaa – rauta, mangaani, fosfori ja kalsium vyöhykkeellisyyden suhteen. Master of Science thesis, University of Helsinki, Department of Geology, 61 pp. (In Finnish)

Pakhomova, S. V., Hall, P. O. J., Kononets, M. Y., Rozanov, A. G., Tengberg, A. and Vershinin, A. 2007. Fluxes of iron and manganese across the sediment-water interface under various redox conditions. Marine Chemistry 107, 319–331.

Perttilä, M., Tulkki, P. and Pietikäinen, S. 1980. Mean values and trends of hydrographical and chemical properties of the Gulf of Finland. Finnish Institute of Marine Research 247, 38–50.

Pitkänen, H., Lehtoranta, J. and Peltonen, H. 2008. The Gulf of Finland. In: Schiewer, U. (edit.) Ecology of Baltic Coastal Waters, Ecological Studies 197, Springer, 285–308. DOI: 10.1007/978-3-540-73524-3_13

Post, J. E. 1999. Manganese oxide minerals: crystal structures and economic and environmental significance. PNAS 96, 3447–3454.

Postma, D. 1985. Concentrations of Mn and separation from Fe in sediments -1. Kinetics and stoichiometry of the reaction between birnessite and dissolved Fe(II) at 10 °C. Geochimica et Cosmochimica Acta 49, 1023–1033.

Poulton, S. W., Krom, M. D. and Raiswell, R. 2004. A revised scheme for the reactivity of iron (oxyhydr)oxide minerals towards dissolved sulphide. Geochimica et Cosmochimica Acta 68, 3703–3715.

Poulton, S. W. and Raiswell, R. 2002. The low-temperature geochemical cycle of iron: from conctinental fluxes to marine sediment deposition. American Journal of Science 302, 774–805.

Raiswell, R. and Canfield, D. E. 2012. The Iron Biogeochemical Cycle Past and Present. In: Benning, L. G., Elliott, T., Oelkers, E. H. and Stipp, S. L. S. (edit.) Geochemical Perspectives 1, 232 pp.

Raiswell, R. and Canfield, D. E. 1996. Rates of reaction between silicate iron and dissolved sulphide in Peru Margin sediments. Geochimica et Cosmochimica Acta 60, 2777–2787.

Reimann, C., Siewers, U., Tarvainen, T., Bitykova, L., Eriksson, J., Gilucis, A., Gregorauskiene, V., Lukashev, V., Matinian, N. N. ja Pasieczna, A. 2000. Baltic soil survey: total concentrations of major and selected trace elements in arable soils from 10 countries around the Baltic Sea. The Science of the Total Environment 257, 155–170.

Rizescu, C. T., Georgescu, G. N., Duliu, O. G. and Szobotka, S. A. 2001. 3-D dual gamma-ray computer axial tomography investigation of polymetallic nodules. Deep-Sea Research I 48, 2529–2540.

Schieber, J. 2011. Iron sulphide formation. In: Reitner, J. and Thiel, V. (edit.) Encyclopedia of Geobiology, Springer, pp. 486–502. DOI: 10.1007/978-1-4020-9212-1_118.

Schmitz, R. A., Daniel, R., Deppenmeier, U. and Gottschalk, G. 2006. The Anaerobic Way of Life. Falkow, S., Roseberg, E., Schleifer, K.-H. and Stackebrandt, E. (edit.) The Procaryotes 2: Ecophysiology and Biochemistry, Springer, 86–101.

Schoonen, M. 2004. Mechanisms of sedimentary pyrite formation. Geological Society of America Special Paper 379, 117–134.

Somayajulu, B. L. K. 2000. Growth rate of oceanic manganese nodules: implications to their genesis, palaeo-earth environment and resource potential. Current Science 78: 300–308.

Suess, E. and Djafari, D. 1977. Trace metal distribution in Baltic Sea ferromanganese concretions: inferences on accretion rates. Earth and Planetary Science Letters 35, 49–54.

Svensson, N.-O. 1989. Late Weichselian and early Holocene shore displacement in the central Baltic Sea. Quaternary International 9, 7–26.

Tebo, B. M., Ghiorse, W. C., van Waasbergen, L. G., Siering, P. L. and Caspi, R. 1997. Bacterially mediated mineral formation: insights into manganese(II) oxidation from

molecular genetic and biochemical studies. In: Banfield, J. F. and Nealson, K. H. (edit.) Geomicrobiology: interactions between microbes and minerals. Mineral Society of America, Washington, DC, pp. 225–266.

Tebo, B. M., Bargar, J. R., Clement, B. G., Dick, G. J., Murray, K. J., Parker, D., Verity, R. and Webb, S. M. 2004. Biogenic manganese oxides: Properties and mechanisms of formation. Annual Review of Earth and Planetary Sciences 32, 287–328.

Tebo, B. M., Clement, B. G. and Dick, G. J. 2007. Biotransformations of manganese. In: Hurst, C. J., Crawford, R. L., Garland, J. L., Lipson, D. A., Mills, A. L. and Stetzenbach, L. D. (edit.) Manual of environmental microbiology. ASM Press, Washington, DC, pp. 1223–1238.

Telesh, I. V., Golubkov, S. M. and Alimov, A. F. 2008. The Neva Estuary Ecosystem. In: Schiewer, U. (edit.) Ecology of Baltic Coastal Waters, Ecological Studies 197, Springer, 259–284. DOI: 10.1007/978-3-540-73524-3_12

Thamdrup, B., Glud, R. N. and Hansen, J. W. 1994. Manganese oxidation and in situ manganese fluxes from coastal sediment. Geochimica et Cosmochimica Acta 58, 2563–2570.

Thiel, G. A. 1925. Manganese precipitated by microorganisms. Economic Geology 20, 301–310.

Vasconcelos, C. and McKenzie, J.A. 2009. The Descent of Minerals. Science 323, 218–219.

Wang, X., Schröder, H. C., Schloßmacher, U. and Müller, W. E. G. 2009a. Manganese/polymetallic nodules: Micro-structural characterization of exolithobiontic- and endolithobiontic microbial biofilms by scanning electron microscopy. Micron 40, 350–358. DOI: 10.1016/j.micron.2008.10.005.

Wang, X., Gan, L. and Müller, W. E. G. 2009b. Contribution of biomineralization during growth of polymetallic nodules and ferromanganese crusts from the Pacific Ocean. Frontiers of Materials Science China 3, 109–123. DOI: 10.1007/s11706-009-0033-0.

Wang, X., Schröder, H. C., Schloßmacher, U. and Müller, W. E. G. 2009c. Organized bacterial assemblies in manganese nodules: evidence for a role of S-layers in metal deposition. Geo-Marine Letters 29, 85–91.

Wang, X., Wiens, M., Schröder, H. C., Schloßmacher, U. and Müller, W. E. G. 2011. Molecular biomineralization: toward an understanding of the biogenic origin of polymetallic nodules, crusts, and hydrothermal vents. In: Müller W. E. G. (edit.) Molecular Biomineralization: Aquatic Organisms Forming Extraordinary Materials, Progress in Molecular and Subcellular Biology 52, Springer, Berlin, pp.77–110. DOI: 10.1007/978-3-642-21230-7_4.

Weber, K. A. and Coates, J. D. 2007. Microbially Mediated Anaerobic Iron(II) Oxidation at Circumneutral pH. In: Hurst, C. J., Crawford, R. L., Garland, J. L., Lipson, D. A., Mills, A. L. and Stetzenbach, L. D. (edit.) Manual of environmental microbiology. ASM Press, Washington, DC, pp. 1147–1154.

Werdanskij, W. I. 1930. Geochemie in ausgewahlten Kapiteln. Akademische Verlagsgesellschaft m.b.H., Leipzig, 370 p. (Verdansky, V. I. 1934. Studies on Geochemistry. Gorgeonefteizdat, Moscow.)

Whiston, C. 1987. X-Ray Methods. Analytical Chemistry by Open Learning. Wiley, London, 426 pp.

Wightman, P. G. and Fein, J. B. 2005. Iron adsorption by *Bacillus subtilis* bacterial cell walls. Chemical Geology 216, 177–189. DOI: 10.1016/j.chemgeo.2004.11.008

Winterhalter B. 1966. Pohjanlahden ja Suomenlahden rauta-mangaani-saostumista. Geoteknillisiä julkaisuja 69, Geologian Tutkimuslaitos, Otaniemi. 77 s. (In Finnish)

Winterhalter B. 2004. Ferromanganese Concretions in the Gulf of Bothnia. In: Harff J., Emelyanov E., Schmidt-Thome M. and Spiridonov M. (edit.) Mineral Resources of the Baltic sea –Exploration, Exploitation and Sustainable Development. Zeitschrift fur Angewandte Geologie, special issue 2, Hannover, 199–212.

Winterhalter, B. and Siivola, J.1967. An electron microprobe study of the distribution of iron, manganese and phosphorus in concretions from the Gulf of Bothnia, Northern Baltic Sea. Geological Society of Finland 39, 161–172.

Winterhalter, B., Ignatius, H., Axberg, S., NIemistö, L. 1981. Geology of the Baltic Sea. In:

Voipio, A. (edit.) The Baltic Sea. Oceanography Series, Elsevier, 121 p.
Yao, W. and Millero, F. J. 1996. Oxidation of hydrogen sulphide by hydrous Fe(III) oxides in seawater. Marine Chemistry 52, 1–16.
Yli-Hemminki, P., Jørgensen, K. S. and Lehtoranta, J. 2014. Iron-Manganese Concretions Sustaining Microbial Life in the Baltic Sea: The Structure of the Bacterial Community and Enrichments in Metal-Oxidizing Conditions. Geomicrobiology Journal 31, 263–275. DOI: 10.1080/01490451.2013.819050
Zee, van der, C., Roberts, D. R., Rancourt, D. G. and Slomp, C. P. Nanogoethite is the dominant reactive oxyhydroxide phase in lake and marine sediments. Geology 31, 993–996. DOI: 10.1130/G19924.1
Zhamoida, V. A., Glasby, G. P., Grigoriev, A. G., Manuilov, S. F., Moskalenko, P. E. and Spridonov, M. A. 2004. Distribution, morphology, composition and economic potential of ferromanganese concretions from the eastern Gulf of Finland. In: Harff, J., Emelyanov, E., Schmidt-Thomé, M. and Spiridonow, M. (edit.): Mineral Resources of the Baltic sea – Exploration, Exploitation and Sustainable Development. Zeitschrift für Angewandte Geologie, special issue 2, Hannover, 213–226.
Zhamoida, V., Grigoriev, A., Gruzdov, K. and Ryabchuk, D. 2007. The influence of ferromanganese concrections-forming processes in the eastern Gulf of Finland on the marine environment. The Quarternary deposits of the Eastern Gulf of Finland. Geological Survey of Finland, Special Paper 45, 21–32.
Zhang, F. -S., Lin, C. -Y., Bian, L. -Z., Glasby, B. G. and Zhamoida, V. A. 2002. Possible evidence for the biogenic formation of spheroidal ferromanganese concretions from the eastern Gulf of Finland, the Baltic Sea. Baltica 15, 23–29.

APPENDICES

Appendix A – Tomography samples

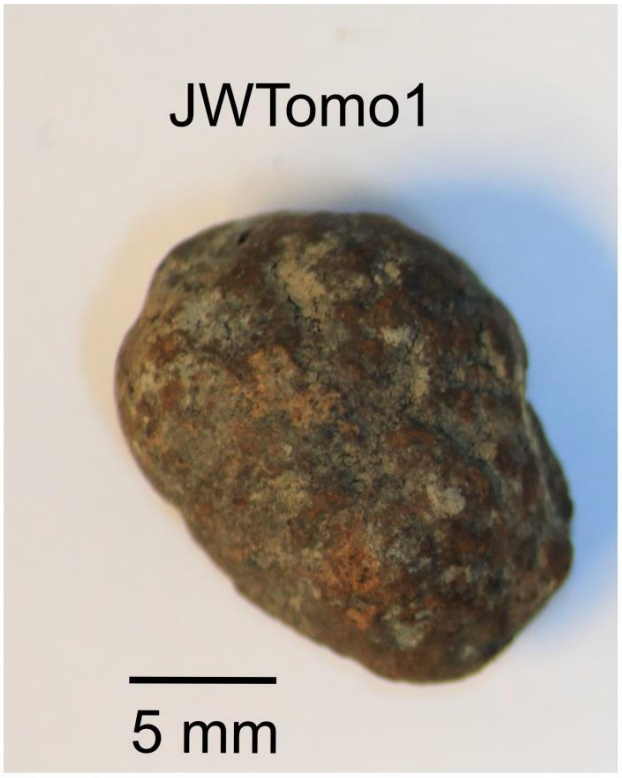


JWTomo5
5 mm

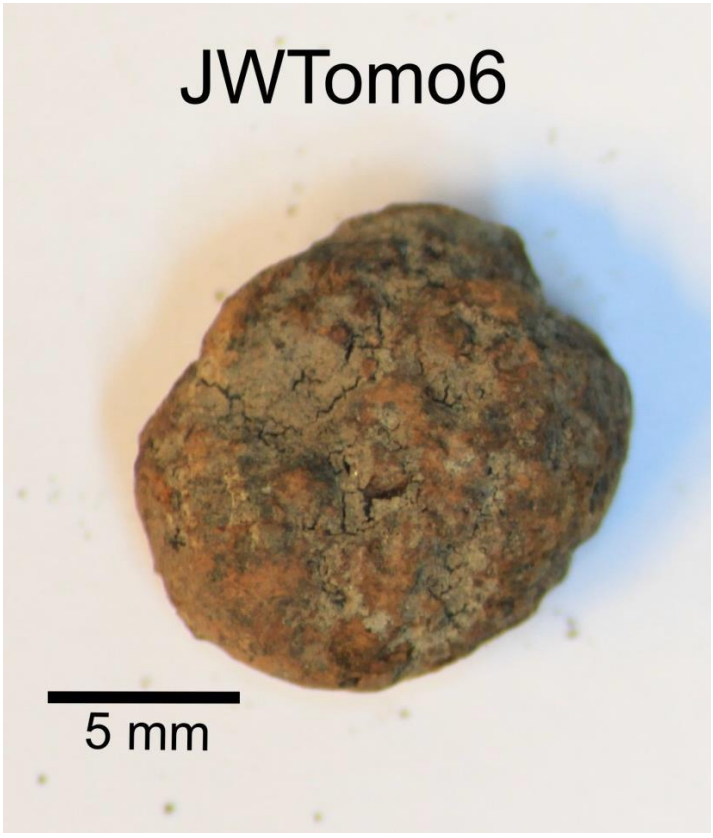
JWTomo6
5 mm

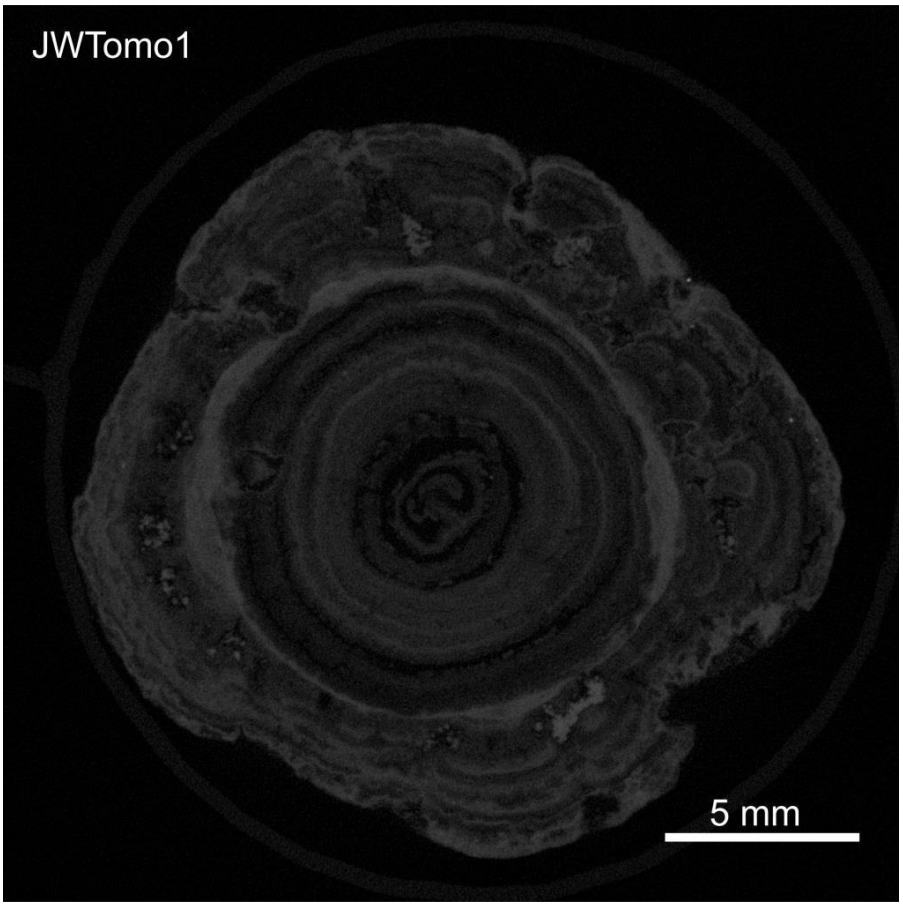
JWTomo1
5 mm

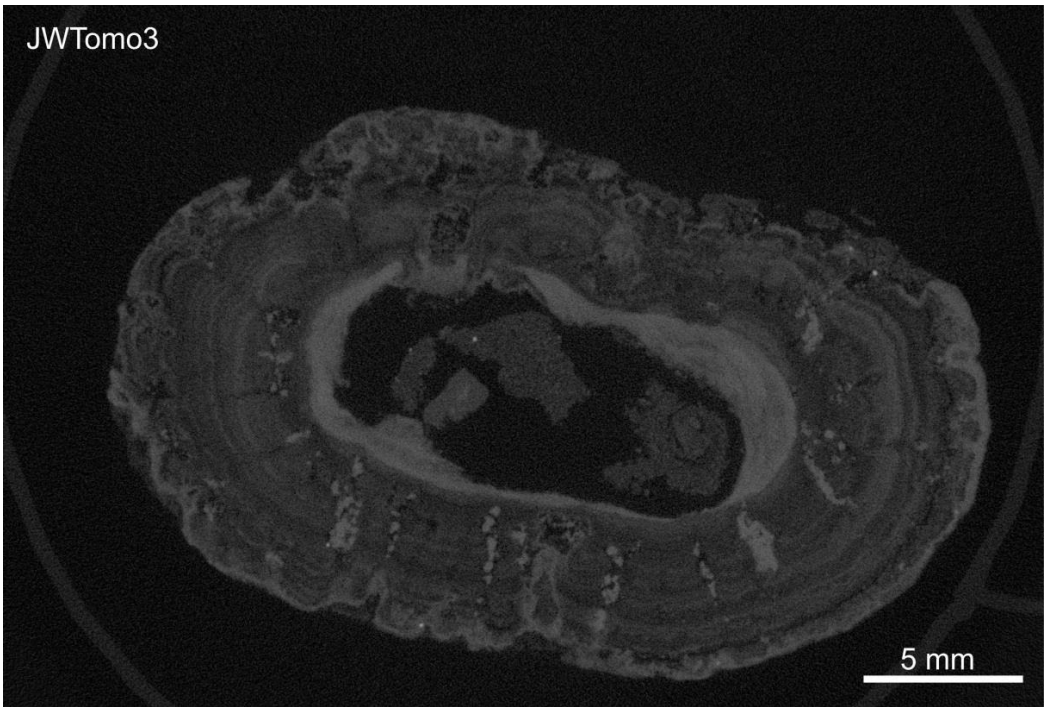
JWTomo3
5 mm

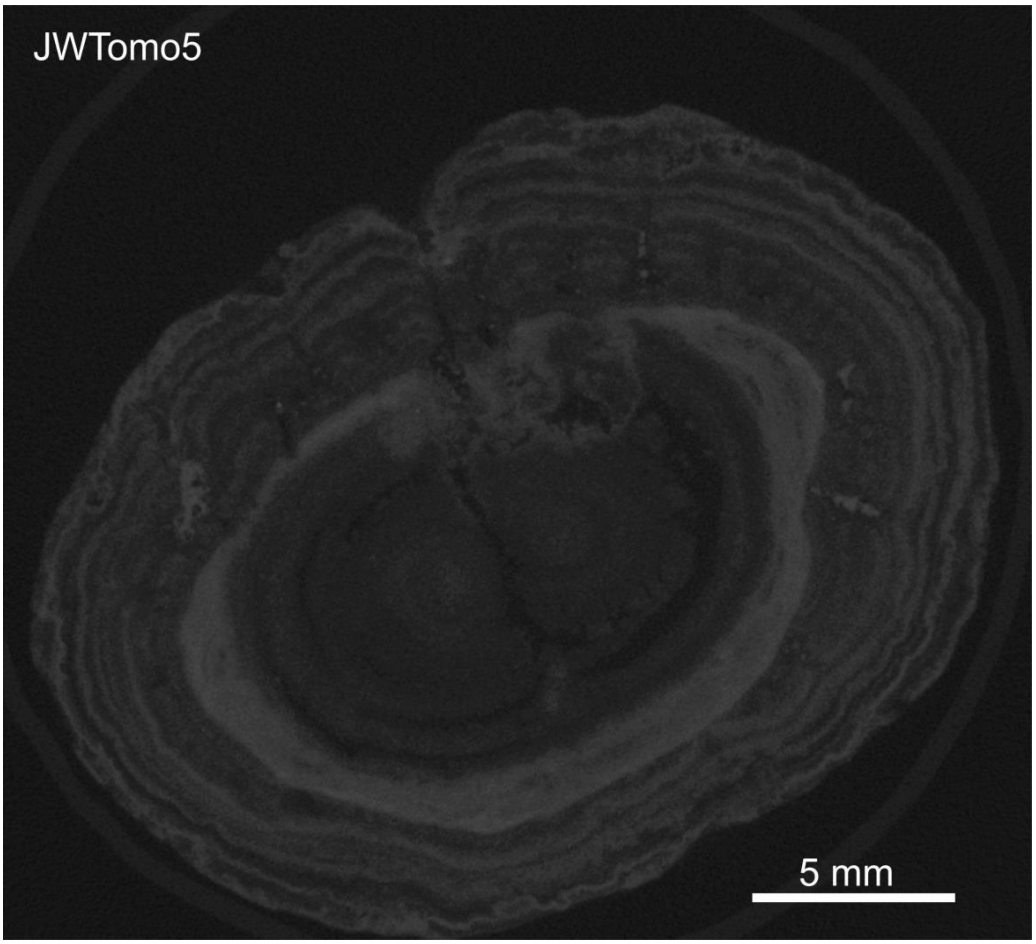
JWTomo5
5 mm

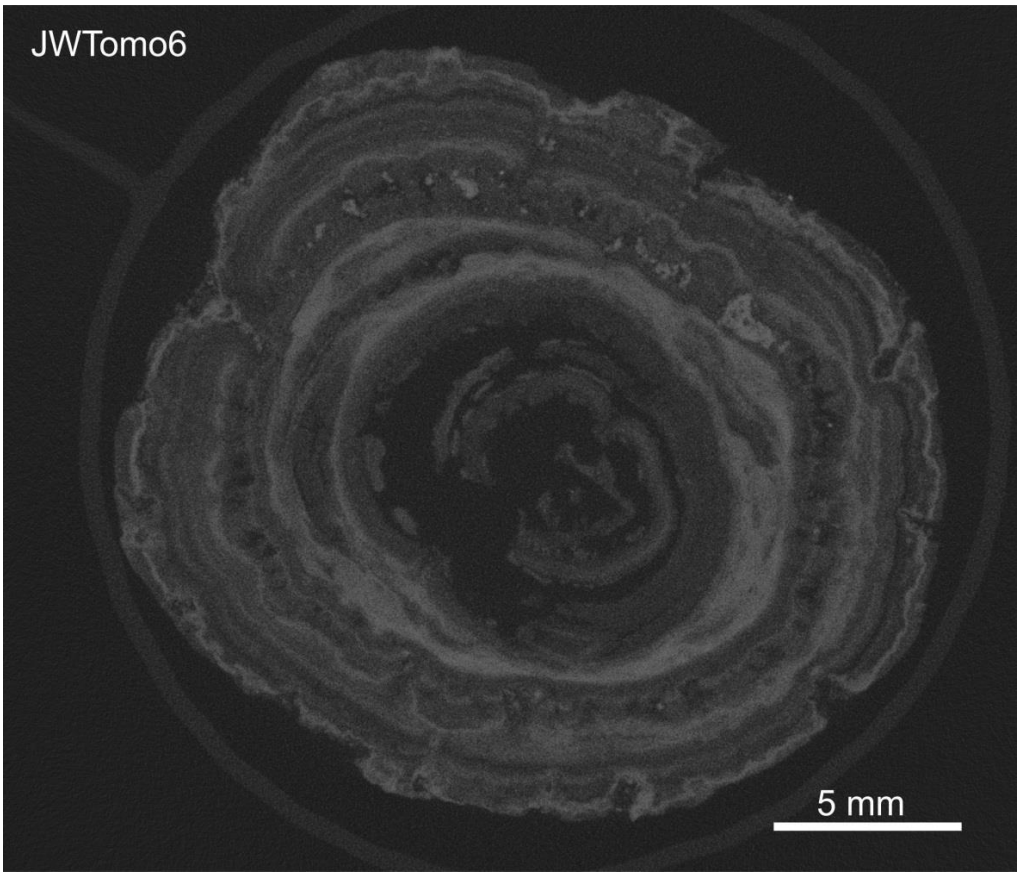
JWTomo6
5 mm

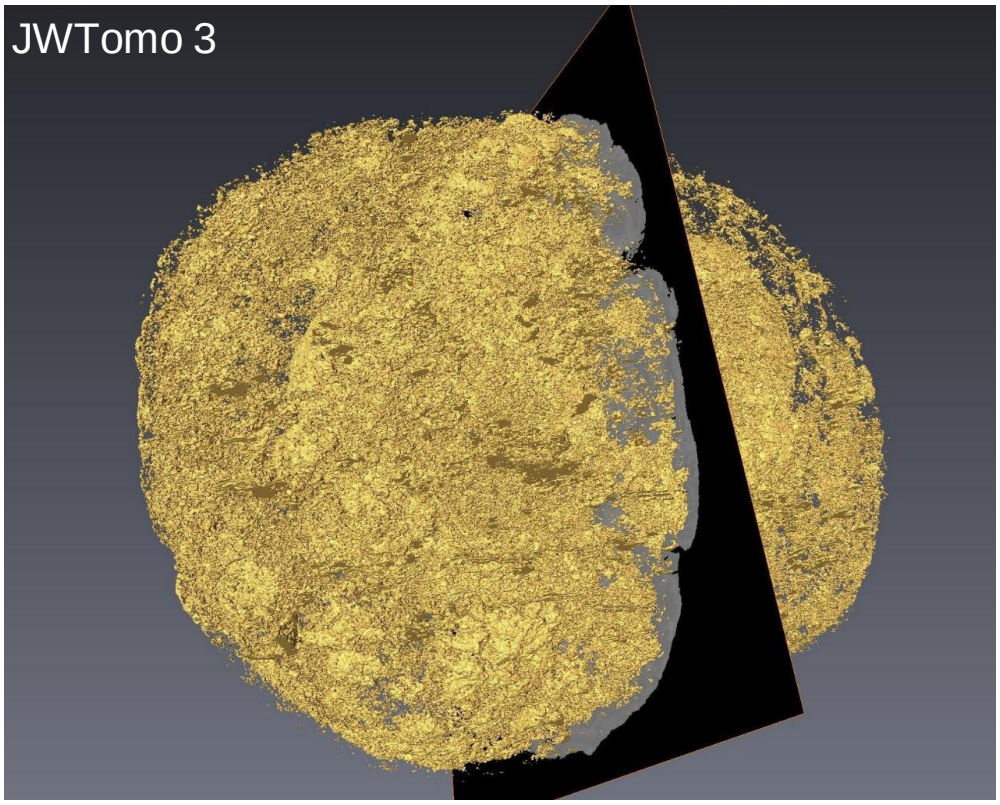
JWTomo 3

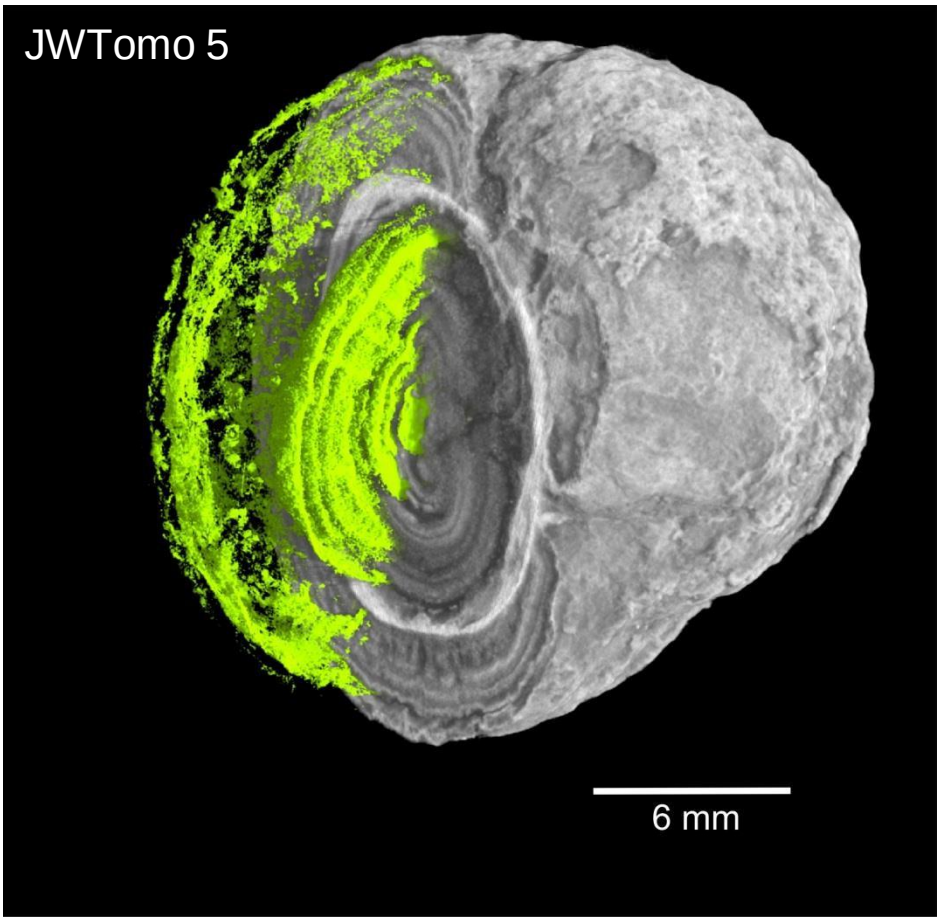
JWTomo 5
6 mm

Test tubes used for tomography samples

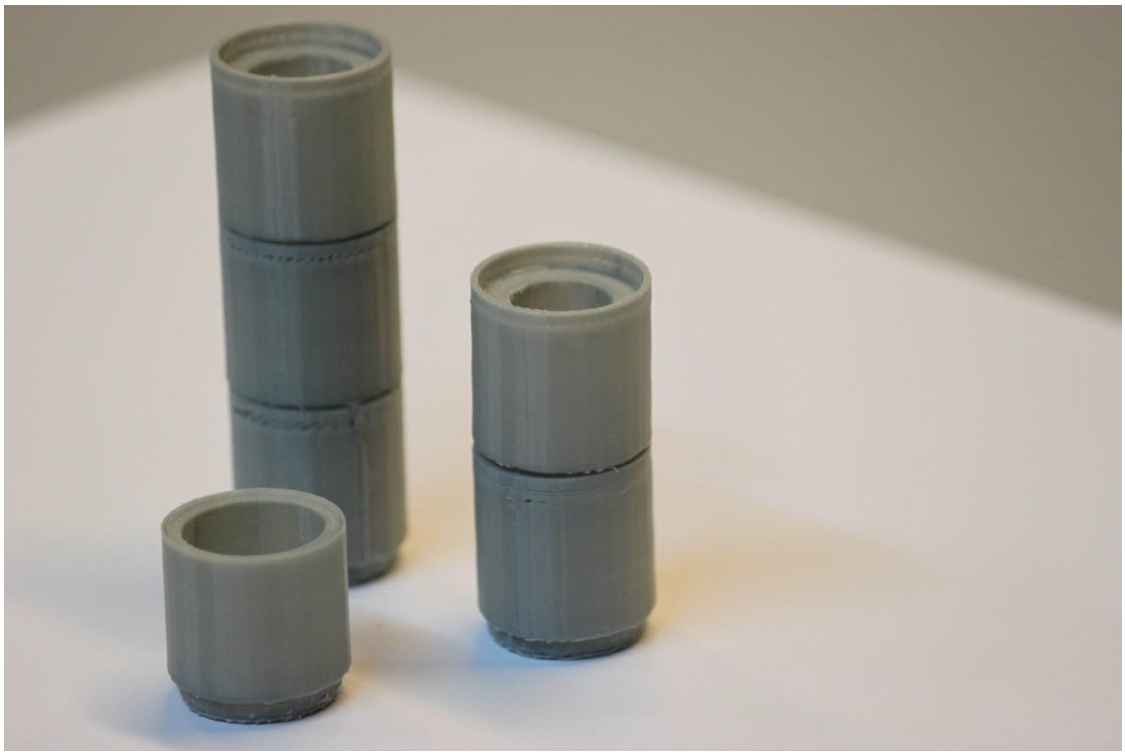

Appendix B – X-Ray tomography imaging log (setups for X-ray source, measuring geometry and detector)

[GENERAL]
Version=datosx_acq.exe version
1.3.3.6 Comment=

[GEOMETRY]
Magnification=5.26318119
Voxelsize=0.00949996
CorrValue=0.00000000
FOD=94.99949646
FDD=499.99957275
TiltAngle=0.00000000

[ACQUISITION]
NumberImages=900
NumberFastSkip=0
NumberFastAv=1
ImgStart=901
VSensorStart=0
TotalRotation=360.000000
00 ImgInterval=150
ImgRect_Top=0
ImgRect_Left=0
ImgRect_Bottom=2303
ImgRect_Right=2303
DimX=2280
DimY=2304
ImgBitspp=12
SubSample=0
MirrorImgX=0
MirrorImgY=0
Rotation=0
WarmUp=1
WarmUp_TimeTriggered=0
WarmUp_GrayValueTriggered=0
WarmUp_DoseTriggered=0
WarmUp_Window_left=0
WarmUp_Window_right=11
WarmUp_Window_top=868
WarmUp_Window_bottom=1202
WarmUp_GreyValue=1654.00000000
WarmUp_Deviation=20.00000000
WarmUp_Voltage=185
WarmUp_Time=1
Scaling=0
FreeRay=1773
Multiscan_Activ=1
Multiscan_NrScans
=5
Multiscan_ActNrScans=5
Multiscan_Dist=24.00000000
VSensor_Tiles=1
VSensor_TileType=2
VSensor_Overlap=9
VSensor_SensorDistance=15.00000000
VSensor_SensorStartPos=10.00000000
VSensor_SensorXOffset=0.00000000
VSensor_AdjustImg=0
FastCT=0
ShortScan=0
ImageUpdateEnable
=1 MGainMode=1
ShsStart=0.0000000
0
ShsStop=360.00000000

NoRot=0
ETime=33895
RTime=-115
STime=33779
SImgDone=901
SImgScan=901
CtType=0
ObjectDiameter=0.00000000
ShiftpT=0
NumTurns=0
TransCtVFactor=1.00000000
DetMoveMode=0
DetMoveEnable=1
DetMoveAmplitude=12
DetMoveInterval=1
DetMoveStep=1
AddSwBinning=0

[DETECTOR]
Binning=0
Timing=2
TimingVal=1000 ms
Averaging=5
Averaging_Cal=100
Skip=1
Blocksize=0
IntervalSkip=10
CalPoints=4
Sensor=HCD-5184-50
PixelsizeX=0.05000000
PixelsizeY=0.05000000
Bitspp=12
NrPixelsX=2304
NrPixelsY=2304
MultipleGainVoltages=170;170;170;170;
MultipleGainCurrents=20;40;80;160;
GainImg=I:\CT Data\AK\Karhu\FeMn series 1\3D printed holder\test1_gain_150_170_1250ms_1Det.his
MultGainImg=I:\CT Data\Alexander\Rapakivi\Rapakivi A\Series3\Series3_2_6_MultGain_1500ms_4p_1Det_.his
OffsetImg=I:\CT Data\AK\Karhu\FeMn series 1\3D printed holder\test1_offset_1250_.his
DefPixelImg=C:\Program Files\phoenix x-ray\datosx acq\CalibrationImages\pixmask_B1x1_x2304_y2304.his
CameraGain=0

[XRAY]
Voltage=150
Current=170
Mode=0
KLNumber=0
XRayFilter=Cu
XRayFilterThickness=0.5
Tube=phoenix|x-ray 180 kV
TubeID=1080
PFocus=0
TargetDose=0.00000000
DoseType=0

[CNC]
XS=0.00000000
YS=118.49991667
YT=0.00000000
ZS=94.99950000
TS=0.00000000
RS=359.99980000
XD=0.00000000
YD=0.00000000
ZD=499.99956250
WD=0.00000000
V1=0.00000000
V2=0.00000000

Appendix C – element mapping images

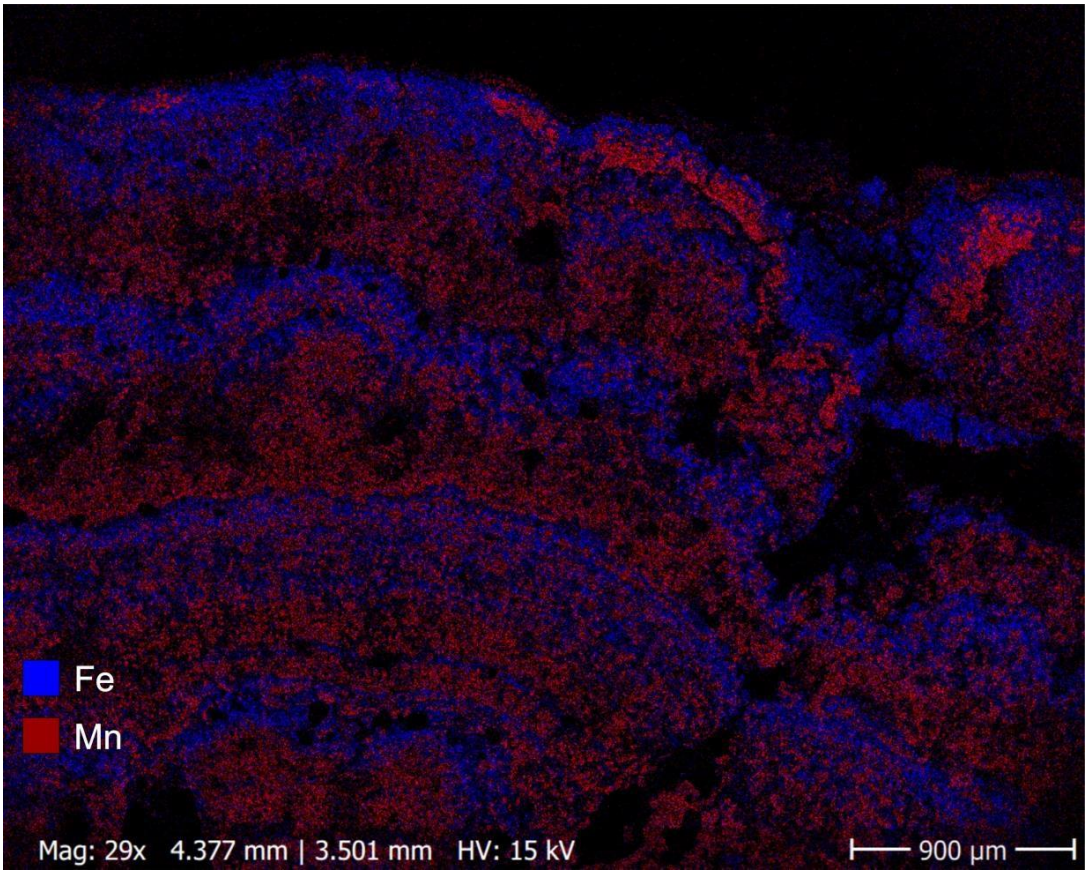

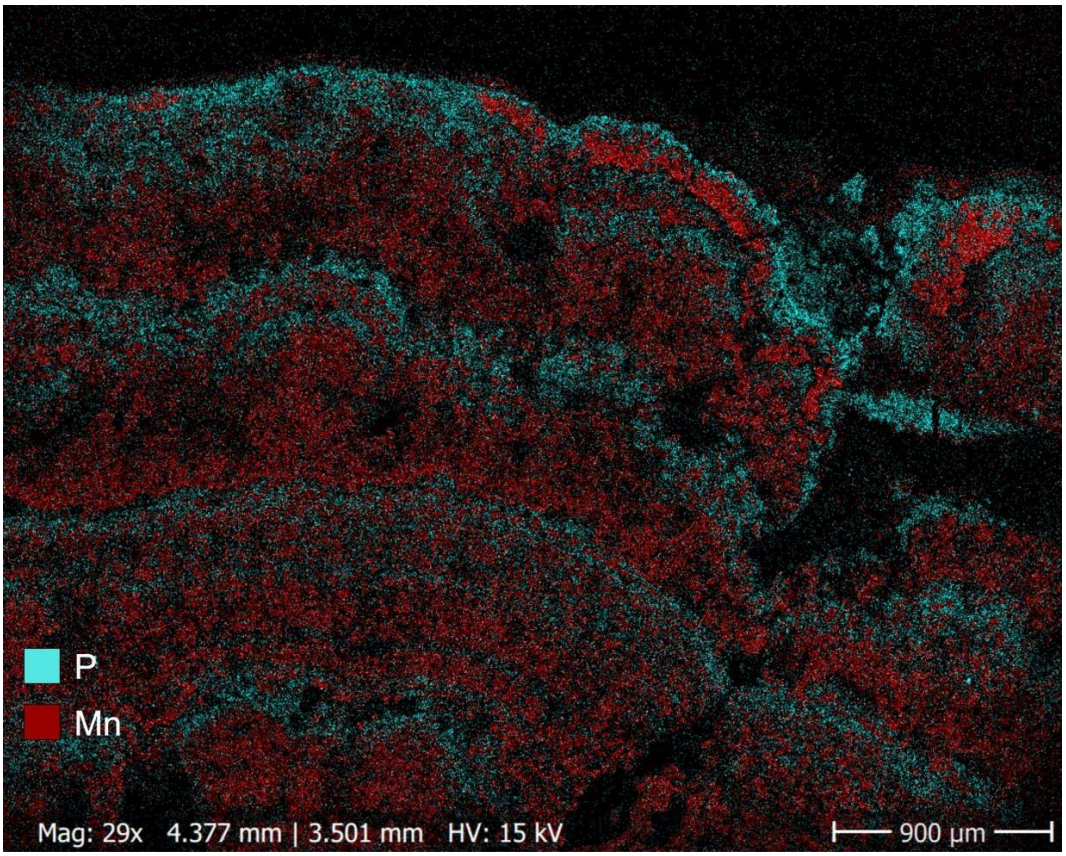

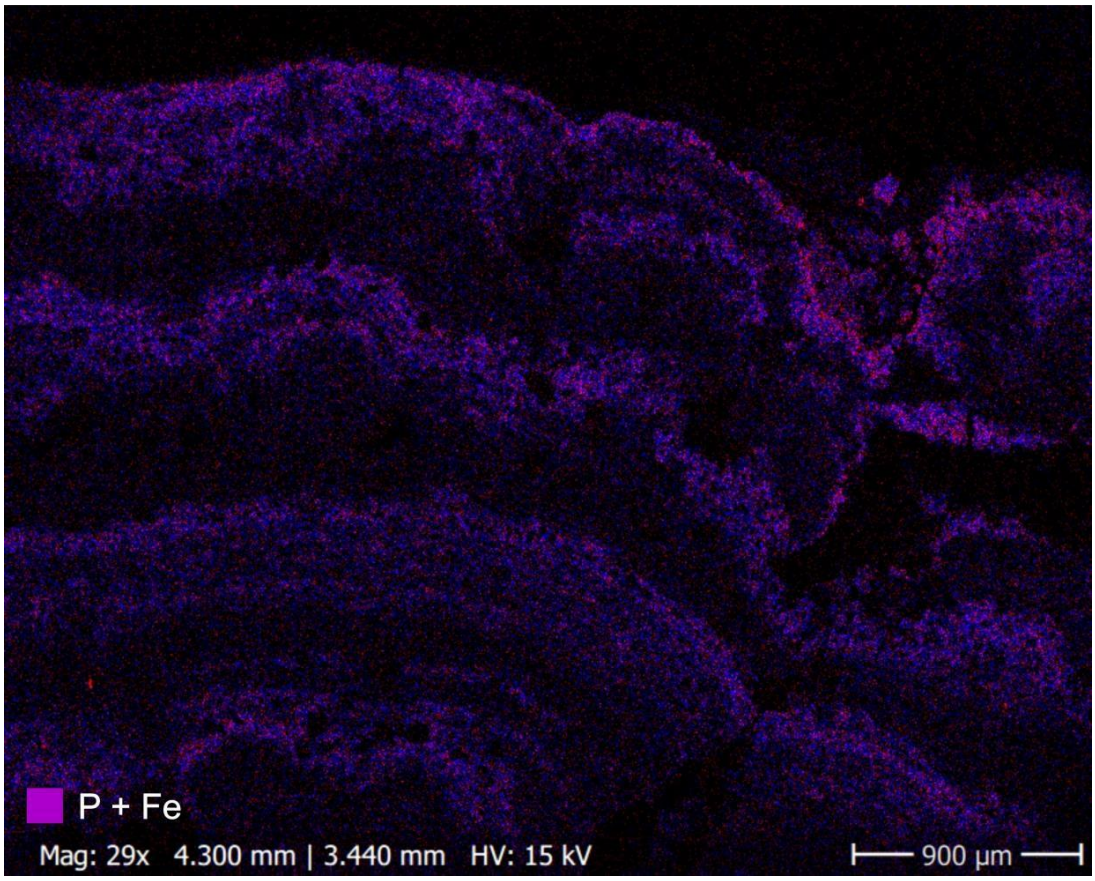
P + Fe
Mag: 29x 4.300 mm | 3.440 mm HV: 15 kV
900 µm

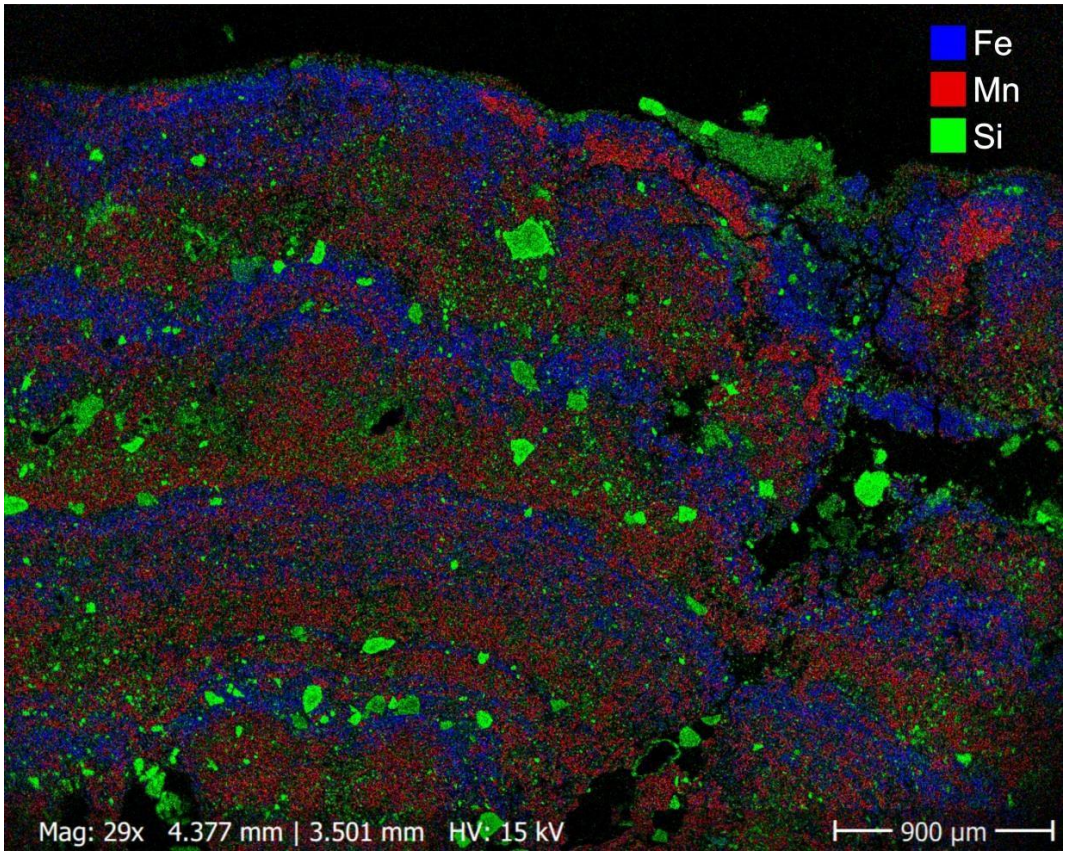
Fe
Mn
Si
Mag: 29x 4.377 mm | 3.501 mm HV: 15 kV
900 µm

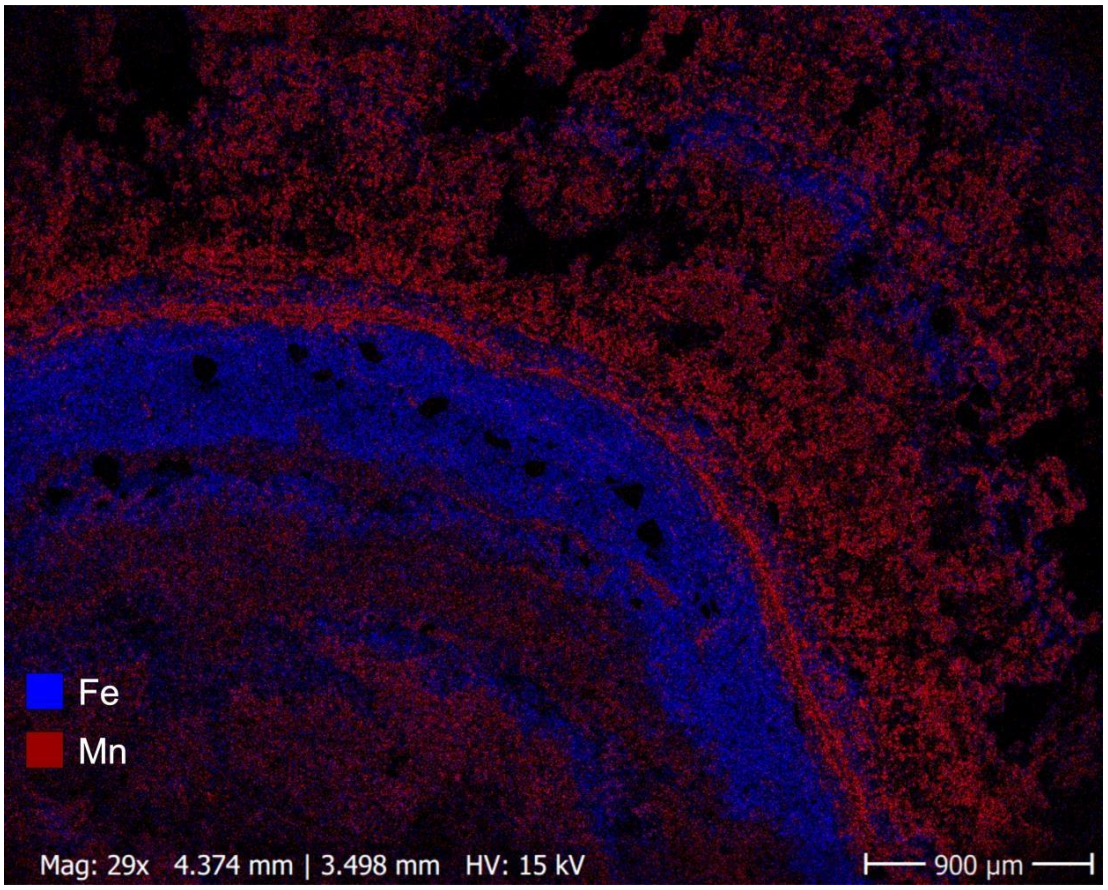
Fe
Mn
Mag: 29x 4.374 mm | 3.498 mm HV: 15 kV
900 µm

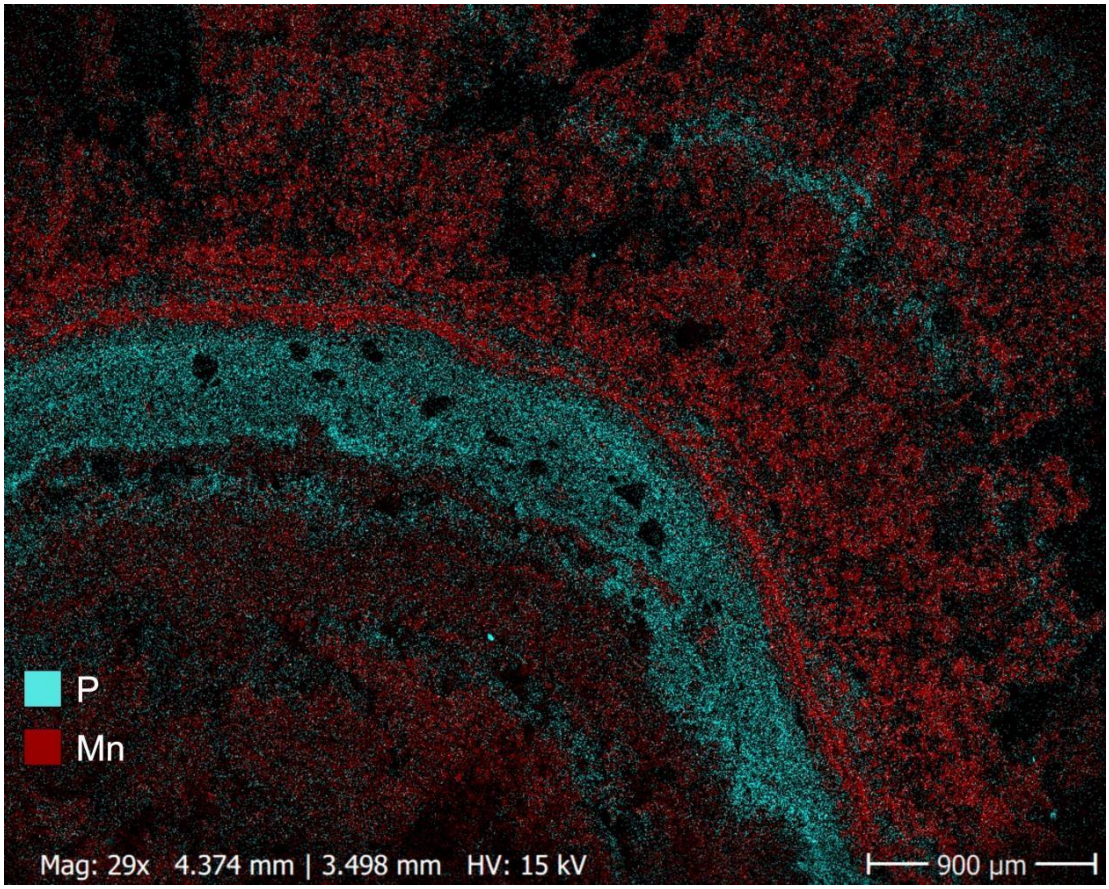
P
Mn
Mag: 29x 4.374 mm | 3.498 mm HV: 15 kV
900 µm

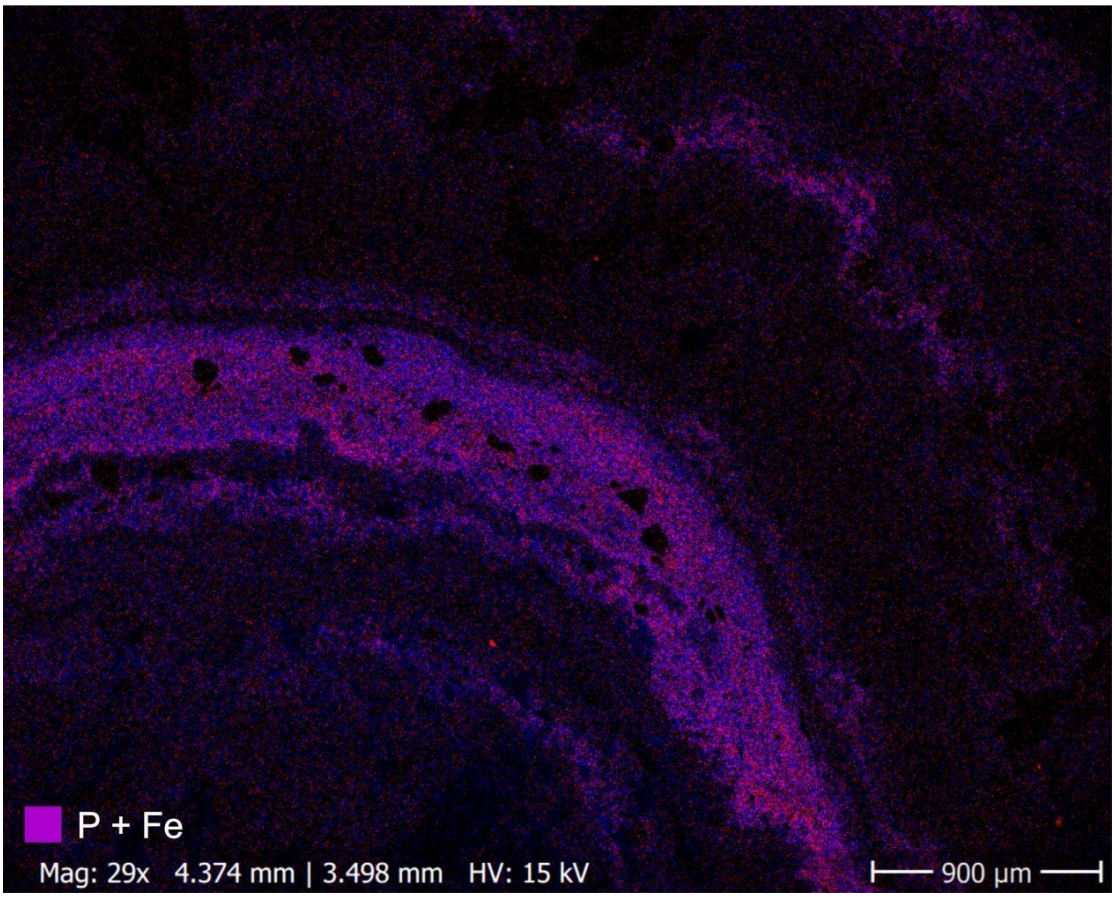
P + Fe
Mag: 29x 4.374 mm | 3.498 mm HV: 15 kV
900 µm

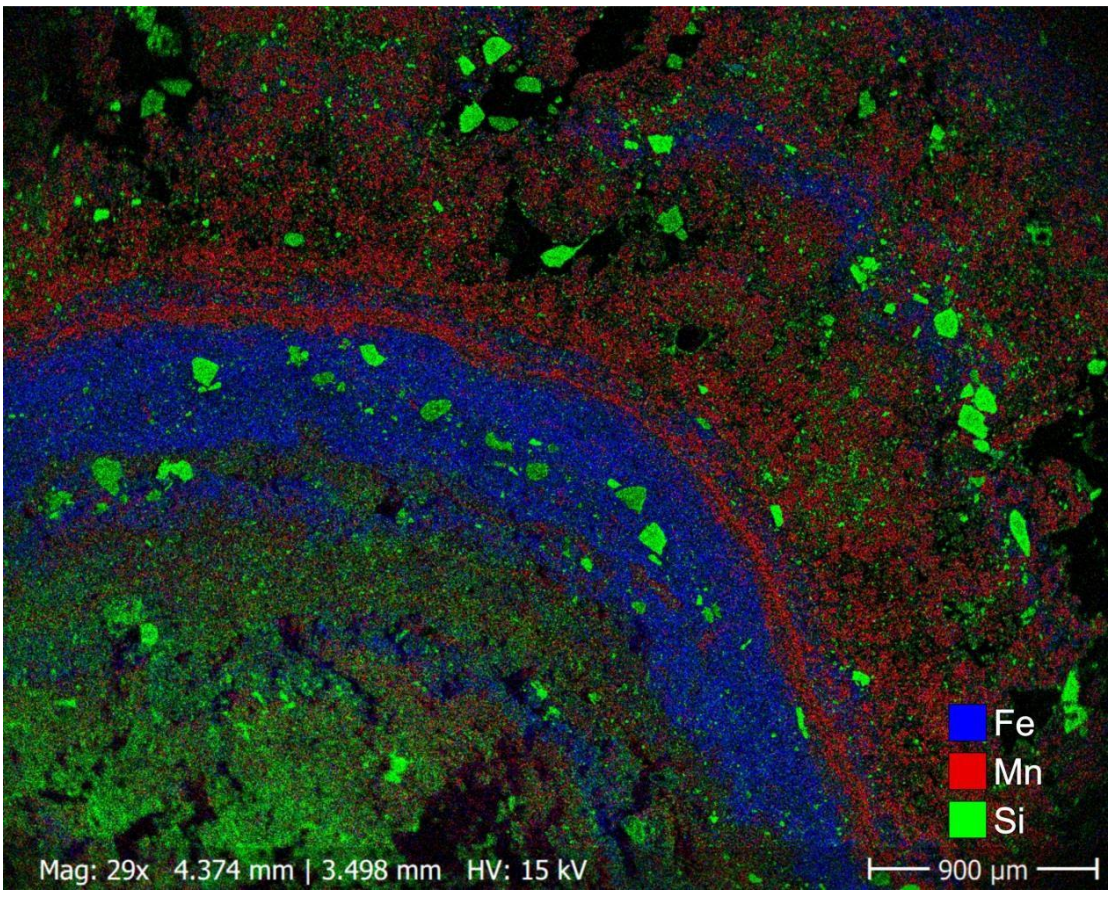
Fe
Mn
Si
Mag: 29x 4.374 mm | 3.498 mm HV: 15 kV
900 µm

Appendix D – EDS analysis results
Sample: JWEPMA

Electron microprobe	Jeol Superprobe
Model:	JXA-8600
Analysis type:	EDS
	standardless
Calibrated	none
Kiihdytysjännite:	15.0
Analysed:	20.8.2013 14:30

Ferrous layer core zone

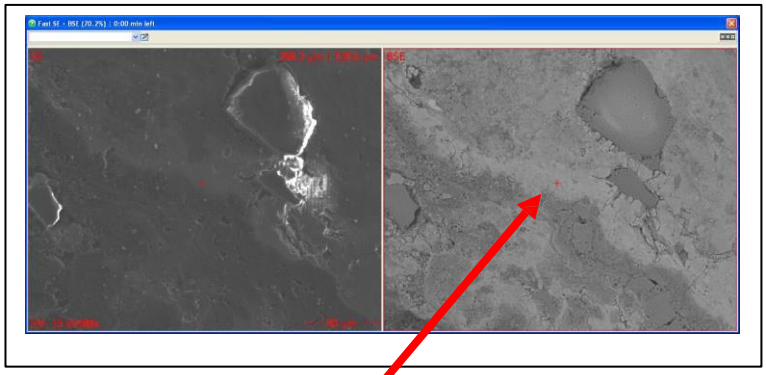

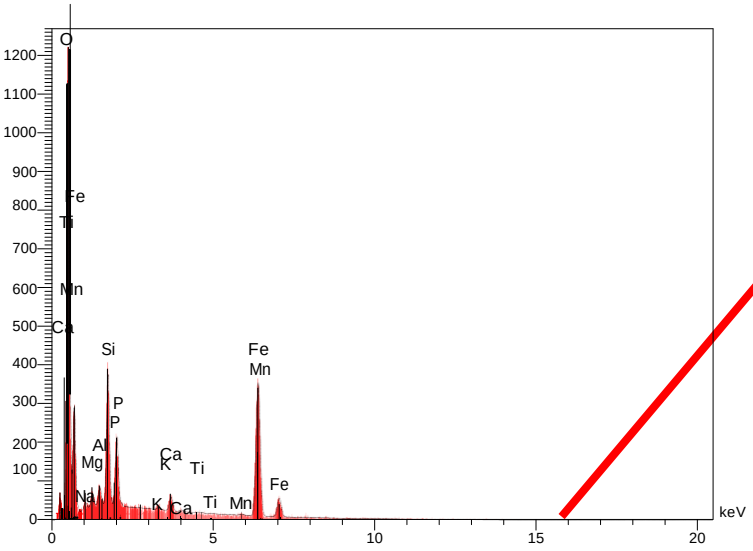

Elt	XRay	Int	W%	A%	Formula	Ox%
O			32.73	57.63		0.00
Na	Ka	8.5	0.80	0.98	Na2O	1.08
Mg	Ka	16.8	1.06	1.23	MgO	1.76
Al	Ka	25.1	1.30	1.35	Al2O3	2.45
Si	Ka	180.9	8.22	8.25	SiO2	17.59
P	Ka	99.8	5.01	4.56	P2O5	11.49
K	Ka	3.6	0.22	0.16	K2O	0.26
Ca	Ka	21.5	1.40	0.98	CaO	1.96
Ti	Ka	1.3	0.12	0.07	TiO2	0.20
Mn	Ka	2.1	0.31	0.16	MnO	0.40
Fe	Ka	263.2	48.83	24.63	FeO	62.82
			100.00	100.00		100.00

Sample: JWEPMA

Electron microprobe	Jeol Superprobe
Model:	JXA-8600
Analysis type:	EDS
	standardless
Calibrated	none
Kiihdytysjännite:	15.0
Analysed:	20.8.2013 14:43

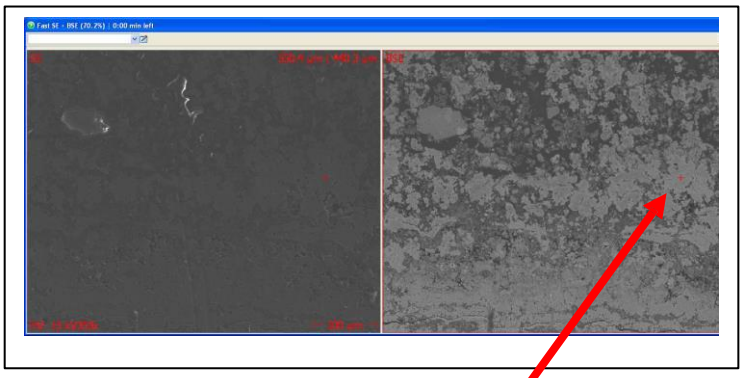

Mn zone near core (no phosphorus)

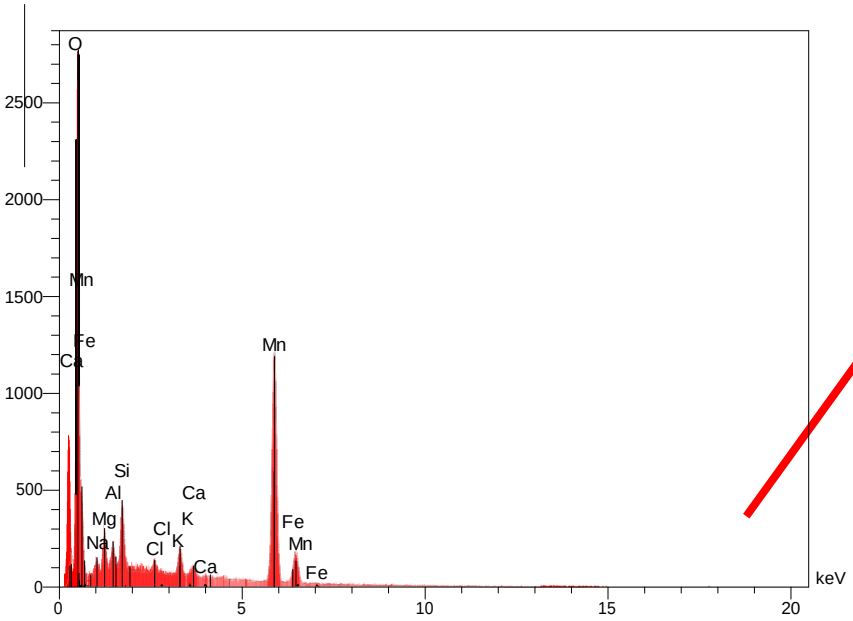

Elt	XRay	Int	W%	A%	Formula	Ox%
O			26.64	51.32		0.00
Na	Ka	14.5	1.70	2.27	Na2O	2.29
Mg	Ka	39.2	3.13	3.96	MgO	5.18
Al	Ka	26.1	1.73	1.98	Al2O3	3.27
Si	Ka	67.9	3.94	4.32	SiO2	8.43
Cl	Ka	12.4	0.79	0.69		0.79
K	Ka	28.8	2.13	1.68	K2O	2.56
Ca	Ka	9.1	0.72	0.55	CaO	1.01
Mn	Ka	301.6	58.17	32.64	MnO	75.11
Fe	Ka	4.6	1.05	0.58	FeO	1.35
			100.00	100.00		100.00

Sample: JWEPMA

Electron microprobe	Jeol Superprobe
Model:	JXA-8600
Analysis type:	EDS
	standardless
Calibrated	none
Kiihdytysjännite:	15.0
Analysed:	20.8.2013 14:35

Carbonaceous area near core

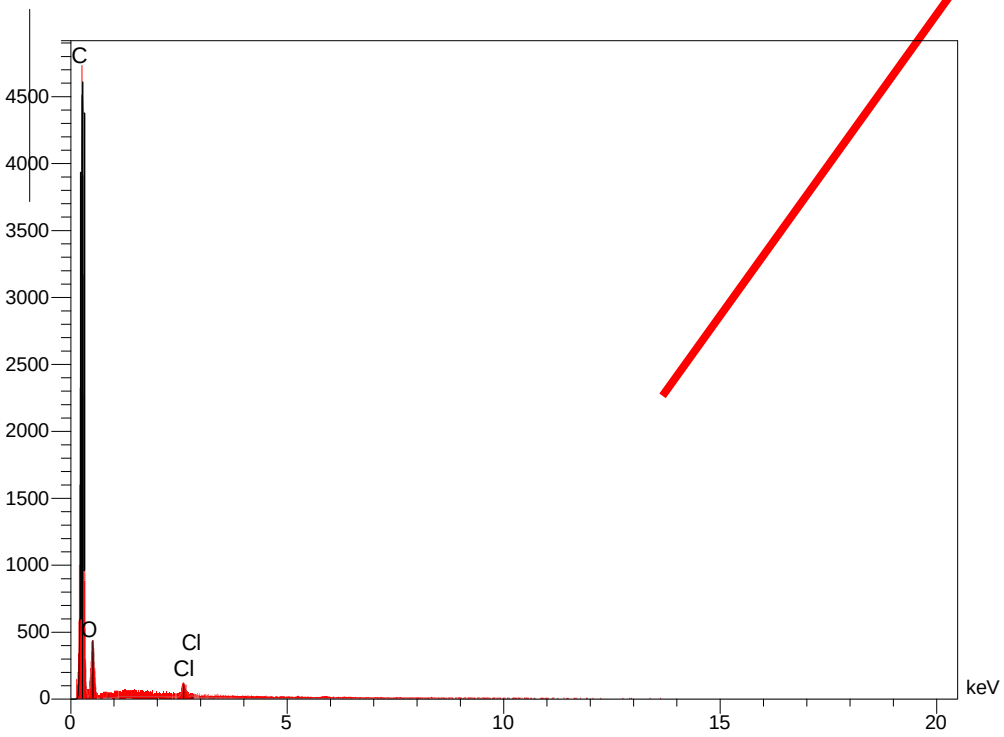

Elt	XRay	Int	W%	A%	Formula	Ox%
C	Ka	978.3	27.22	33.30	CO2	99.73
O			72.51	66.59		0.00
Cl	Ka	28.3	0.27	0.11		0.27
			100.00	100.00		100.00

Sample: JWEPMA

Electron microprobe	Jeol Superprobe
Model:	JXA-8600
Analysis type:	EDS
	standardless
Calibrated	none
Kiihdytysjännite:	15.0
Analysed:	20.8.2013 14:17

first iron layer in core- biotite grain

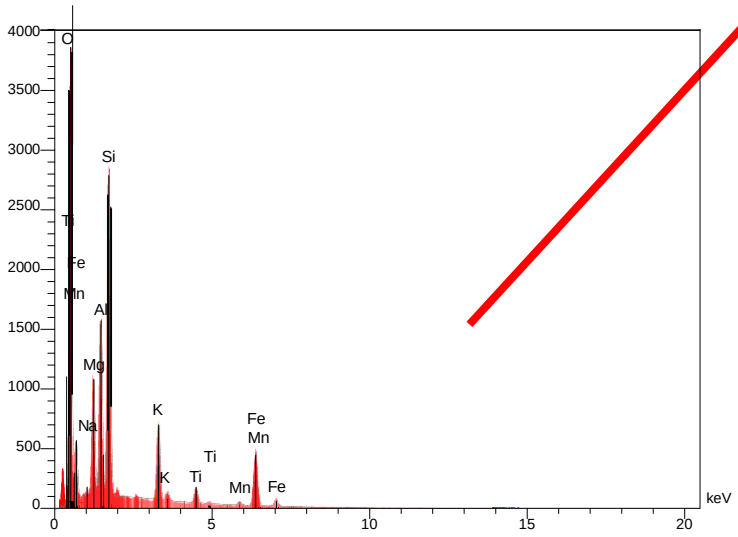

Elt	XRay	Int	W%	A%	Formula	Ox%
O			39.48	57.91		0.00
Na	Ka	4.9	0.31	0.32	Na2O	0.42
Mg	Ka	142.8	6.57	6.34	MgO	10.90
Al	Ka	223.1	9.45	8.22	Al2O3	17.85
Si	Ka	427.3	17.67	14.76	SiO2	37.79
K	Ka	110.8	6.38	3.83	K2O	7.69
Ti	Ka	22.7	1.98	0.97		1.98
Mn	Ka	5.0	0.74	0.31	MnO	0.95
Fe	Ka	98.3	17.42	7.32	FeO	22.41
			100.00	100.00		100.00

EDS Spot analyses for Dissolution experiment precipitates

Label	W%(O)	W%(Na)	W%(Al)	W%(Si)	W%(P)	W%(S)	W%(Cl)	W%(Ca)	W%(Ti)	W%(Mn)	W%(Fe)	B.Current
JWTomo3p4.3	0	0	0	1.3	7.8	4.1	3.2	2.5	0.0	0.8	80.4	1.02
JWTomo5p1	0	0	0	8.8	1.3	21.7	5.1	1.0	0.0	0.3	61.8	1.03
JWTomo5p2titanite	0	0	0	25.2	1.0	3.3	1.6	28.7	33.1	0.4	6.8	1.02
JWTomo5p3albite	49.0	6.9	11.0	31.5	0.0	0.3	0.1	0.6	0.1	0.1	0.3	1.03
JWTomo5p4	37.9	4.1	2.2	5.8	0.6	10.9	1.3	0.9	0.1	0.2	35.9	1.02
JWTomo5p5	35.9	3.8	1.0	1.7	1.0	12.1	1.9	0.8	0.1	0.4	41.4	1.02
JWTomo5p6	36.5	6.8	1.7	3.2	0.8	12.3	5.8	0.6	0.1	0.2	32.0	1.02

	A%(O)	A%(Na)	A%(Al)	A%(Si)	A%(P)	A%(S)	A%(Cl)	A%(Ca)	A%(Ti)	A%(Mn)	A%(Fe)	B.Current
JWTomo3p4.3	0	0	0	2.2	12.5	6.3	4.4	3.0	0.0	0.7	70.9	1.02
JWTomo5p1	0	0	0	13.6	1.8	29.3	6.2	1.1	0.0	0.2	47.9	1.03
JWTomo5p2titanite	0	0	0	34.3	1.3	3.9	1.7	27.4	26.5	0.2	4.6	1.02
JWTomo5p3albite	62.2	6.1	8.3	22.8	0.0	0.2	0.0	0.3	0.0	0.0	0.1	1.03
JWTomo5p4	60.7	4.5	2.1	5.3	0.5	8.7	0.9	0.6	0.1	0.1	16.5	1.02
JWTomo5p5	60.0	4.4	1.0	1.6	0.8	10.1	1.4	0.5	0.1	0.2	19.8	1.02
JWTomo5p6	58.2	7.5	1.6	2.9	0.7	9.8	4.2	0.4	0.0	0.1	14.6	1.02

Appendix E - Helsinki-water composition and added vitamins

Helsinki-water

Macronutrients	Concentration **mg/l**	**Micronutrients**	Concentration **µg/l**	**Salts**	Concentration **g/l**
NH_4Cl	16,13 measured 3-4	$Na_2WO_4*2H_2O$	0,165	NaCl	4,68
K_2HPO_4	1,55	$(NH_4)_6Mo_7O_{24}*2H_2O$	0,44	$MgCl_2$	1,36
		KBr	0,6	$MgSO_4*7H_2O$	0,56
		KI	0,415	$CaCl_2*2H_2O$	0,46
		$ZnSO_4*7H_2O$	1,435	K_2SO_4	0,15
		$Cd(NO_3)_2*4H_2O$	0,77	$CaCO_3$	0,02
		$Co(NO_3)_2*6H_2O$	0,73		
		$CuSO_4*5H_2O$	0,625		
		$NiSO_4(NH_4)_2SO_4*6H_2O$	0,99		
		$Cr(NO_3)_3*9H_2O$	0,205		
		$KAl(SO_4)_2*12H_2O$	4,74		
		V_2O_5	0,0445		
		H_3BO_3	15,5		
		$FeCl_3*6H_2O$	*140*		
		$MnSO_4*4H_2O$	*11,15*		

Vitamins:
biotin
nicotinamide
p-aminobenzoic acid
thiamin (B1)
pantothenic acid
pyridoxamine (B6) pyridoxine
cyanocobalamine (B12)
riboflavin (B2)
folic acid

Appendix F - EDS element mapping and linescan data for JWEPMA

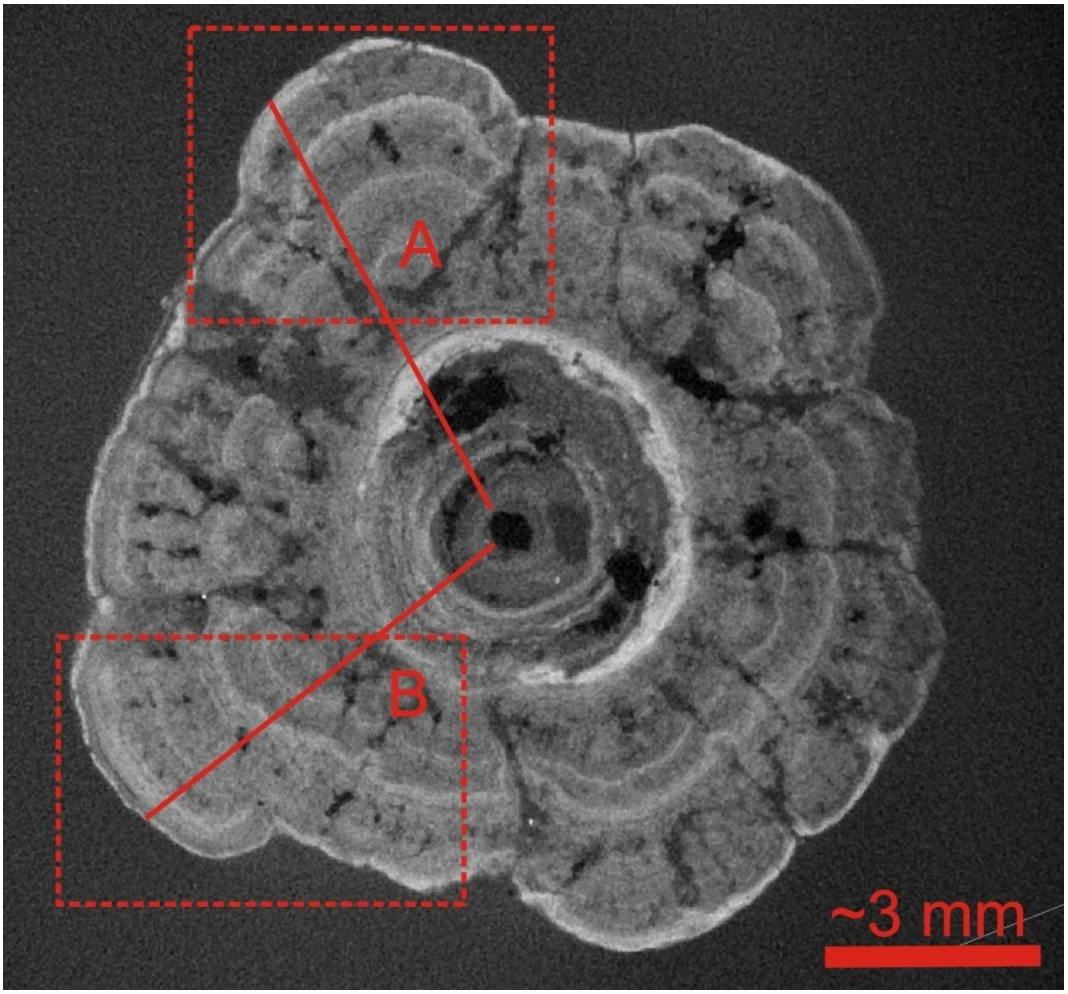

Raw CT grayscale slice of JWEPMA. Dashed line boxes and coherent lines A and B were possible areas of interest for both line scan and element mapping. In the end area A was chosen for both analyses.

| | | |